AD-A261 700

RL-TR-92-257
Final Technical Report
November 1992

MICROSTRIP ANTENNAS ON/IN ANISOTROPIC MATERIAL LAYERS

Phraxos Research and Development, Inc.

H.Y. Yang, J.A. Castaneda, A. Nakatani

DTIC
ELECTE
MAR 03 1993
S E D

93-04419

APPROVED FOR PUBLIC RELEASE; DISTRIBUTION UNLIMITED.

Rome Laboratory
Air Force Materiel Command
Griffiss Air Force Base, New York

This report has been reviewed by the Rome Laboratory Public Affairs Office (PA) and is releasable to the National Technical Information Service (NTIS). At NTIS it will be releasable to the general public, including foreign nations.

RL-TR-92-257 has been reviewed and is approved for publication.

APPROVED: Michelle H Champion

MICHELLE H. CHAMPION
Project Engineer

FOR THE COMMANDER: John K. Schindler

JOHN K. SCHINDLER, Director
Electromagnetics & Reliability Directorate

If your address has changed or if you wish to be removed from the Rome Laboratory mailing list, or if the addressee is no longer employed by your organization, please notify RL(ERAA) Hanscom AFB MA 01731-5000. This will assist us in maintaining a current mailing list.

Do not return copies of this report unless contractual obligations or notices on a specific document require that it be returned.

DISCLAIMER NOTICE

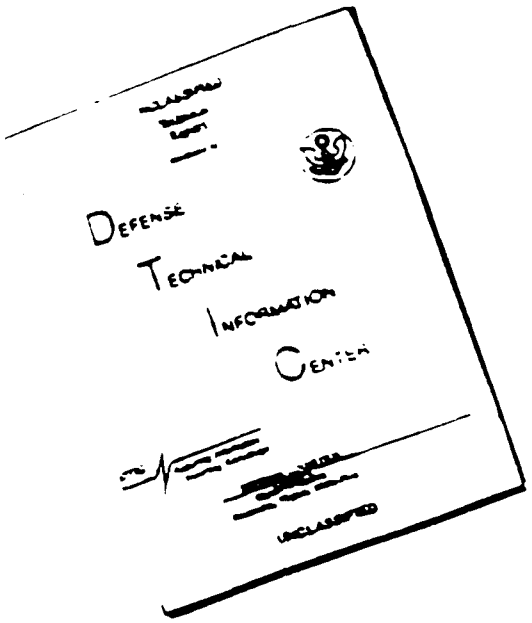

THIS DOCUMENT IS BEST QUALITY AVAILABLE. THE COPY FURNISHED TO DTIC CONTAINED A SIGNIFICANT NUMBER OF PAGES WHICH DO NOT REPRODUCE LEGIBLY.

REPORT DOCUMENTATION PAGE

Form Approved
OMB No. 0704-0188

Public reporting burden for this collection of information is estimated to average 1 hour per response, including the time for reviewing instructions, searching existing data sources, gathering and maintaining the data needed, and completing and reviewing the collection of information. Send comments regarding this burden estimate or any other aspect of this collection of information, including suggestions for reducing this burden, to Washington Headquarters Services, Directorate for information Operations and Reports, 1215 Jefferson Davis Highway, Suite 1204, Arlington, VA 22202-4302, and to the Office of Management and Budget, Paperwork Reduction Project (0704-0188), Washington, DC 20503

1. AGENCY USE ONLY (Leave Blank)	2. REPORT DATE	3. REPORT TYPE AND DATES COVERED
	November 1992	Final Aug 88 - Feb 91

4. TITLE AND SUBTITLE
MICROSTRIP ANTENNAS ON/IN ANISOTROPIC MATERIAL LAYERS

5. FUNDING NUMBERS
C - F19628-88-C-0059
PE - 61102F
PR - 2305
TA - J3
WU - 59

6. AUTHOR(S)
H.Y. Yang, J.A. Castaneda, A. Nakatani

7. PERFORMING ORGANIZATION NAME(S) AND ADDRESS(ES)
Phraxos Research and Development, Inc.
2716 Ocean Park Blvd., Suite 1020
Santa Monica CA 90405

8. PERFORMING ORGANIZATION REPORT NUMBER
RPT-91025

9. SPONSORING/MONITORING AGENCY NAME(S) AND ADDRESS(ES)
Rome Laboratory (ERAA)
Hanscom AFB MA 01731-5000

10. SPONSORING/MONITORING AGENCY REPORT NUMBER
RL-TR-92-257

11. SUPPLEMENTARY NOTES
Rome Laboratory Project Engineer: Michelle H. Champion/ERAA/(617) 377-4036

12a. DISTRIBUTION/AVAILABILITY STATEMENT
Approved for public release: distribution unlimited.

12b. DISTRIBUTION CODE

13. ABSTRACT (Maximum 200 words)

Accurate fullwave analyses of microstrip dipoles on multi-layer substrates with generalized anisotropic permittivity and permeability have been developed. The solution to the problem of microstrip dipoles on/in gyrotropic substrates has been obtained. The potential of electronically shaped, scanned, and gain enhanced element factors with ferrite substrates has been theoretically demonstrated. The scattering and radiation problems were solved. The use of biased ferrite substrates to simultaneously reduce RCS and preserve antenna in-band gain has also been described. Infinite phased arrays of microstrip dipoles and probe-fed patches on general anisotropic multi-layer substrates have been analyzed. All the solutions involve the dyadic Green's function for the anisotropic layered structure and the application of the method of moments to an electric field integral equation.

14. SUBJECT TERMS
Microstrip Antennas, Microstrip Arrays, Anisotropic Substrates, Gyrotropic Substrates, Scattering, Phased Arrays

15. NUMBER OF PAGES
102

16. PRICE CODE

17. SECURITY CLASSIFICATION OF REPORT	18. SECURITY CLASSIFICATION OF THIS PAGE	19. SECURITY CLASSIFICATION OF ABSTRACT	20. LIMITATION OF ABSTRACT
UNCLASSIFIED	UNCLASSIFIED	UNCLASSIFIED	UL

Accesion For
NTIS CRA&I ☒
DTIC TAB ☐
Unannounced ☐
Justification
By
Distribution /
Availability Codes
Dist | Avail and / or Special
A-1

CONTRIBUTORS:

Jesse A. Castaneda (Project Manager)
Hung-Yu Yang (Project Lead Scientist)
Akifumi Nakatani

PUBLICATIONS RESULTING FROM THIS PROJECT:

Journal Papers:

1. H.Y. Yang and J.A. Castaneda, "Printed Dipole Charateristics in a Two-Layer Geometry with Uniaxial Anisotropy," Electromagnetics, vol 9, pp 439-450, 1989.

2. H.Y. Yang, A. Nakatani, and J.A. Castaneda, "Efficient Evaluation of Spectral Integrals in the Moment Method Solution of Microstrip Antennas and Circuits," IEEE Transactions on Antennas and Propagation, accepted for publication.

3. Hung-Yu Yang and Jesse A. Castaneda, "Infinite Phased Arrays of Microstrip Antennas on Generalized Anisotropic Substrates," Electromagnetics, vol 11, pp 107-124, 1991.

Symposium Papers and Presentations:

4. A. Nakatani and J.A. Castaneda, "Accurate and Efficient Modelling of Dispersive MMIC Passive Discontiuity Components," Applied Computational Electromagnetics Society Symposium, March 22, 1989.

SUMMARY

The project objective was the development of fullwave analyses for the characterization of microstrip antennas and arrays on multi-layer anisotropic substrates. Many other researchers have addressed the problem of strip antennas on isotropic substrates. The material constants are very important to the performance of printed antennas. In practice, many dielectric and magnetic media are anisotropic. Neglecting the substrate anisotropy can introduce significant errors in the design of microwave printed circuits[3]. Similar sensitivities to anisotropy are exhibited by printed antenna structures. In some instances the anisotropy is a principal feature of the design materials, as is the case with biased ferrite substrates. Thus, accurate models, which include anisotropy, are needed for microstrip antennas and arrays.

The analyses for microstrip dipole elements on general anisotropic substrates have been developed. The solutions for infinite arrays of microstrip dipoles and probe-fed patches on generalized anisotropic substrates have also been derived. Provision has been made for both dielectric and magnetic anisotropy. In Chapter 1 the printed dipole antenna on a two layer uniaxial substrate is addressed. Chapter 2 deals with dipoles on gyrotropic substrates (such as the biased ferrite). The use of biased ferrite substrates provides very interesting capabilities, including element pattern scanning, element pattern shaping, and element gain enhancement. All these features can be actively controlled by way of the bias field strength. In addition, in Chapter 3 the use of biased ferrite substrates for the reduction of RCS is illustrated. The non-reciprocal nature of the microstrip antenna with biased ferrite materials permits the reduction of RCS while transmit gain is preserved.

A substantial effort was devoted to the development of efficient algorithms for the evaluation of the spectral integrals that arise in the solution method which was adopted. It resulted in significant improvements in the numerical efficiency of the solutions. This is discussed in Chapter 4.

In Chapter 5 the analyses for the infinite phased arrays of strip dipoles and probe-fed patches on general anisotropic substrates are presented. The results include the impedance as a function of scan.

The solutions which were developed are fullwave integral equation solutions using the method of moments. The Green's functions for the structures were found by a matrix method which can be easily extended to any number of anisotropic layers.

The effects of substrate anisotropy on printed antenna characteristics have been shown to be important. In addition, several potentially significant applications of biased ferrite substrates have been identified.

Contents

1 Microstrip Dipole on a Two-layer Uniaxial Dielectric Substrate 1

1.1 Green's Function 1

1.2 The Method of Moments 6

1.3 Antenna Gain and Radiation Efficiency 7

1.4 Results 8

1.4.1 Conclusion 11

2 Microstrip Dipoles on Gyrotropic Substrates 16

2.1 Introduction 16

2.2 Theory 17

2.2.1 Material Characteristics of Ferrites 17

2.2.2 Green's Function for a Grounded Ferrite 19

2.2.3 The Moment Method Solution 21

2.3 Numerical Results 24

2.3.1 Element Pattern Shaping, Scanning, and Gain Enhancement 24

2.3.2 Conclusion 29

3 Scattering and RCS of Microstrip Dipoles on/in Biased Ferrite Substrates **33**

3.1 The Integral Equation for Scattering 34

3.2 The Moment Method Solution for the Induced Dipole Currents . . 34

3.3 Scattered Far Fields and Radar Cross Section 35

3.4 Results 36

3.5 Conclusion 37

4 Evaluation of Spectral Integrals in the Moment Method **50**

4.1 Introduction 50

4.2 The New Algorithm 51

4.3 Numerical Examples 57

4.3.1 A Center-fed Dipole 57

4.3.2 Microstrip Open-end and Gap Discontinuities 57

4.4 Conclusions 58

5 Infinite Arrays of Microstrip Antennas on Generalized Anisotropic Substrates **60**

5.1 Introduction 60

5.2 Analysis 62

5.2.1 Integral Equation and Green's Function for Infinite Probe-fed Patch Arrays 66

5.2.2 Method of Moments for Infinite Patch Arrays 68

5.2.3 Integral Equation and Green's Function for Infinite dipole Arrays 69

5.3 Results 70

5.3.1 Conclusion 82

List of Figures

1.1 A Two-Layer Printed Antenna Structure with Uniaxial Anisotropy 2

1.2 Broadside Gain Versus Frequency. Antenna Is at the Material Interface with h = 0.08 cm, and b = 0.04 cm. The substrate is anisotropic (Sapphire). 9

1.3 Broadside Gain versus Frequency. The antenna is at the material interface with h = 0.08 cm, and b = 0.04 cm. The superstrate is anisotropic (Sapphire). 10

1.4 Radiation Efficiency versus Material Thickness. The antenna is at the material interface with h = 2b. 12

1.5 Input Resistance of a Center-fed Dipole. The antenna is at the material interface with h = 0.2 λ_0, b = 0.1 λ_0, and w/h = 0.05 . . 13

1.6 Input Reactance of a Center-fed Dipole. The antenna is at the material interface with h = 0.2 λ_0, b = 0.1 λ_0, and w/h = 0.05 . . 14

1.7 Dipole Resonant Length versus Material Thickness. The antenna is at the material interface with h = 2b and w = 0.05 h. 15

2.1 A Microstrip Dipole on a Ferrite Substrate 18

2.2 E-plane Transmit Gain Pattern for a Center-fed Dipole on a Ferrite Substrate 25

2.3 H-plane Transmit Gain Pattern for a Center-fed Dipole on a Ferrite Substrate 26

2.4 E-plane Directivity of a Center-fed Dipole on a Ferrite Substrate . 27

2.5 H-plane Directivity of a Center-fed Dipole on a Ferrite Substrate . 28

2.6 Element Beam Pointing Angle as a Function of Bias Field 30

2.7 H-plane Patterns for two different Bias Fields 31

2.8 Element Beam Pointing Angle as a Function of Frequency 32

3.1 RCS at Broadside as a Function of Frequency 38

3.2 Transmit Gain as a Function of Frequency 39

3.3 RCS at Broadside as a Function of Field Polarization 40

3.4 Current at the Load as a Function of Incident Field Polarization . 41

3.5 Received Power as a Function of Incident Field Polarization 42

3.6 Broadside RCS as a Function of Frequency for Different Incident Field Polarizations 43

3.7 Broadside RCS as a Function of Frequency for Different Incident Field Polarizations 44

3.8 Induced Current as a Function of Frequency for Different Incident Field Polarizations 45

3.9 Induced Current as a Function of Frequency for Different Incident Field Polarizations 46

3.10 Transmit Gain Patterns 48

3.11 Receive Patterns 49

4.1 A Two-layer Printed Antenna Structure 52

4.2 Integration Contour in either the λ_x or λ_y complex plane. 54

4.3 $-jS(\lambda_x)$ as a function of λ_x 56

5.1 Infinite Array of Printed Dipoles on a Generalized Anisotropic Substrate. 63

5.2 Infinite Array of Probe-fed Patches on a Generalized Anisotropic Substrate. 64

5.3 E-plane Scan Characteristics of Infinite Printed Dipole Array. . . . 71

5.4 H-plane Scan Characteristics of Infinite Printed Dipole Array . . . 72

5.5 E-plane Scan of a Dipole Array on a Uniaxial Substrate with Tilted Optical Axis 73

5.6 H-plane Scan of a Dipole Array on a Uniaxial Substrate with Tilted Optical Axis 74

5.7 E-plane Scan Characteristics of an Infinite Probe-fed Patch Array on a Uniaxial Substrate with Tilted Optical Axis 75

5.8 H-plane Scan Characteristics of an Infinite Probe-fed Patch Array on a Uniaxial Substrate with Tilted Optical Axis 76

5.9 Comparison of the Scan Characteristics of Dipole Arrays on Isotropic and Biased Ferrite (gyrotropic) Substrates. 77

5.10 E-plane Scan Characteristics of an Infinite Array of Printed Dipoles on a Ferrite Substrate. 78

5.11 H-plane Scan Characteristics of an Infinite Array of Printed Dipoles on a Ferrite Substrate. 79

5.12 Scan Characteristics of an Infinite Probe-fed Patch Array on a Ferrite Substrate 80

5.13 Input Reflection Coefficient for the Patch Array on a Biased Ferrite Substrate as a Function of the Bias Field Angle 81

Chapter 1

Microstrip Dipole on a Two-layer Uniaxial Dielectric Substrate

The fullwave solution for the considered structure involves: (i) the development of the Green's Function appropriate to the structure; (ii) the application of the method of moments to an electric field integral equation involving the unknown currents on the strip antenna element; and (iii) the derivation of the antenna characteristics such as input impedance, gain, and efficiency from the knowledge of those currents.

1.1 Green's Function

The geometry of the structure under consideration is shown in Figure 1.1. The bottom layer of thickness b (region I) is assumed to have a permeability μ_1 and permittivity $\bar{\epsilon}_1$

$$\bar{\epsilon}_1 = \begin{pmatrix} \epsilon_1^x & 0 & 0 \\ 0 & \epsilon_1^x & 0 \\ 0 & 0 & \epsilon_1^z \end{pmatrix}, \tag{1.1}$$

while the top layer of thickness t (region II) is assumed to have a permeability μ_2 and permittivity $\bar{\epsilon}_2$

$$\bar{\epsilon}_2 = \begin{pmatrix} \epsilon_2^x & 0 & 0 \\ 0 & \epsilon_2^x & 0 \\ 0 & 0 & \epsilon_2^z \end{pmatrix}. \tag{1.2}$$

The total material thickness is h = (b+t). For the problem considered here the source (antenna) is located either at the material interface (z = b) or at the air-dielectric interface (z = h). Therefore, Maxwell's curl equations for each region

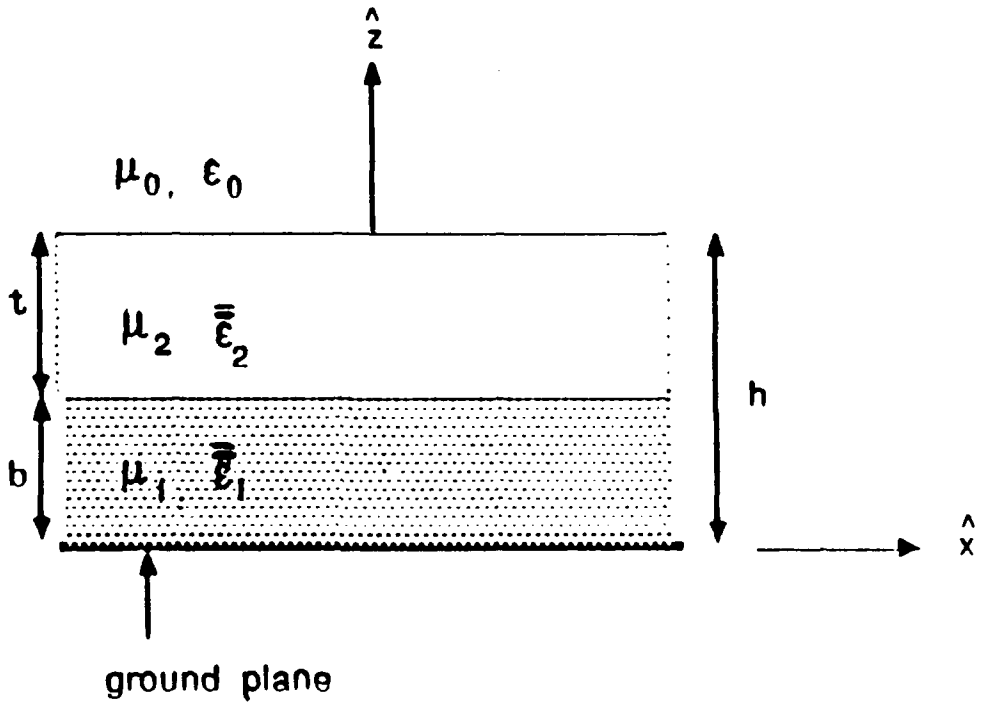

Figure 1.1: A Two-Layer Printed Antenna Structure with Uniaxial Anisotropy

are source free. The Maxwell's curl equations are

$$\nabla \times \vec{E} = -j\omega\mu\vec{H} \tag{1.3}$$

and

$$\nabla \times \vec{H} = j\omega\bar{\epsilon} \cdot \vec{E}. \tag{1.4}$$

The Fourier and inverse Fourier transform pairs are defined as:

$$\mathcal{L}(x - x\prime, y - y\prime, z) = \frac{1}{4\pi^2} \int_{-\infty}^{\infty} \int_{-\infty}^{\infty} \tilde{\mathcal{L}}(\lambda_x, \lambda_y, z)\, e^{j\lambda_x(x-x\prime)} e^{j\lambda_y(y-y\prime)} d\lambda_x\, d\lambda_y \tag{1.5}$$

and

$$\tilde{\mathcal{L}}(\lambda_x, \lambda_y, z) = \int_{-\infty}^{\infty} \int_{-\infty}^{\infty} \mathcal{L}(x - x\prime, y - y\prime, z) e^{-j\lambda_x(x-x\prime)} e^{-j\lambda_y(y-y\prime)} dx dy. \tag{1.6}$$

The vector function $\mathcal{L}$ is either the electric or magnetic field. From Eqs 1.3- 1.6, it can be shown that the transformed field components must satisfy the following equations:

$$\frac{\epsilon_z}{\epsilon_x} \frac{\partial^2 \tilde{E}_z}{\partial^2 z} + (k_o^2 \epsilon_z \mu - \lambda^2)\tilde{E}_z = 0, \tag{1.7}$$

$$\frac{\partial^2 \tilde{H}_z}{\partial^2 z} + (k_o^2 \epsilon_x - \lambda^2)\tilde{H}_z = 0 \tag{1.8}$$

$$(k_o^2 \mu \epsilon_x + \frac{\partial}{\partial z^2})\tilde{E}_x = \omega\mu\lambda_y \tilde{H}_z + j\lambda_x \frac{\partial \tilde{E}_z}{\partial z}, \tag{1.9}$$

$$(k_o^2 \mu \epsilon_x + \frac{\partial}{\partial z^2})\tilde{E}_y = -\omega\mu\lambda_x \tilde{H}_z + j\lambda_y \frac{\partial \tilde{E}_z}{\partial z}, \tag{1.10}$$

$$(k_o^2 \mu \epsilon_x + \frac{\partial}{\partial z^2})\tilde{H}_x = -\omega\epsilon_x\lambda_y \tilde{E}_z + j\lambda_x \frac{\partial \tilde{H}_z}{\partial z}, \tag{1.11}$$

$$(k_o^2 \mu \epsilon_x + \frac{\partial}{\partial z^2})\tilde{H}_y = \omega\epsilon_x\lambda_x \tilde{E}_z + j\lambda_y \frac{\partial \tilde{H}_z}{\partial z}. \tag{1.12}$$

From Eqs. 1.7- 1.12, the electromagnetic fields in each region can be expressed as:

In region I, $0 \leq z \leq b$,

$$\tilde{E}_z = A\cosh(q_1^a z),\ \tilde{H}_z = B\sinh(q_1^a z), \tag{1.13}$$

$$\tilde{E}_x = \frac{\omega\mu_o\mu_1\lambda_y}{\lambda^2} B\sinh(q_1^b z) + \frac{j\lambda_x q_1^a \epsilon_1^z}{\epsilon_1^z \lambda^2} A\sinh(q_1^a z), \tag{1.14}$$

$$\tilde{E}_y = \frac{-\omega\mu_o\mu_1\lambda_x}{\lambda^2} B\sinh(q_1^b z) + \frac{j\lambda_y q_1^a \epsilon_1^z}{\epsilon_1^z \lambda^2} A\sinh(q_1^a z), \tag{1.15}$$

$$\tilde{H}_x = \frac{j\lambda_x q_1^b}{\lambda^2} B\cosh(q_1^b z) - \frac{\omega\epsilon_o\epsilon_1^z\lambda_y}{\lambda^2} A\cosh(q_1^a z), \tag{1.16}$$

$$\tilde{H}_y = \frac{j\lambda_y q_1^b}{\lambda^2} B\cosh(q_1^b z) + \frac{\omega\epsilon_o\epsilon_1^z\lambda_x}{\lambda^2} A\cosh(q_1^a z), \tag{1.17}$$

where

$$q_1^a = \sqrt{\frac{\epsilon_1^x}{\epsilon_1^z}(\lambda^2 - \epsilon_1^x k_o^2\mu_1)} \tag{1.18}$$

$$q_1^b = \sqrt{(\lambda^2 - \epsilon_1^z k_o^2\mu_1)}. \tag{1.19}$$

In region II, $b \le z \le h$,

$$\tilde{E}_z = C\cosh(q_2^a z) + D\sinh(q_2^a z),\ \tilde{H}_z = E\cosh(q_2^b z) + F\sinh(q_2^b z), \tag{1.20}$$

$$\tilde{E}_x = \frac{\omega\mu_o\mu_2\lambda_y}{\lambda^2}[E\cosh(q_2^b z) + F\sinh(q_2^b z)] + \frac{j\lambda_x q_2^a\epsilon_2^z}{\epsilon_2^x\lambda^2}[D\cosh(q_2^a z) + C\sinh(q_2^a z)], \tag{1.21}$$

$$\tilde{E}_y = \frac{-\omega\mu_o\mu_2\lambda_x}{\lambda^2}[E\cosh(q_2^b z) + F\sinh(q_2^b z)] + \frac{j\lambda_y q_2^a\epsilon_2^z}{\epsilon_2^x\lambda^2}[D\cosh(q_2^a z) + C\sinh(q_2^a z)], \tag{1.22}$$

$$\tilde{H}_x = \frac{j\lambda_x q_2^b}{\lambda^2}[F\cosh(q_2^b z) + E\sinh(q_2^b z)] - \frac{\omega\epsilon_o\epsilon_2^z\lambda_y}{\lambda^2}[C\cosh(q_2^a z) + D\sinh(q_2^a z)], \tag{1.23}$$

$$\tilde{H}_y = \frac{j\lambda_y q_2^b}{\lambda^2}[F\cosh(q_2^b z) + E\sinh(q_2^b z)] + \frac{\omega\epsilon_o\epsilon_2^z\lambda_x}{\lambda^2}[C\cosh(q_2^a z) + D\sinh(q_2^a z)], \tag{1.24}$$

where

$$q_2^a = \sqrt{\frac{\epsilon_2^x}{\epsilon_2^z}(\lambda^2 - \epsilon_2^z k_o^2\mu_2)} \tag{1.25}$$

$$q_2^b = \sqrt{\lambda^2 - \epsilon_2^z k_o^2\mu_2)}. \tag{1.26}$$

In region 0, $h \le z$,

$$\tilde{E}_z = Ge^{-q(z-h)}, \tilde{H}_z = He^{-q(z-h)}, \tag{1.27}$$

$$\tilde{E}_x = (\frac{\omega\mu_o\lambda_y}{\lambda^2}H - \frac{j\lambda_x q}{\lambda^2}G)e^{-q(z-h)} \tag{1.28}$$

$$\tilde{E}_y = (\frac{-\omega\mu_o\lambda_x}{\lambda^2}H - \frac{j\lambda_y q}{\lambda^2}G)e^{-q(z-h)} \tag{1.29}$$

$$\tilde{H}_x = (\frac{-j\lambda_x q}{\lambda^2}H - \frac{\omega\epsilon_o\lambda_y}{\lambda^2}G)e^{-q(z-h)} \tag{1.30}$$

$$\tilde{H}_y = (\frac{-j\lambda_y q}{\lambda^2}H + \frac{\omega\epsilon_o\lambda_x}{\lambda^2}G)e^{-q(z-h)}, \tag{1.31}$$

where

$$q = \sqrt{\lambda^2 - k_o^2} \tag{1.32}$$

and

$$\lambda = \sqrt{\lambda_x^2 + \lambda_y^2}. \tag{1.33}$$

For an $\hat{x}$ directed δ source at $x = x\prime$, $y = y\prime$, with the source located at the material interface, one has

$$\tilde{H}_y(z = b^+) - \tilde{H}_y(z = b^-) = -1. \tag{1.34}$$

If the source is located at the air-dielectric interface, one has

$$\tilde{H}_y(z = h^+) - \tilde{H}_y(z = h^-) = -1. \tag{1.35}$$

Other tangential field components are continuous across each interface. By enforcing these boundary conditions and after some algebraic manipulations, one can obtain a system of linear equations in the form:

$$\begin{bmatrix} \frac{\mu_1}{\mu_2}\tanh(q_1^b b) & -\cosh(q_2^b b) & -\sinh(q_2^b b) & 0 \\ -q_1^b & q_2^b \sinh(q_2^b b) & q_2^b \cosh(q_2^b b) & 0 \\ 0 & 1 & \tanh(q_2^b h) & -1/\mu_2 \\ 0 & q_2^b \tanh(q_2^b h) & q_2^b & q \end{bmatrix} \begin{bmatrix} B \\ E \\ F \\ H \end{bmatrix} = [V_1] \tag{1.36}$$

$$\begin{bmatrix} -q_1^a \epsilon_1^z/\epsilon_1^z \tanh(q_1^a b) & \sinh(q_2^a b) q_2^a \epsilon_2^z/\epsilon_2^z & \cosh(q_2^a b) q_2^a \epsilon_2^z/\epsilon_2^z & 0 \\ \epsilon_1^z & -\epsilon_2^z \cosh(q_2^a b) & -\epsilon_2^z \sinh(q_2^a b) & 0 \\ 0 & \tanh(q_2^a h) q_2^a \epsilon_2^z/\epsilon_2^z & q_2^a \epsilon_2^z/\epsilon_2^z & q \\ 0 & \epsilon_2^z & \tanh(q_2^a h)\epsilon_2^z & -1 \end{bmatrix} \begin{bmatrix} A \\ C \\ D \\ G \end{bmatrix} = [V_2] \tag{1.37}$$

For the case where the source is located at z = b, the excitation matrix is

$$[V_1] = \begin{bmatrix} 0 \\ j\lambda_y \\ 0 \\ 0 \end{bmatrix} \; and \; [V_2] = \begin{bmatrix} 0 \\ \lambda_x/\omega\epsilon_o \\ 0 \\ 0 \end{bmatrix}. \tag{1.38}$$

While for the case where the source is located at z = h, the excitation matrix is

$$[V_1] = \begin{bmatrix} 0 \\ 0 \\ 0 \\ -j\lambda_y \end{bmatrix} and [V_2] = \begin{bmatrix} 0 \\ 0 \\ 0 \\ \lambda_x/\omega\epsilon_o \end{bmatrix}. \tag{1.39}$$

The coefficients of the Fourier transformed fields can be found by inverting the matrix in Eq. 1.36 and 1.37. From these coefficients and Eqs. 1.5, 1.13- 1.33, the electromagnetic fields in the entire half space due to an infinitesimal electric dipole (Green's function) can be found.

1.2 The Method of Moments

Assuming that the current is flowing in the x direction on the dipole, the pertinent integral equation is

$$E_x = \int_{-w/2}^{w/2} \int_0^L G_{xx}(x - x',\, y - y') J_x(x',\, y') dx' dy', \tag{1.40}$$

where G_{xx} is the Green's function and is in the form:

$$G_{xx}(x - x',\, y - y') = \frac{1}{4\pi^2} \int_{-\infty}^{\infty} \int_{-\infty}^{\infty} \tilde{G_{xx}}(\lambda_x,\, \lambda_y) e^{j\lambda_x(x-x')}\, e^{j\lambda_y(y-y')} d\lambda_x\, d\lambda_y. \tag{1.41}$$

The Fourier component $\tilde{G_{xx}}$ is exactly the expression of Eq. 1.21 with either z = b (dipole at the material interface) or z = h (dipole at the air-dielectric interface). In the method of moments procedure, the current on the dipole is expanded in terms of a set of overlapped piecewise sinusoidal functions and a Maxwellian function [1]. By assuming that the dipole length L is (N + 1)d and employing the method of moments followed by a Galerkin's procedure, the integral equation is discretized into a system of linear equations which may be expressed in matrix form as $[Z][I] = [V]$, where the elements of [Z] can be written as

$$Z_{mn} = \int_0^{\infty} \tilde{j_x}^2(\lambda_x) \cos[\lambda_x(m - n)d] d\lambda_x \int_0^{\infty} \tilde{G_{xx}}(\lambda_x,\, \lambda_y) J_o^2(\lambda_y w/2) d\lambda_y \tag{1.42}$$

with

$$\tilde{j_x}(\lambda_x) = 2k_e \frac{\cos \lambda_x d - \cos k_e d}{k_e^2 - \lambda_x^2}. \tag{1.43}$$

The impedance matrix elements are evaluated by a newly developed method which is described in a later chapter [6]. This scheme computes the double infinite integral in a rectangular-form.

The elements in the excitation matrix [V] are

$$V_n = < f_n, E_x > \tag{1.44}$$

where n = 1, 2, 3, ... For a center-fed dipole, supposing that N is odd, one has

$$V_{(N+1)/2} = 1 \tag{1.45}$$

and $V_k = 0$ elsewhere. The input impedance of the center-fed dipole is defined as

$$Z_{in} = V_{(n+1)/2} / I_{(n+1)/2} \tag{1.46}$$

1.3 Antenna Gain and Radiation Efficiency

Once the current in the dipole and the Green's function are known, it is possible to find the corresponding electromagnetic fields in the far zone.

The tangential electric fields at the air-material interface (z=h) can be written as

$$\vec{E}(x,\, y,\, z=h) = \frac{1}{4\pi^2}\int_{-\infty}^{\infty}\int_{-\infty}^{\infty} \tilde{E}(\lambda_x,\, \lambda_y) e^{j\lambda_x x + j\lambda_y y}\, d\lambda_x\, d\lambda_y, \tag{1.47}$$

where

$$\tilde{E}(\lambda_x,\, \lambda_y) \;=\; \tilde{E}_x(\lambda_x,\, \lambda_y)\hat{x} \;+\; \tilde{E}_y(\lambda_x,\, \lambda_y)\hat{y}. \tag{1.48}$$

$\tilde{E}(\lambda_x,\, \lambda_y)$, a vector quantity, is the multiplication of the spectral dyadic Green's function and the Fourier transform of the current in the dipole. The far zone electric fields are related to the tangential spectral electric fields through the formulae [5, p.67]

$$E_\phi \;=\; jk_0\frac{e^{-jk_0R}}{2\pi R}\left[\tilde{E}_y(k_x,\, k_y)\cos\phi - \tilde{E}_x(k_x,\, k_y)\sin\phi\right], \tag{1.49}$$

$$E_\theta \;=\; jk_0\frac{e^{-jk_0R}}{2\pi R}\left[\tilde{E}_x(k_x,\, k_y)\cos\phi + \tilde{E}_y(k_x,\, k_y)\sin\phi\right], \tag{1.50}$$

where

$$k_x \;=\; k_0\sin\theta\cos\phi \tag{1.51}$$

and

$$k_z \;=\; k_0\sin\theta\sin\phi \tag{1.52}$$

The power density in space is given as

$$P_o = \frac{1}{240\pi}\left[|\, E_\theta\,|^2 \;+\; |\, E_\phi\,|^2\right], \tag{1.53}$$

while the total radiated power is

$$P_{rad} = \int_0^{\pi/2}\int_0^{2\pi} P_o(\theta,\, \phi)R^2\sin\theta d\phi d\theta. \tag{1.54}$$

The transmit gain of the dipole is given by

$$\text{gain}(\theta,\, \phi) = \frac{P_o(\theta,\, \phi)4\pi R^2}{P_{rad}}, \tag{1.55}$$

and in Db,

$$\text{gain}_{Db}(\theta,\, \phi) = 10\log_{10}\text{gain}(\theta,\, \phi). \tag{1.56}$$

The radiation efficiency is defined as

$$\eta \;=\; \frac{P_{rad}}{P_{tot}}, \tag{1.57}$$

where

$$P_{tot} = \frac{1}{2} R_{in} |I_{in}|^2 \tag{1.58}$$

For a lossless material the total input power is the sum of the radiated power and the power due to surface waves.

1.4 Results

In this section, the effects of material anisotropy on printed circuit antenna characteristics are presented through an accurate numerical computation. For practical applications, printed antennas are usually covered with a protective layer. This is the configuration studied in this research. Interesting phenomena for printed antenna characteristics due to the presence of the cover layer are described in [2]. The results presented here focus on the effects of either substrate or superstrate anisotropy. As was discussed in [3], many practical integrated circuit substrates exhibit strong anisotropy due to either their nature or what is introduced in the manufacturing process. Epsilam-10 ($\epsilon_x = 10.2$ and $\epsilon_z = 13$), Sapphire ($\epsilon_x = 9.4$ and $\epsilon_z = 11.6$) and PTFE(CuClad) ($\epsilon_x = 2.43$ and $\epsilon_z = 2.88$) are examples of these materials.

Typical printed antenna gain is about 6 Db. Figure 1.2 shows the broadside ($\theta = 0$) gain as a function of frequency with Sapphire as a substrate. The solid line is for the case of neglecting the substrate anisotropy, while the dash line is for the case of including the substrate anisotropy. It is seen from Figure 1.2 that the substrate anisotropy has little effect on the antenna gain in almost the entire frequency range. On the other hand, the superstrate anisotropy has strong effects on the gain performance as illustrated in Figure 1.3, where the anisotropic material (Sapphire) is used as the superstrate. The deep valleys occurring in both Figures 1.2 and 1.3 are due to the resonance of the layered structure. This resonance behavior can be explained in terms of a transmission line equivalence model [2].

Microstrip structures support surface waves, of which the lowest order mode has zero cutoff frequency. For printed circuit antenna applications, the surface wave power is considered loss since all the power is intended for radiation into free space. The radiation efficiency characteristics can be used to examine the percentage of power loss due to the surface waves as compared to the total power emanating from the antenna element. These surface waves propagating horizontally are usually undesirable except for special prescribed applications. Figure 1.4 shows radiation

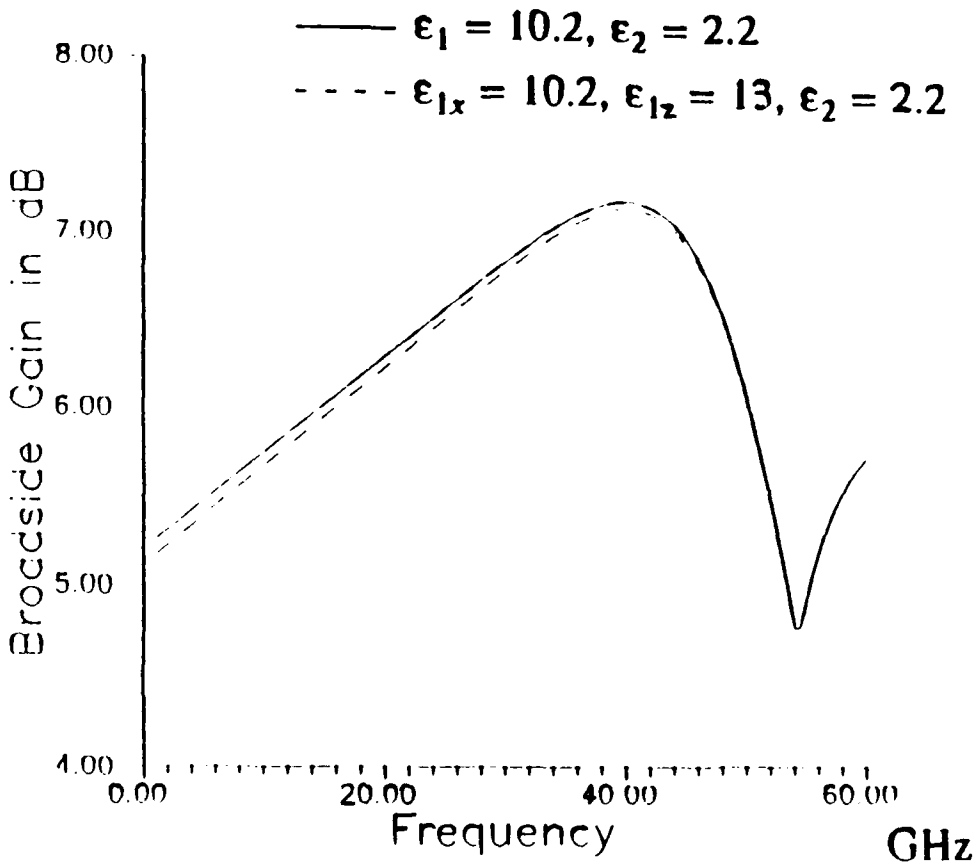

Figure 1.2: Broadside Gain Versus Frequency. Antenna Is at the Material Interface with h = 0.08 cm, and b = 0.04 cm. The substrate is anisotropic (Sapphire).

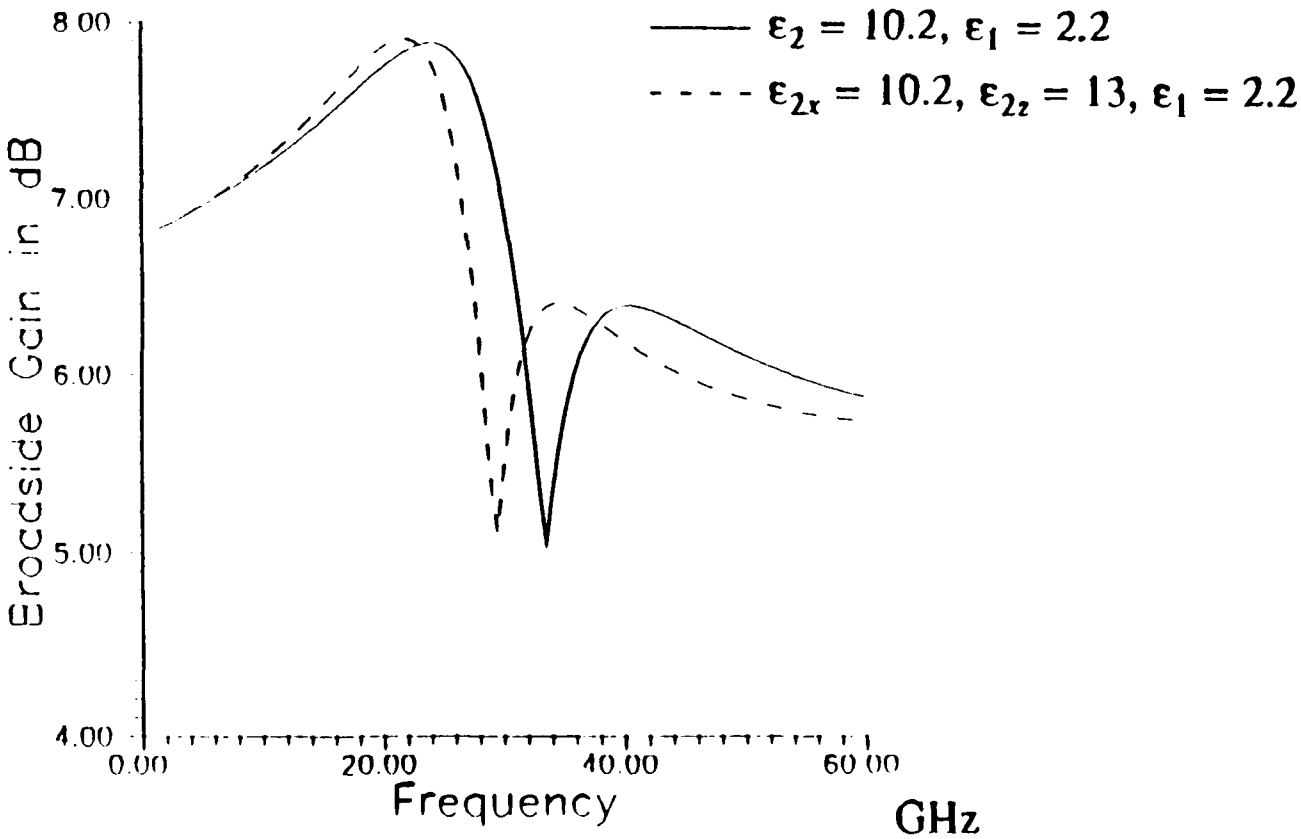

Figure 1.3: Broadside Gain versus Frequency. The antenna is at the material interface with h = 0.08 cm, and b = 0.04 cm. The superstrate is anisotropic (Sapphire).

efficiency as a function of material thickness with and without the substrate or superstrate anisotropy. It is seen that material anisotropy does not affect the efficiency much. This is due to the fact that both surface wave power and radiation resistance increase or decrease together when the material constants change.

The effects of the substrate anisotropy on the input impedance of a center-fed printed dipole are shown in Figures 1.5 and 1.6. In these figures, two cases are considered. One is for the case where both the substrate and superstrate are isotropic ($\epsilon_1 = 2.43$ and $\epsilon_2 = 2.2$). The other is for the case of an isotropic superstrate ($\epsilon_2 = 2.2$) and a substrate with anisotropy in the z (vertical) direction ($\epsilon_{1x} = 2.43$ and $\epsilon_{1z} = 2.88$). In addition to the change in the resonant length, the resonant resistance changes about 10% which is rather significant. This implies that the neglect of the material anisotropy can lead to an unexpected and severe input mismatch. It is also seen that away from the dipole resonance, the material anisotropy has no significant effect. The resonant length of a center-fed dipole is also an important parameter for the antenna designer. Figure 1.7 shows the dipole resonant length as a function of the layer thickness (or frequency) with and without substrate anisotropy. The materials used in this illustration are Epsilam ($\epsilon = 10.2$) substrate and Duroid ($\epsilon = 2.2$) superstrate. It is found that neglecting the substrate anisotropy results in an error in the resonant length of more than 10%. The decrease for the resonant length due to the substrate anisotropy is because the material anisotropy in the z direction increases the effective dielectric constant of the substrate. It is also noted that the increase of the layer thickness (or frequency) results in the decrease of the dipole resonant length.

From all the above observations, it is clear that the material anisotropy has significant effects on the near fields and current distributions of printed antennas.

1.4.1 Conclusion

In this work, we have developed accurate computer codes for analyzing two-layer printed antenna structures capable of including the effect of material anisotropy. The computer codes include both near field and far field computations. It has been found that the material anisotropy has strong effects on the printed antenna performance especially when the near fields are considered. The parameters that are affected significantly include input impedance and resonant length of the antennas.

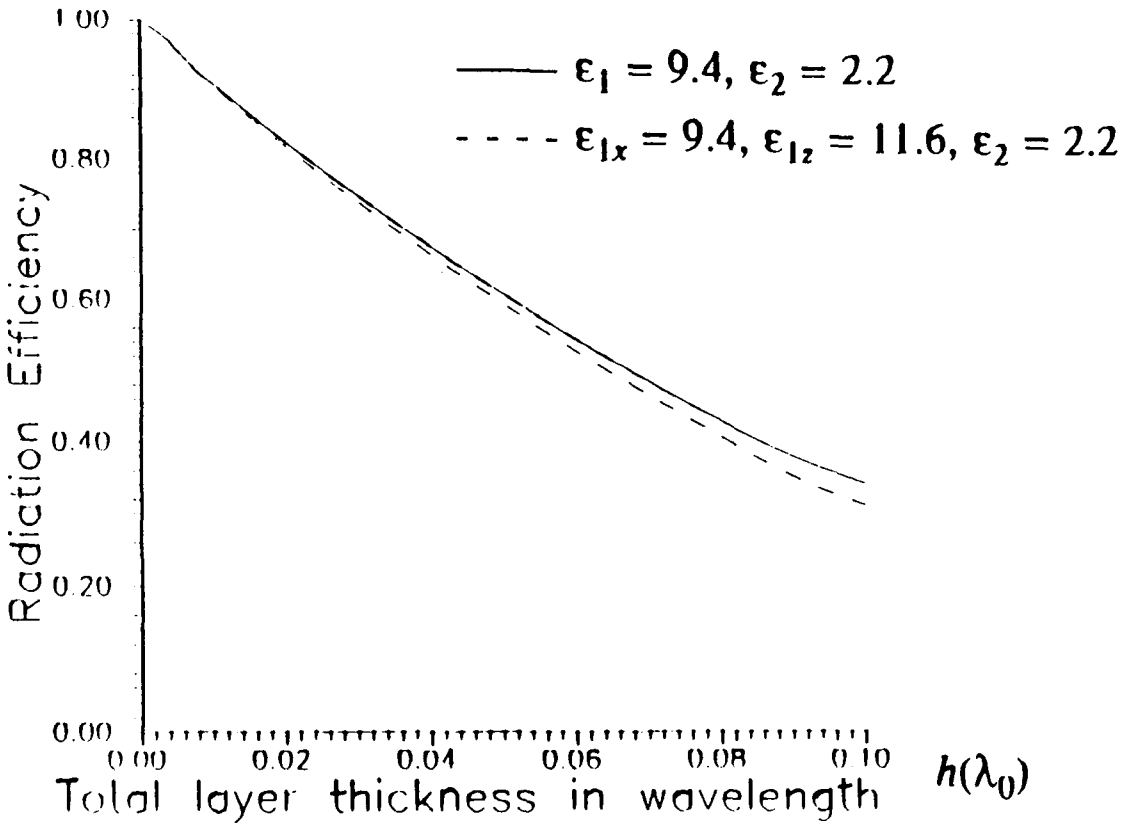

Figure 1.4: Radiation Efficiency versus Material Thickness. The antenna is at the material interface with h = 2b.

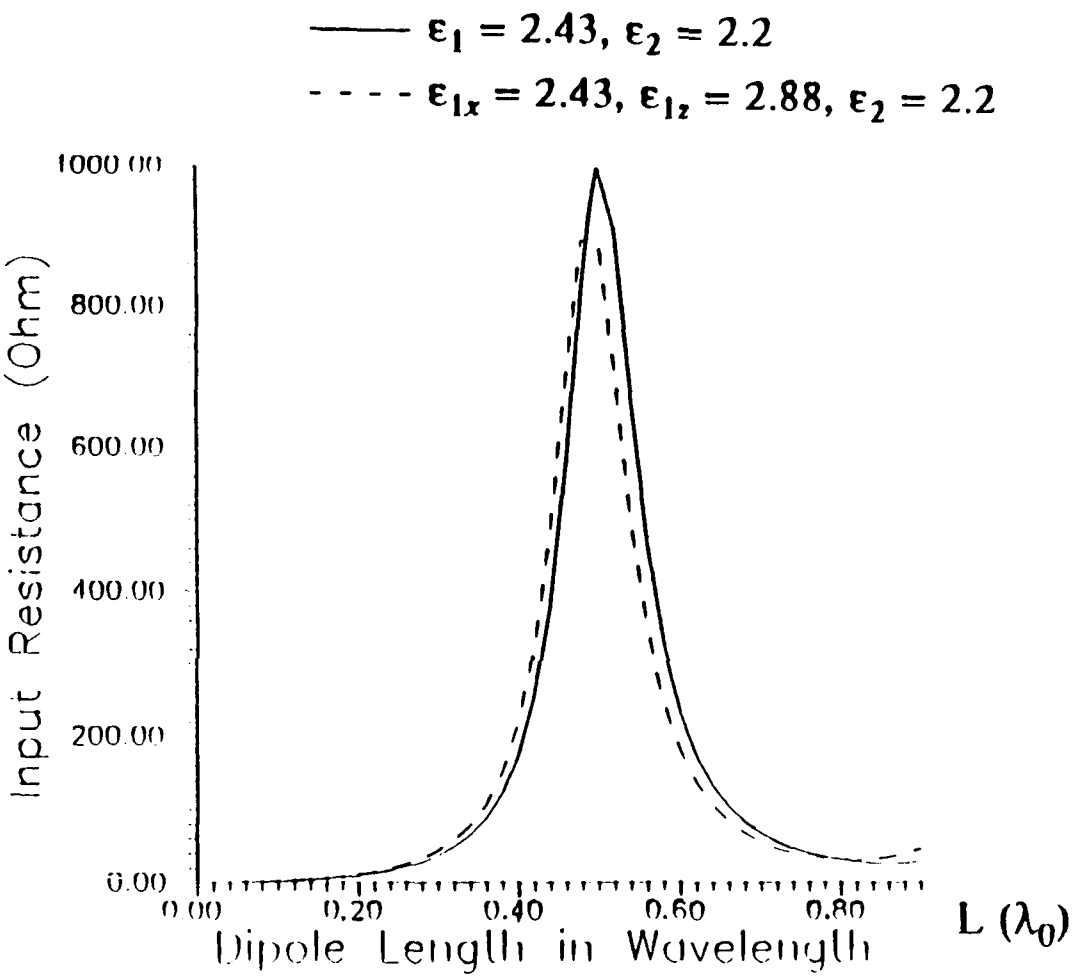

Figure 1.5: Input Resistance of a Center-fed Dipole. The antenna is at the material interface with h = 0.2 λ_0, b = 0.1 λ_0, and w/h = 0.05 .

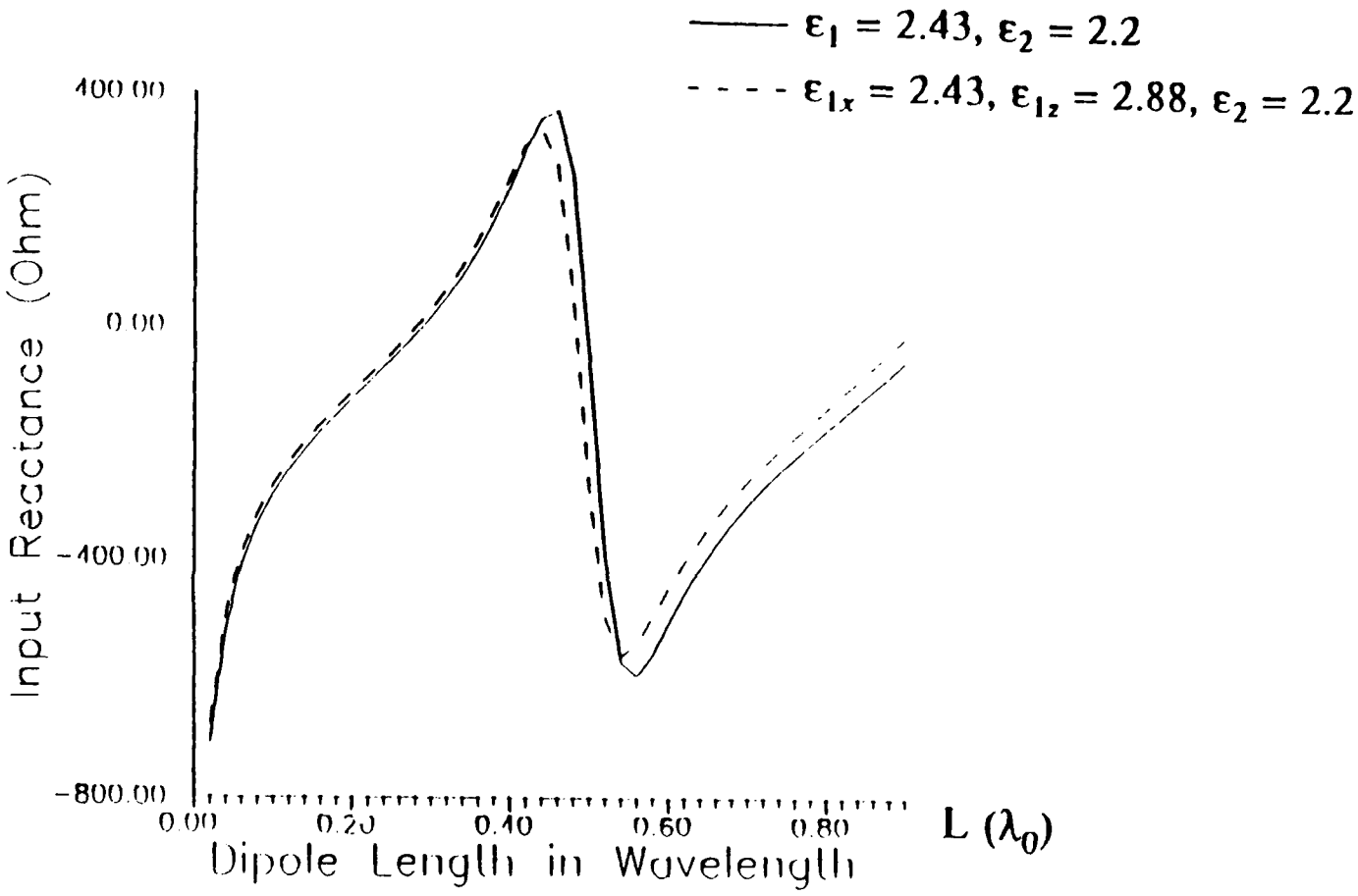

Figure 1.6: Input Reactance of a Center-fed Dipole. The antenna is at the material interface with h = 0.2 λ_0, b = 0.1 λ_0, and w/h = 0.05 .

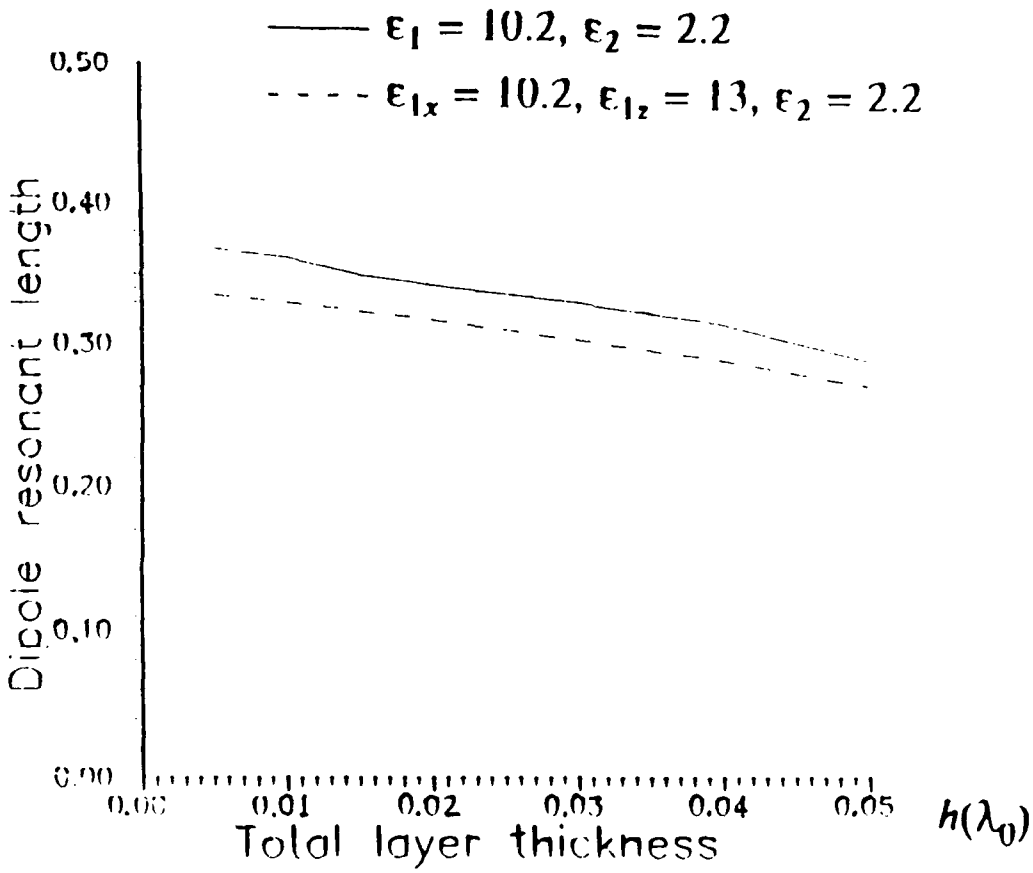

Figure 1.7: Dipole Resonant Length versus Material Thickness. The antenna is at the material interface with h = 2b and w = 0.05 h.

Chapter 2

Microstrip Dipoles on Gyrotropic Substrates

The characteristics of a microstrip dipole on/in a gyrotropic substrate are investigated. As in the case of uniaxial permittivity, the boundary value problem is formulated as an integral equation that is solved by the method of moments. The Green's function, which is central in the solution, is represented in the spectral domain. A numerical technique for generating the Green's function is described. The new algorithm for the evaluation of the double infinite spectral integral is used. The details of that algorithm are presented in Chapter 4. Radiation patterns (transmit gain patterns) are presented for the case of a dipole on a biased ferrite substrate. Although the development of the Green's function is detailed for the single general anisotropic layer substrate, the matrix method can be easily applied to the problem of multiple anisotropic layers. Computed results for the case of an isotropic substrate with a gyrotropic (biased ferrite) cover layer are presented. Those results illustrate the use of the biased ferrite substrates or cover layers for element pattern shaping, element pattern beam steering, and element gain enhancement.

2.1 Introduction

The printed circuit antenna is an attractive antenna structure for its conformability, low profile, light weight, and low cost [7,8]. It has been demonstrated in [1,2] that the material constants and thickness are critical to the performance of the printed circuit antenna. Also, the frequency range of operation is limited (narrow band); once the structure is built, it is not possible to change the antenna

characteristics and frequency band of operation.

By using biased ferrite substrates in microstrip structures one can, by way of the applied bias dc magnetic field, change the permeability tensor and thus the electrical properties of the material. It is possible to change and control the antenna characteristics dynamically without changing the physical structure.

2.2 Theory

2.2.1 Material Characteristics of Ferrites

Ferrite materials have been extensively used in microwave devices due to their non-reciprocal electrical properties. The magnetic properties of ferrites arise mainly from the magnetic dipole moment associated with the electron spin. The fundamental physics of ferrites have been well discussed in the literature, as for example in [9,10]. In this section, we summarize the material properties of ferrites in terms of a permeability tensor which is suitable for the study of the wave propagation problems.

For a z directed dc bias, the permeability tensor of a ferrite material is

$$\vec{\bar{\mu}} = \mu_0 \begin{bmatrix} \mu & j\kappa & 0 \\ -j\kappa & \mu & 0 \\ 0 & 0 & 1 \end{bmatrix}, \tag{2.1}$$

where

$$\mu = 1 + \frac{\omega_0 \omega_m}{\omega_0^2 - \omega^2}, \tag{2.2}$$

$$\kappa = \frac{\omega \omega_m}{\omega_0^2 - \omega^2}, \tag{2.3}$$

$$\omega_0 = \gamma \mu_0 H_0, \tag{2.4}$$

$$\omega_m = \gamma \mu_0 M_s, \tag{2.5}$$

$$\gamma = 1.759 \times 10^{-11}\ \mathrm{kg}/coul, \tag{2.6}$$

ω is the a.c. operating frequency, M_s is material saturation magnetization, and H_0 is the dc bias magnetic field. For the geometry shown in Figure 2.1, the planar ferrite slab is parallel to the x-y plane. The dc bias H field is, for practicality, taken to be in the planar direction. For such cases, the permeability tensor is

$$\vec{\bar{\mu}} = \mu_0 \begin{bmatrix} \mu + (\mu_0 - \mu)\cos^2\phi_0 & \frac{\mu_0 - \mu}{2}\sin 2\phi_0 & -j\kappa \sin\phi_0 \\ \frac{\mu_0 - \mu}{2}\sin 2\phi_0 & \mu + (\mu_0 - \mu)\sin^2\phi_0 & j\kappa\cos\phi_0 \\ j\kappa\sin\phi_0 & -j\kappa\cos\phi_0 & \mu \end{bmatrix}, \tag{2.7}$$

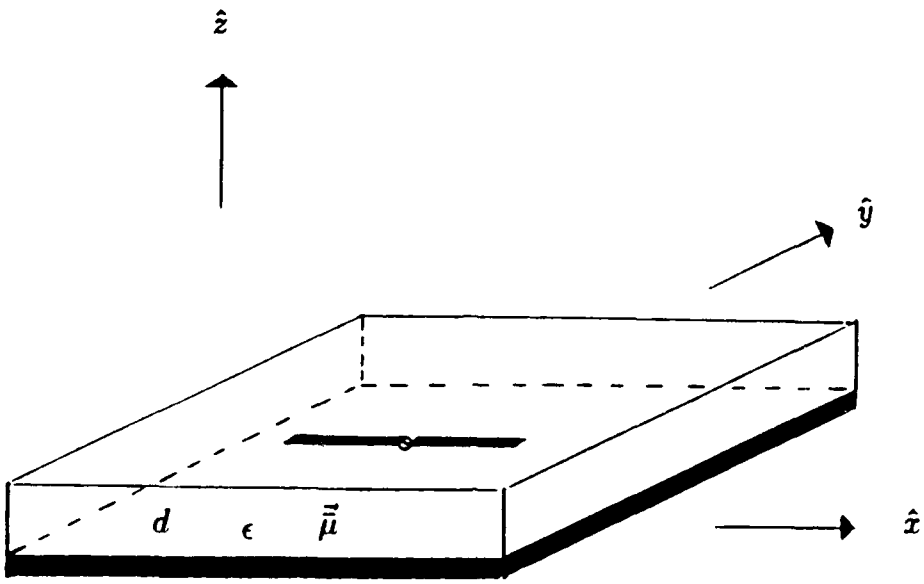

Figure 2.1: A Microstrip Dipole on a Ferrite Substrate

where ϕ_0 is the angle of the direction of the dc bias H field measured from the x axis.

It can be seen from Eqs. 2.1 - 2.7 that the permeability tensor for a ferrite is determined by an inherent material property (saturation magnetization), the strength and angle of the input bias H field, as well as the operating frequency.

2.2.2 Green's Function for a Grounded Ferrite

In dealing with the Green's function for a grounded ferrite, no more difficulty is introduced by considering both permittivity and permeability as anisotropic. With this generalization, both the permittivity and permeability are tensor forms, which in a rectangular Cartesian coordinate system are expressed as:

$$\vec{\bar{\mu}} = \mu_0 \begin{bmatrix} \mu_{xx} & \mu_{xy} & \mu_{xz} \\ \mu_{yx} & \mu_{yy} & \mu_{yz} \\ \mu_{zx} & \mu_{zy} & \mu_{zz} \end{bmatrix} \text{ and } \vec{\bar{\epsilon}} = \epsilon_0 \begin{bmatrix} \epsilon_{xx} & \epsilon_{xy} & \epsilon_{xz} \\ \epsilon_{yx} & \epsilon_{yy} & \epsilon_{yz} \\ \epsilon_{zx} & \epsilon_{zy} & \epsilon_{zz} \end{bmatrix}. \tag{2.8}$$

Then Maxwell's equations for the fields inside the ferrite slab ($0 < z < d$) with no source are

$$\nabla \times \vec{E} = -j\omega\vec{\bar{\mu}} \cdot \vec{H} \text{ and } \nabla \times \vec{H} = j\omega\vec{\bar{\epsilon}} \cdot \vec{E}. \tag{2.9}$$

Introducing the following Fourier transformation

$$\begin{matrix} \vec{E} \\ \vec{H} \end{matrix} = \frac{1}{4\pi} \int_{-\infty}^{\infty} \begin{matrix} \tilde{E} \\ \tilde{H} \end{matrix} (k_x, k_y)\, e^{-jk_x x}\, e^{-jk_y y}\, dk_x\, dk_y, \tag{2.10}$$

and using Eq. 2.9, one obtains

$$-j\mathbf{k} \times \tilde{H} + \frac{\partial}{\partial z}(\hat{z} \times \tilde{H}) = j\omega\vec{\bar{\epsilon}} \cdot \tilde{E} \tag{2.11}$$

and

$$-j\mathbf{k} \times \tilde{E} + \frac{\partial}{\partial z}(\hat{z} \times \tilde{E}) = -j\omega\vec{\bar{\mu}} \cdot \tilde{H}, \tag{2.12}$$

with $\mathbf{k} = k_x\hat{x} + k_y\hat{y}$ and $\tilde{E}$ and $\tilde{H}$ are the spectral electric and magnetic fields, respectively, more over

$$\tilde{E} = \tilde{E}_x\hat{x} + \tilde{E}_y\hat{y} + \tilde{E}_z\hat{z} \tag{2.13}$$

and

$$\tilde{H} = \tilde{H}_x\hat{x} + \tilde{H}_y\hat{y} + \tilde{H}_z\hat{z}. \tag{2.14}$$

After some algebraic manipulations, Eqs. 2.11 - 2.12 can be written in the form of a set of linear differential equations, as

$$\frac{\partial}{\partial z}[\tilde{\psi}(z)] = [A]\,[\tilde{\psi}(z)] \tag{2.15}$$

where

$$[\tilde{\psi}(z)] = \begin{bmatrix} k_x\tilde{H}_x(z) + k_y\tilde{H}_y(z) \\ k_y\tilde{H}_x(z) - k_x\tilde{H}_y(z) \\ k_x\tilde{E}_x(z) + k_y\tilde{E}_y(z) \\ k_y\tilde{E}_x(z) - k_x\tilde{E}_y(z) \end{bmatrix} \text{ and } [A] = \begin{bmatrix} a_{11} & a_{12} & a_{13} & a_{14} \\ a_{21} & a_{22} & a_{23} & a_{24} \\ a_{31} & a_{32} & a_{33} & a_{34} \\ a_{21} & a_{42} & a_{43} & a_{44} \end{bmatrix} \tag{2.16}$$

The solution of Eq. 2.15 is

$$[\tilde{\psi}(z_1)] = [T(z_1 - z_2)]\,[\tilde{\psi}(z_2)], \tag{2.17}$$

where

$$[T(z_1 - z_2)] = [\tilde{\phi}] \begin{bmatrix} e^{\lambda_1(z_1-z_2)} & 0 & 0 & 0 \\ 0 & e^{\lambda_2(z_1-z_2)} & 0 & 0 \\ 0 & 0 & e^{\lambda_3(z_1-z_2)} & 0 \\ 0 & 0 & 0 & e^{\lambda_4(z_1-z_2)} \end{bmatrix} [\tilde{\phi}]^{-1}, \tag{2.18}$$

in which the $\lambda_i, i = 1,2,3,4$ are the eigenvalues and $[\tilde{\phi}]$ is a 4×4 eigenvector matrix of [A]. According to the Calley-Hamilton theorem, the matrix $[T(z_1 - z_2)]$ can also be expressed as

$$[T(z_1 - z_2)] = \sum_{n=0}^{3} C_n(z_1 - z_2)[A]^n, \tag{2.19}$$

where the coefficients C_n are given from the solution of the matrix equation

$$e^{\lambda_j(z_1-z_2)} = \sum_{k=0}^{3} \lambda_j^k C_k(z_1 - z_2), \quad j = 1,\ 2,\ 3,\ 4. \tag{2.20}$$

The matrix [T] relates the tangential electromagnetic fields at one surface ($z = z_1$) to another ($z = z_2$). The tangential electromagnetic fields at the air-material interface can now be related to those at the ground plane as

$$[\tilde{\psi}(d^-)] = [T(d)]\,[\tilde{\psi}(0)] \tag{2.21}$$

The electromagnetic fields in the air ($z \geq d$) can be derived in a straightforward manner. With this result together with the boundary conditions that the tangential electric fields are zero at the ground plane, one obtains

$$[\tilde{\psi}(d^+)] = \begin{bmatrix} j\sqrt{k^2 - k_0^2}\,\tilde{a} \\ \omega\epsilon_0\,\tilde{b} \\ j\sqrt{k^2 - k_0^2}\,\tilde{b} \\ -\omega\mu_0\,\tilde{a} \end{bmatrix} \text{ and } [\tilde{\psi}(0)] = \begin{bmatrix} \tilde{c} \\ \tilde{d} \\ 0 \\ 0 \end{bmatrix}, \tag{2.22}$$

where $\tilde{a}$, $\tilde{b}$, $\tilde{c}$ and $\tilde{d}$ are unknown spectral quantities to be determined.

With the current source at the air-material interface, the electromagnetic fields just above and below z=d are related as follows:

$$[\tilde{\psi}(d^+)] - [\tilde{\psi}(d^-)] = [U_I], \tag{2.23}$$

where $[U_I]$ is either $[U_x]$ or $[U_y]$ and

$$[U_x] = \begin{bmatrix} -k_y \\ k_x \\ 0 \\ 0 \end{bmatrix} \text{ and } [U_y] = \begin{bmatrix} k_x \\ -k_y \\ 0 \\ 0 \end{bmatrix}. \tag{2.24}$$

$[U_x]$ is for the current source in the x direction, while $[U_y]$ is for the current source in the y direction. Eq. 2.23 involves a 4 by 4 matrix equation, where the solution determines the quantities $\tilde{a}$, $\tilde{b}$, $\tilde{c}$ and $\tilde{d}$. As a result, the spectral Green's function of the pertinent structure is determined.

2.2.3 The Moment Method Solution

The Impedance Matrix Elements

The integral equation for the problem is

$$E_x = \int G_{xx} J_x \, ds \,, \tag{2.25}$$

where the microstrip dipole is oriented in the $\hat{x}$ direction, and is assumed to have current flowing only in the $\hat{x}$ direction. The integral in Eq. 2.25 is a surface integral over the strip dipole. G_{xx} is the Green's function component which is the E_x component due to a δ current source in the x direction. The spectral component of this Green's function has been derived in the previous section.

In the moment method procedure, the current is expanded in terms of a set of known basis functions. For the problem considered the current in the dipole of length $L = (N+1)a$ and width w is conveniently assumed as

$$J_x(x, y) = \sum_{n=1}^{N} I_n j_n(x, y) \tag{2.26}$$

and

$$j_n(x,\, y) \;=\; \frac{f_n(x)}{\pi\sqrt{(w/2)^2 - y^2}}, \tag{2.27}$$

where

$$f_n(x) \;=\; \begin{cases} 1 - \frac{1}{a}|x - na| & ,\ |x - na| \le a \\ 0 & ,\ \text{otherwise.} \end{cases} \tag{2.28}$$

With a standard moment method followed by a Galerkin's procedure, where the same expansion and testing functions are used, the integral equation in Eq. 2.25 is converted into a matrix equation as

$$\sum_{n=1}^{N} I_n\, Z_{mn} \;=\; V_m\,, \quad m = 1,\, 2,\, 3 \ldots N, \tag{2.29}$$

where

$$Z_{mn} = \int_{-w/2}^{w/2}\int_{-w/2}^{w/2}\int_{-L/2}^{L/2}\int_{-L/2}^{L/2} G_{zz}(x, x\prime, y, y\prime)\, j_n(x\prime, y\prime)\, j_m(x, y)\, dx\, dx\prime\, dy\, dy\prime \tag{2.30}$$

and

$$V_m \;=\; \int_{-w/2}^{w/2}\int_{-L/2}^{L/2} E_z(x,\, y) j_m(x,\, y)\; dx\; dy. \tag{2.31}$$

On the strip, however, E_z vanishes except at the delta-gap feed point. Thus, the excitation vector terms are all zero except that element that corresponds to the testing function taken over the delta-gap point:.

$$V_m \;=\; \begin{cases} 1 & ,\ \text{for } m \text{ corresponding to the feed point} \\ 0 & ,\ \text{otherwise.} \end{cases} \tag{2.32}$$

The Green's function and its spectral component is related through the formula:

$$G_{zz}(x,\, x\prime,\, y,\, y\prime) \;=\; \frac{1}{4\pi^2}\int_{-\infty}^{\infty}\int_{-\infty}^{\infty} \tilde{G_{zz}}(k_x,\, k_y)\, e^{-jk_x(x-x\prime)}\, e^{-jk_y(y-y\prime)}\, dk_x\, dk_y \tag{2.33}$$

After inserting Eq. 2.33 into Eq. 2.30 and changing the order of integration, the impedance matrix element Z_{mn} in Eq. 2.30 may be written as

$$Z_{mn} \;=\; \int_{-\infty}^{\infty}\int_{-\infty}^{\infty} \tilde{G_{zz}}(k_x,\, k_y)\, \frac{\sin^4(ak_x/2)}{k_x^4}\, J_0^2(k_y w/2)\, e^{-jk_x(n-m)a}\, dk_x\, dk_y. \tag{2.34}$$

The dipole input impedance is found from the computed current, I_{in}, at the delta-gap feed point:

$$Z_{in} \;=\; R_{in} \;+\; j\, X_{in} \;=\; \frac{1}{I_{in}} \tag{2.35}$$

Far Field Computation

Once the current in the dipole and the Green's function are known, it is possible to find the corresponding electromagnetic fields in the far zone.

The tangential electric fields at the air-material interface (z=d) can be written as

$$\vec{E}(x,\ y,\ z=d) = \frac{1}{4\pi^2}\int_{-\infty}^{\infty}\int_{-\infty}^{\infty}\tilde{E}(k_x,\ k_y)e^{-jk_x x - jk_y y}\,dk_x\,dk_y, \tag{2.36}$$

where

$$\tilde{E}(k_x,\ k_y) \ = \ \tilde{E}_x(k_x,\ k_y)\hat{x} \ + \ \tilde{E}_y(k_x,\ k_y)\hat{y}. \tag{2.37}$$

$\tilde{E}(k_x,\ k_y)$, a vector quantity, is the multiplication of the spectral dyadic Green's function and the Fourier transform of the current in the dipole. The far zone electric fields are related to the tangential spectral electric fields through the formulae [5, p 67]

$$E_\phi \ = \ jk_0\frac{e^{-jk_0R}}{2\pi R}\left[\tilde{E}_y(k_x,\ k_y)\cos\phi - \tilde{E}_x(k_x,\ k_y)\sin\phi\right], \tag{2.38}$$

$$E_\theta \ = \ jk_0\frac{e^{-jk_0R}}{2\pi R}\left[\tilde{E}_x(k_x,\ k_y)\cos\phi + \tilde{E}_y(k_x,\ k_y)\sin\phi\right], \tag{2.39}$$

where

$$k_x \ = \ k_0\sin\theta\cos\phi \tag{2.40}$$

and

$$k_y \ = \ k_0\sin\theta\sin\phi \tag{2.41}$$

The power density in space due to the current in the dipole is given as

$$P_o = \frac{1}{240\pi}\left[|\ E_\theta\ |^2 \ + \ |\ E_\phi\ |^2\right], \tag{2.42}$$

The antenna transmit gain $G_{tr}(\theta,\ \phi)$ is

$$G_{tr}(\theta,\ \phi) \ = \ \frac{4\pi\ P_{tr}(\theta,\phi)}{\int_0^{\pi/2}\int_0^{2\pi}P_{tr}(\theta,\phi)\ d\theta d\phi} \tag{2.43}$$

The receive gain (receiving cross section) must be computed from the results of the scattering problem, since the system is not reciprocal. The scattering problem is addressed in Chapter 3 in connection with the problem of RCS reduction using biased ferrite substrates.

The radiation efficiency, η, for a lossless substrate is

$$\eta \ = \ \frac{\int_0^{\pi/2}\int_0^{2\pi}P_{tr}(\theta,\phi)\ d\theta d\phi}{\frac{1}{2}R_{in}\ |I_{in}|^2} \ = \ 1 \ - \ \frac{P_{sw}}{P_{tot}} \tag{2.44}$$

2.3 Numerical Results

Figures 2.2 and 2.3 are, respectively, E-plane and H-plane transmit gain patterns. The substrate parameters are selected to represent a typical ferrite; the permittivity, ϵ_r, is 12.5, and the saturation magnetization, $\mu_0 M_s$, is taken as 0.25 Tesla. The dipole is oriented in the x direction which is parallel to the $\phi = 0^o$ plane. In each figure two cases are plotted, corresponding to two bias magnetic field directions. The solid thin line curves represent the cases where the biasing magnetic field is y-directed, that is $\phi_o = 90^o$; while the starred line curves represent the cases for which the field is x-directed, $\phi_o = 0^o$.

2.3.1 Element Pattern Shaping, Scanning, and Gain Enhancement

Both for single element antennas and antenna arrays the importance of the element factor to the overall antenna system performance is obvious. In many applications there would be a significant benefit from an element factor with higher gain and shaped radiation patterns. In scanning arrays, an element factor with enhanced off-broadside gain could help to offset the loss in gain that is associated with the decrease in the projected aperture as the beam is scanned off-broadside. With a sufficiently directive element factor a single element could replace an array of elements. If that single highly directive element factor could also be scanned the single element could replace a complete phased array.

As suggested by the results that follow, the microstrip antenna element on a biased ferrite substrate may be used to realize the single element characteristics just described.

Figure 2.4 is a plot of the E-plane directivity pattern of a strip dipole on a biased ferrite substrate. The bias magnetic field is in the plane of the substrate and along the direction of the dipole. The pattern shows the enhanced gain at the off-broadside angles, with approximately the same directivity at 60° as at broadside. The H-plane pattern is plotted in Figure 2.5. It shows a striking reshaping of the element pattern. The pattern is highly directive and the element pattern "beam" goes out at a grazing angle. Those patterns were computed at 30 GHz and for a fixed bias magnetic field of 7150 Gauss. The substrate was 2.0 mm thick and with a relative permittivity of 12.6. The saturation magnetization of the material was 3000 Gauss.

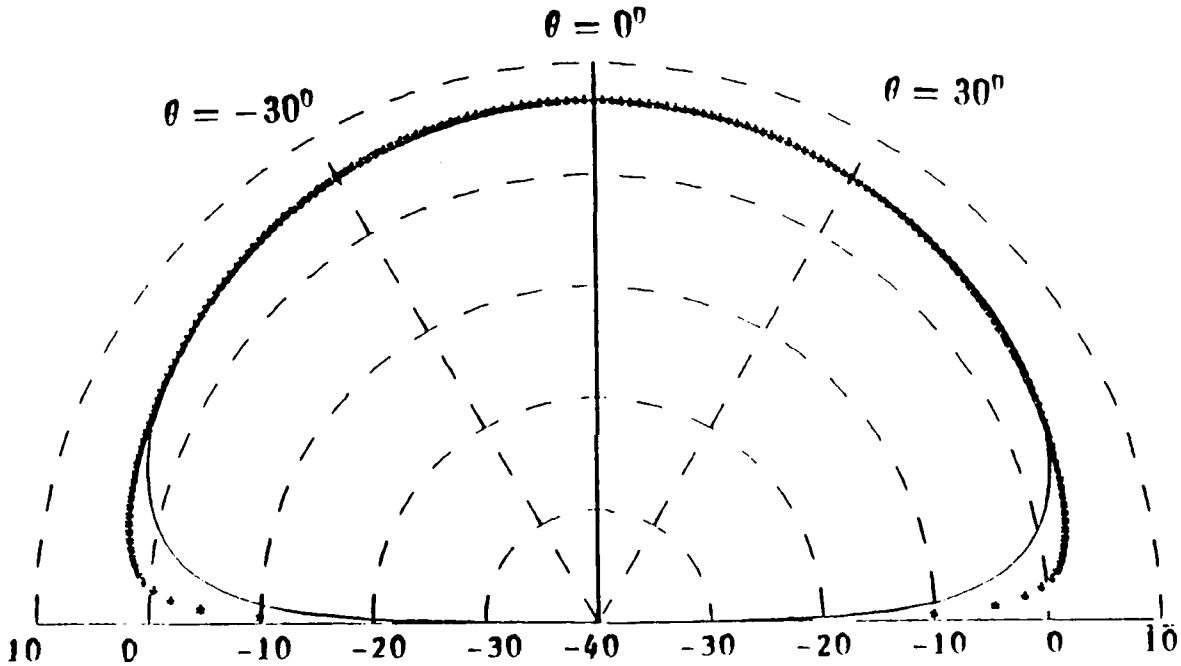

Figure 2.2: E-plane Transmit Gain Pattern for a Center-fed Dipole on a Ferrite Substrate.

The dipole is oriented in the $\phi_o = 0^o$ direction. Substrate thickness = 0.04 λ_o, dipole width = 0.02 λ_o, ϵ_r = 12.5, μ = 0.766, and κ = -0.567 .

Two cases are plotted:

(1) **** the bias field angle is $\phi_o = 0^o$, the dipole resonant length is $l_r = .366\lambda_o$;

(2) — the bias angle is 90°, the dipole resonant length is $l_r = .256\lambda_o$.

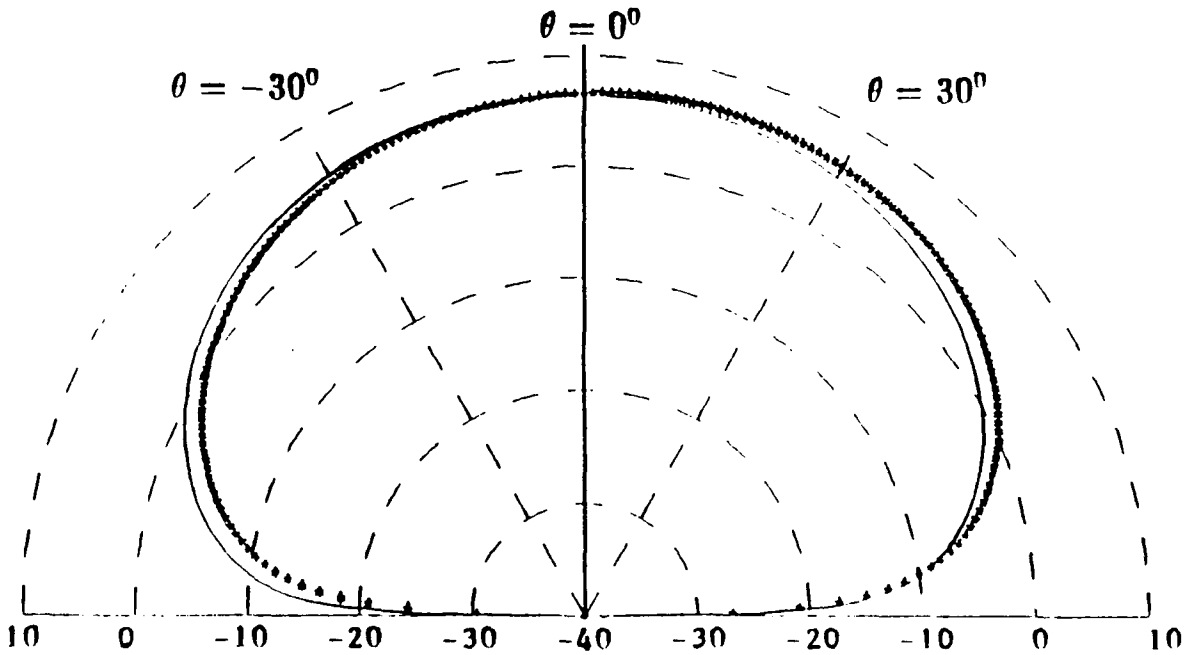

Figure 2.3: H-plane Transmit Gain Pattern for a Center-fed Dipole on a Ferrite Substrate.

The dipole is oriented in the $\phi_o = 0^o$ direction. Substrate thickness = 0.04 λ_o, dipole width = 0.02 λ_o, ϵ_r = 12.5, μ = 0.766, and κ = -0.567 .

Two cases are plotted:

(1) **** the bias field angle is $\phi_o = 0^o$, the dipole resonant length is $l_r = .366\lambda_o$;

(2) — the bias angle is 90°, the dipole resonant length is $l_r = .256\lambda_o$.

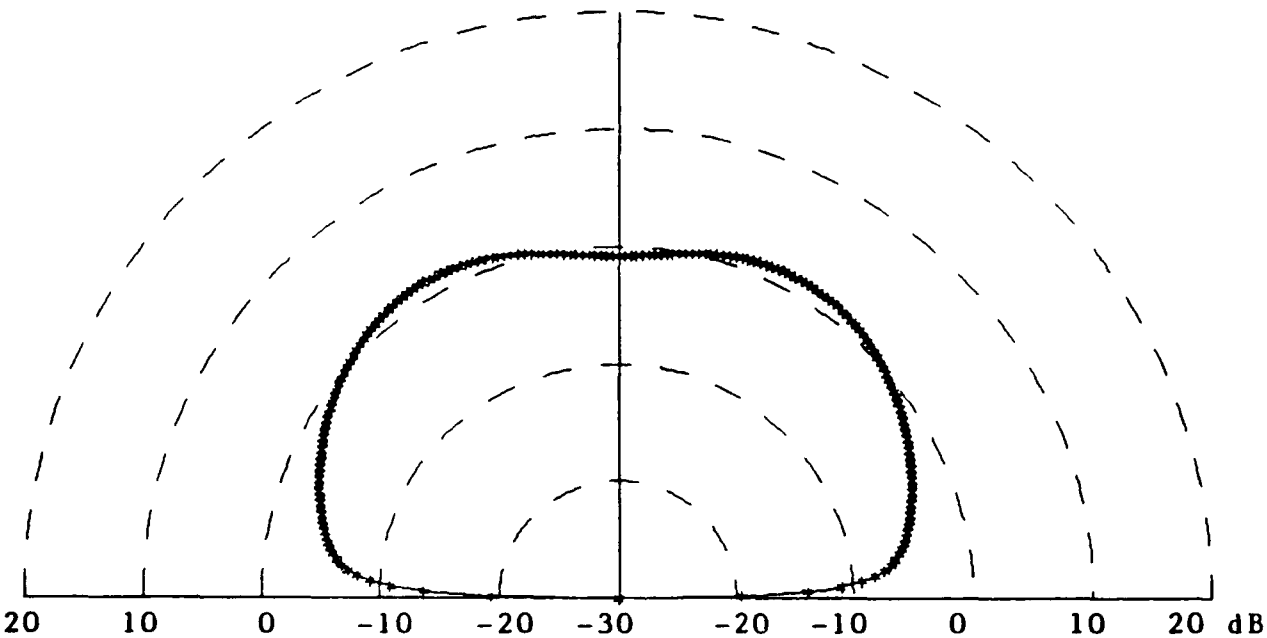

Figure 2.4: E-plane Directivity for a Center-fed Dipole on a Ferrite Substrate.

The frequency is 30 GHz. The bias field is parallel to the dipole.
The substrate thickness is 2.0 mm, and $\epsilon_r = 12.6$.
$H_{dc} = 7150$ Gauss, and $M_s = 3000$ Gauss.

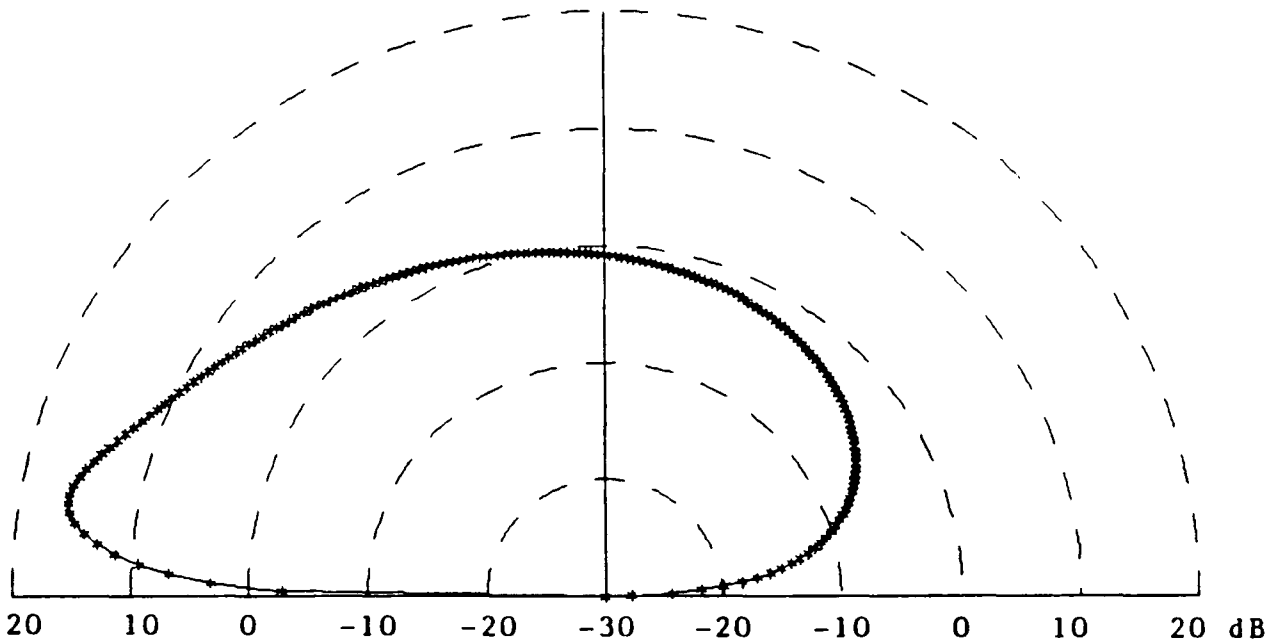

Figure 2.5: H-plane Directivity for a Center-fed Dipole on a Ferrite Substrate.

The frequency is 30 GHz. The bias field is parallel to the dipole.
The substrate thickness is 2.0 mm, and $\epsilon_r = 12.6$.
$H_{dc} = 7150$ Gauss, and $M_s = 3000$ Gauss.

By varying the applied bias magnetic field strength one can vary the patterns of a printed antenna on a ferrite substrate. For the case where the bias field is in the direction of the dipole, the H-plane element pattern "beam" will scan as a function of the applied bias field. This is illustrated in the plot of Figure 2.6, for which the configuration consists of a two layer structure with an isotropic substrate and a biased ferrite cover layer. The isotropic substrate is 1 mm thick with a relative permittivity of 10.0, and a permeability of 1.0. The ferrite cover layer is 3 mm thick with a permittivity of 12.6 and a saturation magnetization (M_s) of 2500 Gauss. The bias magnetic field is directed parallel to the strip dipole. Figure 2.6 is for the fixed frequency of 9 GHz. It is a plot of the element beam pointing angle as a function of the bias field strength. The H-plane patterns for two different bias field strengths are shown in Figure 2.7. Each pattern corresponds to one point in the curve of Figure 2.6. Figure 2.8 is a plot of the beam pointing angle as a function of frequency for a fixed bias field strength $H_{dc} = 1000$ Gauss. From the preliminary computations which have been made it appears that the nonreciprocal properties of the biased ferrite are more apparent when the ferrite is used as a cover layer.

2.3.2 Conclusion

Analyses for microstrip dipole elements on/in gyrotropic (biased ferrite) substrates have been developed using a rigorous moment method solution. The applied bias field can have a significant effect on the electrical performance. The applied bias can be used to dynamically change the dipole characteristics, including resonant frequency and pattern shape. A highly directive element pattern can be achieved. Moreover, the bias magnetic field can be used as a control of the element factor beam direction (peak). This suggests that the structure can be used as an electronically tunable (adaptable) multifunctional system.

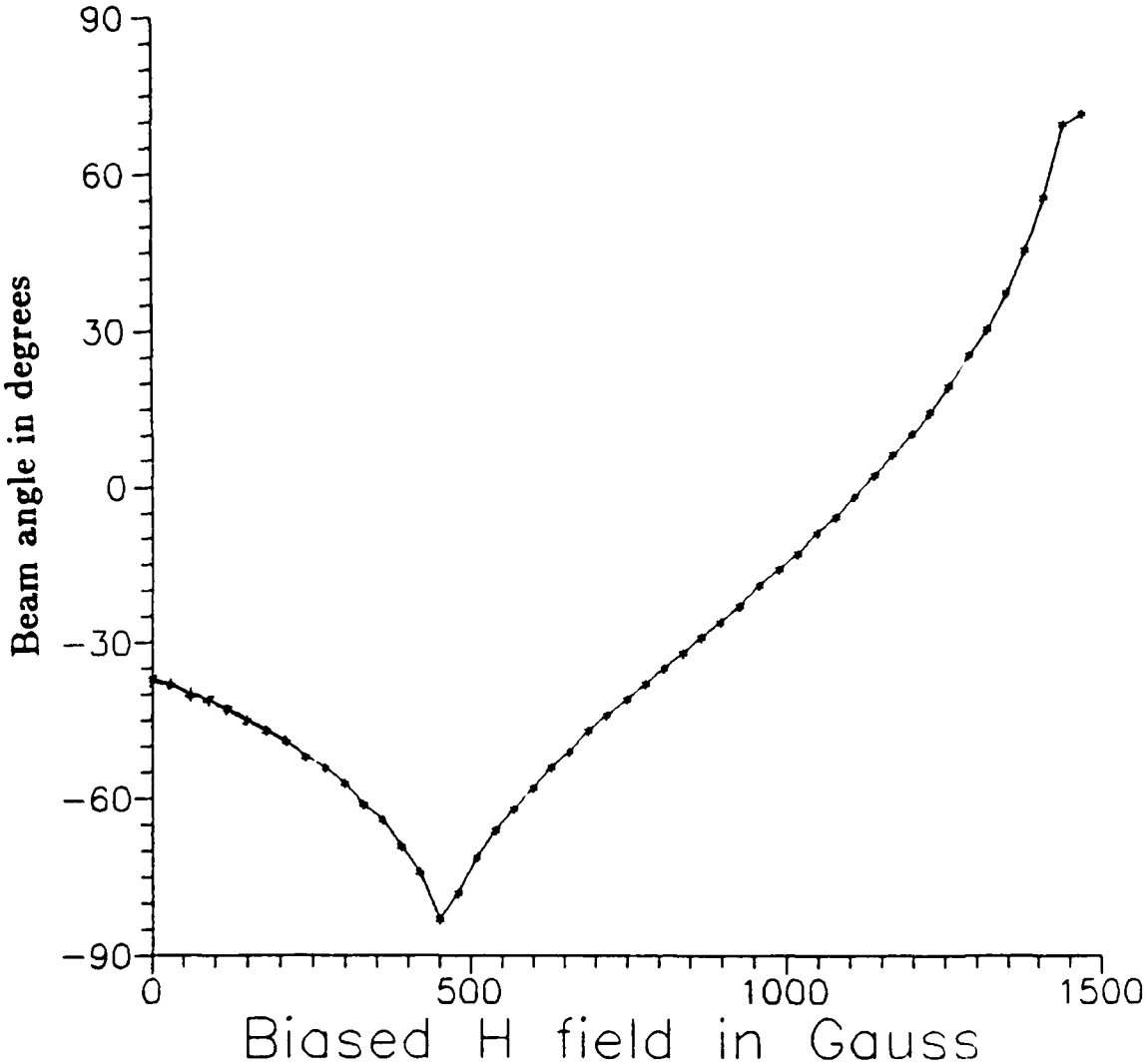

Figure 2.6: H-plane element beam pointing angle as a function of the bias magnetic field strength.

The frequency is 9 GHz. The bias field is parallel to the dipole.
Substrate: thickness = 1.0 mm, $\epsilon_r = 10.0$, and $\mu_r = 1.0$.
Ferrite Cover Layer: thickness = 3.0 mm, $\epsilon_r = 12.6$, $M_s = 2,500G$.

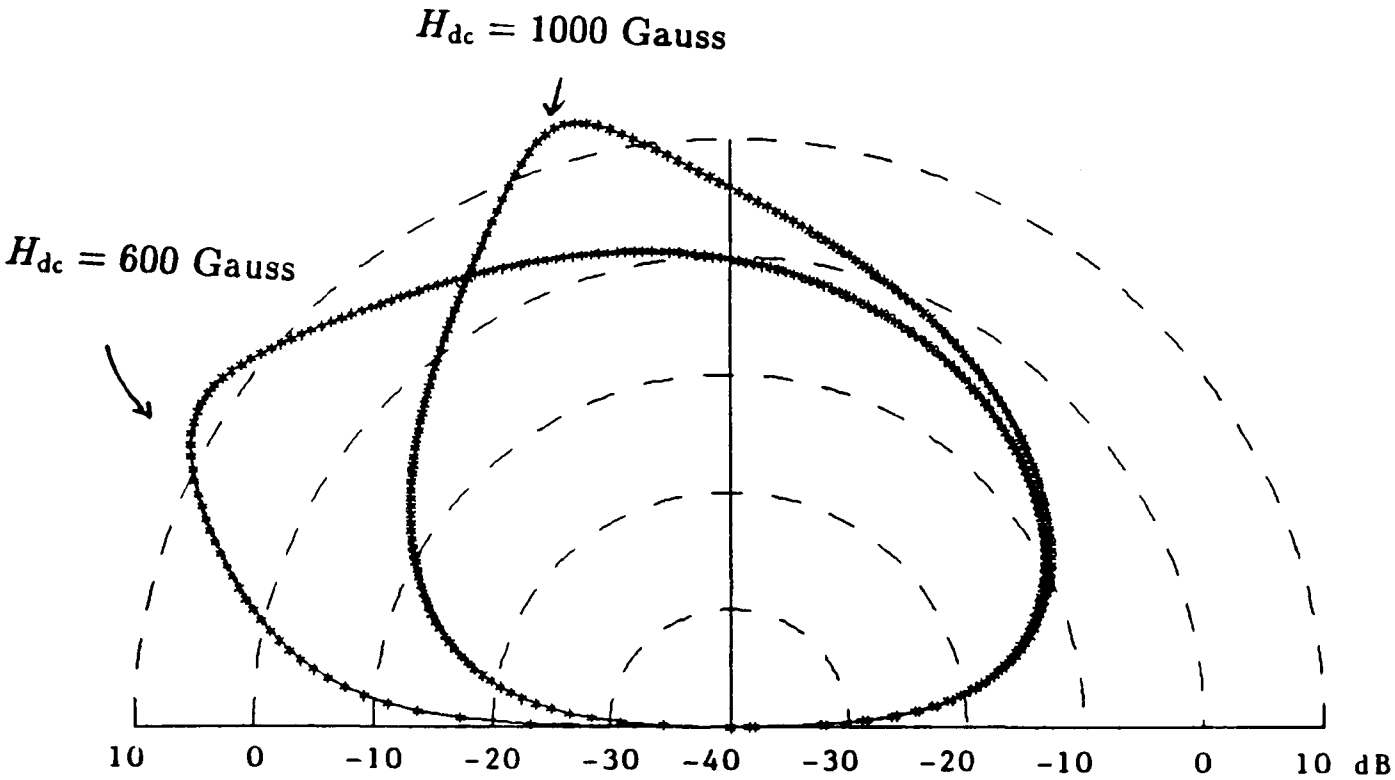

Figure 2.7: H-plane patterns for $H_dc = 600G$ and H_{dc}= 1000 G.

The frequency is 9 GHz. The bias field is parallel to the dipole.
Substrate: thickness = 1.0 mm, ϵ_r = 10.0, and μ_r = 1.0.
Ferrite Cover Layer: thickness = 3.0 mm, ϵ_r = 12.6, M_s= 2,500 G.

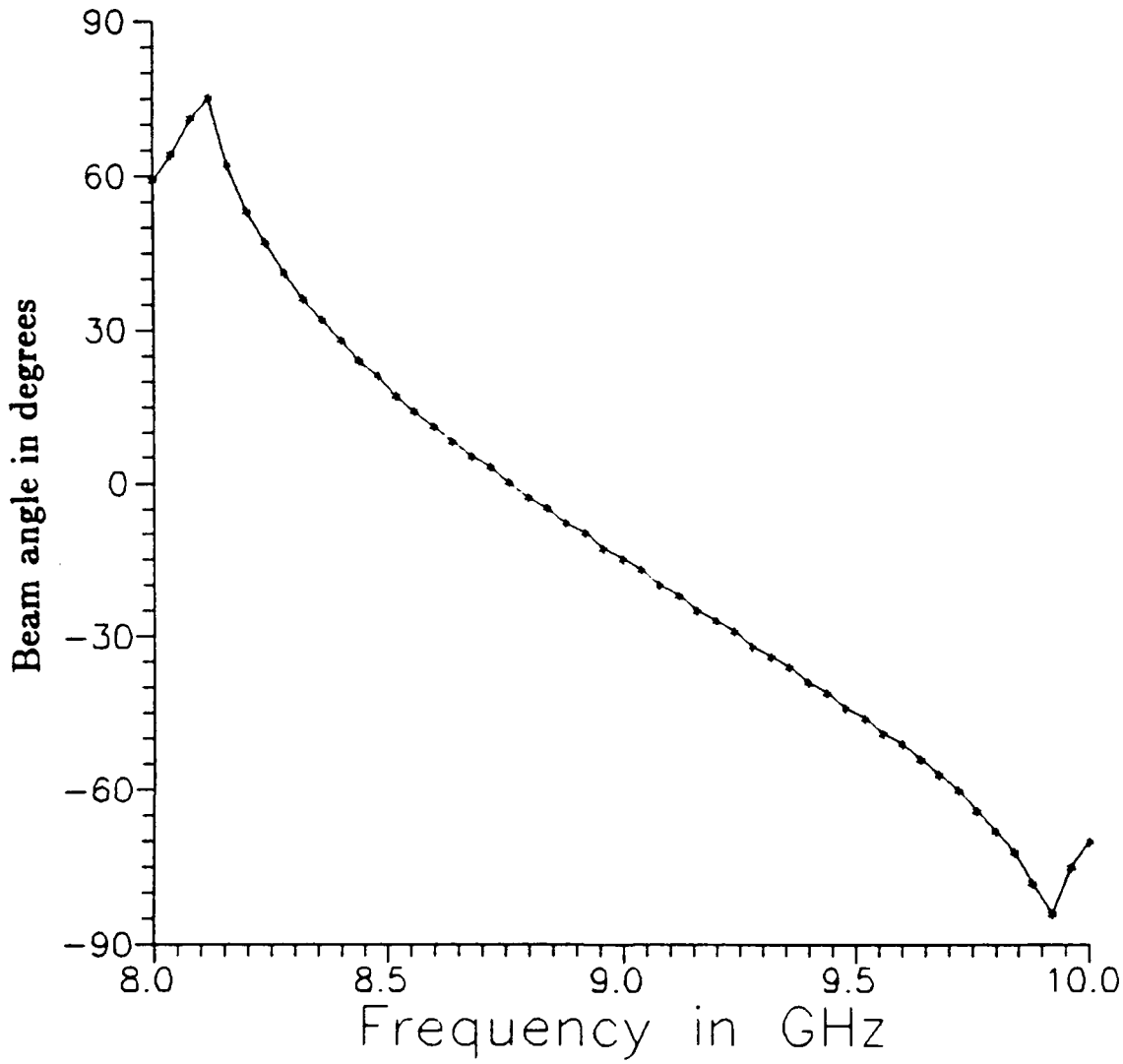

Figure 2.8: H-plane element beam pointing angle as a function of frequency.

The bias field strength is H_{dc}= 1000 G. The bias field is parallel to the dipole.
Substrate: thickness = 1.0 mm, ϵ_r = 10.0, and μ_r = 1.0.
Ferrite Cover Layer: thickness = 3.0 mm, ϵ_r = 12.6, M_s= 2500 G.

Chapter 3

Scattering and RCS of Microstrip Dipoles on/in Biased Ferrite Substrates

In many applications the antenna scattering or radar cross section (RCS) is of importance. In low observable applications it can become the most important performance parameter. Designs with simultaneous low in-band RCS and high gain and efficiency may be required. Conventional antenna designs are limited in the extent to which the EM scattering can be reduced by their reciprocal characteristics. Since because of the system reciprocity, a reduction in antenna in-band RCS implies a reduction in antenna gain. However, the use of non-reciprocal materials, such as biased ferrites, may provide substantial RCS reduction while the antenna gain is preserved.

The antenna scattering problem is of interest for a second reason: it provides the means by which the receive function of the antenna (the receive cross section) can be characterized. In non-reciprocal systems the transmit and receive patterns are distinct, and must be analyzed separately. The characterization of the receive antenna involves the solution of the problem of scattering from a loaded antenna. Specifically, it requires one to find the induced currents on the loaded antenna when a plane wave is incident on the structure, which is the essence of the scattering problem.

In this chapter the analyses and methods described in the previous chapters are applied to the scattering problem. The computation of RCS for the microstrip antenna on a layered structure including gyrotropic layers is outlined.

3.1 The Integral Equation for Scattering

The integral equation for the problem is

$$E_x^{inc} + \int G_{xx}\, J_x\, ds = 0, \text{ at the strip dipole,} \tag{3.1}$$

where the microstrip dipole is oriented in the $\hat{x}$ direction and is assumed only with current flowing in the $\hat{x}$ direction. The integral in Eq. 3.1 is a surface integral over the strip dipole. G_{xx} is the Green's function component which is the E_x component due to a δ current source in the x direction. The spectral component of this Green's function has been derived in the previous chapters. E_x^{inc} is the x component of the total electric field which results when a plane wave is incident on the layered structure without the strip dipole. This term thus includes reflected or scattered plane waves.

3.2 The Moment Method Solution for the Induced Dipole Currents

In the moment method procedure, the current is expanded in terms of a set of known basis functions. For the problem considered the current on the dipole of length $L = (N+1)a$ and width w is assumed to have the form

$$J_x(x,\, y) = \sum_{n=1}^{N} I_n\, j_n(x,\, y) \tag{3.2}$$

where

$$j_n(x,\, y) = \frac{f_n(x)}{\pi\sqrt{(w/2)^2 - y^2}}, \tag{3.3}$$

and

$$f_n(x) = \begin{cases} 1 - \frac{1}{a}|x - na| & , |x - na| \leq a \\ 0 & , \text{otherwise.} \end{cases} \tag{3.4}$$

In Galerkin's procedure the testing functions are chosen to be the same as the expansion functions. The integral equation (Eq. 3.1) is converted into a matrix equation:

$$\sum_{n=1}^{N} I_n\, Z_{mn} = V_m\,, \quad m = 1,\, 2,\, 3 \ldots N, \tag{3.5}$$

where

$$Z_{mn} = \int_{-w/2}^{w/2} \int_{-w/2}^{w/2} \int_{-L/2}^{L/2} \int_{-L/2}^{L/2} G_{xx}(x,\, x',\, y,\, y')\, j_n(x',\, y')\, j_m(x,\, y)\, dx\, dx'\, dy\, dy' \tag{3.6}$$

and

$$V_m = \int_{-w/2}^{w/2} \int_{-L/2}^{L/2} E_z^{inc}(x, y) j_m(x, y)\, dx\, dy. \tag{3.7}$$

The Green's function and its spectral component is related through the formula:

$$G_{zz}(x, x', y, y') = \frac{1}{4\pi^2} \int_{-\infty}^{\infty} \int_{-\infty}^{\infty} \tilde{G_{zz}}(k_x, k_y)\, e^{-jk_x(x-x')}\, e^{-jk_y(y-y')}\, dk_x\, dk_y \tag{3.8}$$

After inserting Eq. 3.8 into Eq. 3.6 and changing the order of integration, the impedance matrix element Z_{mn} in Eq. 3.6 may be written as

$$Z_{mn} = \int_{-\infty}^{\infty} \int_{-\infty}^{\infty} \tilde{G_{zz}}(k_x, k_y) \frac{\sin^4(ak_x/2)}{k_x^4} J_0^2(k_y w/2)\, e^{-jk_x(n-m)a}\, dk_x\, dk_y. \tag{3.9}$$

3.3 Scattered Far Fields and Radar Cross Section

Once the current on the dipole and the Green's function are known, it is possible to find the corresponding electromagnetic fields in the far zone.

The tangential electric fields at the air-material interface (z=d) can be written as

$$\vec{E}(x, y, z = d) = \frac{1}{4\pi^2} \int_{-\infty}^{\infty} \int_{-\infty}^{\infty} \tilde{E}(k_x, k_y) e^{-jk_x x - jk_y y}\, dk_x\, dk_y, \tag{3.10}$$

where

$$\tilde{E}(k_x, k_y) = \tilde{E}_x(k_x, k_y)\hat{x} + \tilde{E}_y(k_x, k_y)\hat{y}. \tag{3.11}$$

$\tilde{E}(k_x, k_y)$, a vector quantity, is the multiplication of the spectral dyadic Green's function and the Fourier transform of the current in the dipole. The far zone electric fields are related to the tangential spectral electric fields through the formulae [5]

$$E_\phi = jk_0 \frac{e^{-jk_0 R}}{2\pi R} \left[\tilde{E}_y(k_x, k_y)\cos\phi - \tilde{E}_x(k_x, k_y)\sin\phi\right], \tag{3.12}$$

$$E_\theta = jk_0 \frac{e^{-jk_0 R}}{2\pi R} \left[\tilde{E}_x(k_x, k_y)\cos\phi + \tilde{E}_y(k_x, k_y)\sin\phi\right], \tag{3.13}$$

where

$$k_x = k_0 \sin\theta \cos\phi \tag{3.14}$$

and

$$k_y = k_0 \sin\theta \sin\phi \tag{3.15}$$

The power density in space due to the current in the dipole is given as

$$P_o = \frac{1}{240\pi} \left[| E_\theta |^2 + | E_\phi |^2 \right], \tag{3.16}$$

while the power density of the incident plane wave is $1/(240\pi)$. Therefore, the radar cross section (RCS) in square meters is

$$\mathrm{RCS}(\theta,\ \phi) = 4\pi \left[|\ E_\theta\ |^2\ +\ |\ E_\phi\ |^2 \right], \tag{3.17}$$

and in dBsm,

$$\mathrm{RCS}_{\mathrm{dB}} = 10 \log_{10} \mathrm{RCS}(\theta,\ \phi). \tag{3.18}$$

3.4 Results

As was noted previously, the objective in RCS reduction schemes is to reduce the RCS but at the same time preserve the antenna RF performance, in particular to preserve transmit gain and/or receive cross section.

From the data that follows one can conclude that with biased ferrite cover layers it may be possible to reduce RCS and at the very least preserve transmit gain. (The interplay of RCS reduction, transmit gain, and receive cross section has yet to be fully investigated.)

The developed solution is based on a fullwave method that takes complete account of the surface wave phenomena due to the substrate construction. Consequently, in the results that follow the computed antenna gains include the surface wave efficiency factors.

Figure 3.1 consists of plots of the computed RCS, at broadside, for a microstrip dipole on an isotropic substrate with and without a biased ferrite cover layer. For each of the two cases the dipole was terminated with an appropriate matched load at 15 GHz. The isotropic substrate was 0.72 mm thick, with a permittivity of 2.2. The ferrite cover layer was 1.08 mm thick, with an assumed permittivity of 12.6, and a saturation magnetization (M_s) of 2780 Gauss. The bias field was 2500 Gauss and it was in a direction normal to the layer surface. The dashed curve, which corresponds to the case with the biased ferrite cover, shows a reduction of the peak RCS of about 7 dBsm relative to the uncovered isotropic case.

The reduction in RCS is significant only if it is possible to simultaneously maintain the gain of the antenna. This is in fact the case. Figure 3.2 consists of plots of the computed transmit gains for the structures with and without the biased ferrite cover. It is seen that at 15 GHz the gain of the antenna with the biased ferrite cover only dropped by 1.0 dB compared to the uncovered isotropic case. The biased ferrite cover layer reduced the peak antenna RCS by 7 dBsm while only reducing the transmit gain by less than 1.0 dB. In some applications that would be an excellent trade-off.

In Figure 3.3 the computed broadside RCS is plotted for the full range of incident field polarizations. This is for the same parameters as those of Figure 3.1, at 15 GHz. From this it is clear that the reduction in RCS is not just due to a rotation of the incident field relative to the polarization of the dipole. The worst-case (largest) RCS for the antenna with a biased ferrite cover is lower by 6dBsm than the worst-case RCS of the isotropic antenna.

Figures 3.4 and 3.5 are, respectively, plots of the current at the load and the received power as a function of the incident field polarization. Those are, as in the previous cases, for broaside incidence at 15 GHz.

The curves of Figures 3.6 and 3.7 are of antenna RCS over frequency and for several different incident field polarizations. The corresponding induced dipole currents are plotted in Figures 3.8 and 3.9.

Computations were made for several discrete angles of incidence other than broadside. The data of Table 3.1 indicates that the RCS reduction noted in the previous data is not specific to the broadside incidence condition, but rather that the phenomenon is observed at all angles of incidence.

Transmit gain and receive gain patterns are provided in Figures 3.10 and 3.11, respectively. The sum of the data suggests that the reduction in RCS is obtained at the expense of the receive gain (receive-cross-section) of the antenna. This at least is the case for the construction and parameters which were used here. It may be possible to find a set of parameters for which the receive gain is preserved and instead the transmit gain is sacrificed in order to achieve the reduction of antenna RCS.

3.5 Conclusion

The scattering and RCS for microstrip antennas on gyrotropic substrates has been investigated. A comparison of gain and RCS data for microstrip antennas with biased ferrite cover layers indicates that it is possible to reduce broadside RCS while preserving transmit gain. These are preliminary results and a variety of parametric studies remain to be carried out. The interplay of RCS, transmit gain, and receive cross section must be fully explored.

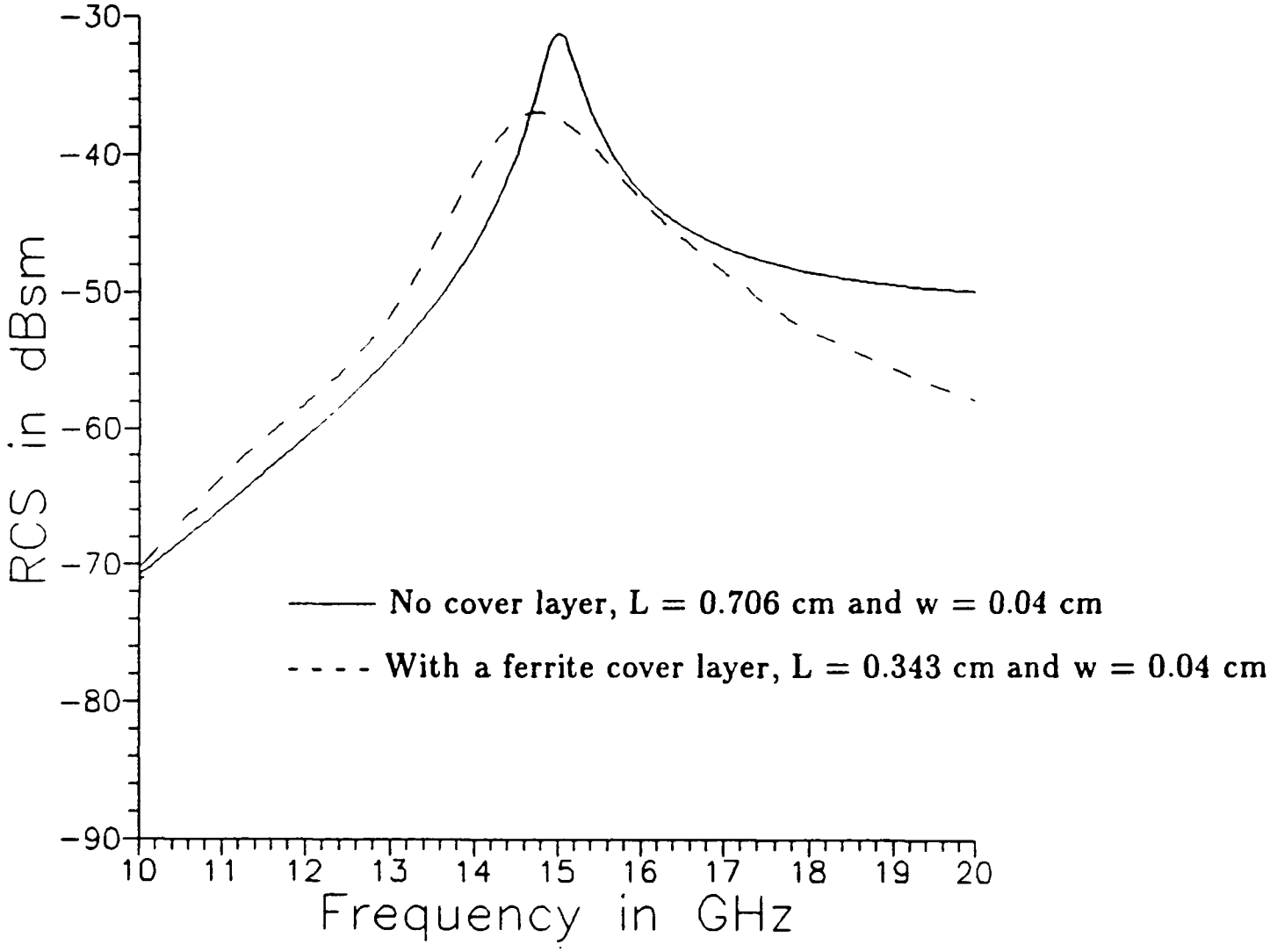

Figure 3.1: RCS at Broadside as a Function of Frequency With and Without a Biased Ferrite Cover Layer.

Substrate: thickness = 0.72 mm, and ϵ_r = 2.2.
Ferrite Cover Layer: thickness= 1.08 mm, ϵ_r = 12.6,
Saturation magnetization (M_s) = 2780 G,
H_{dc} = 2500 Gauss, and the bias field is normal to the layers and dipole.
In each case the dipole is terminated with a matched load at 15 GHz.

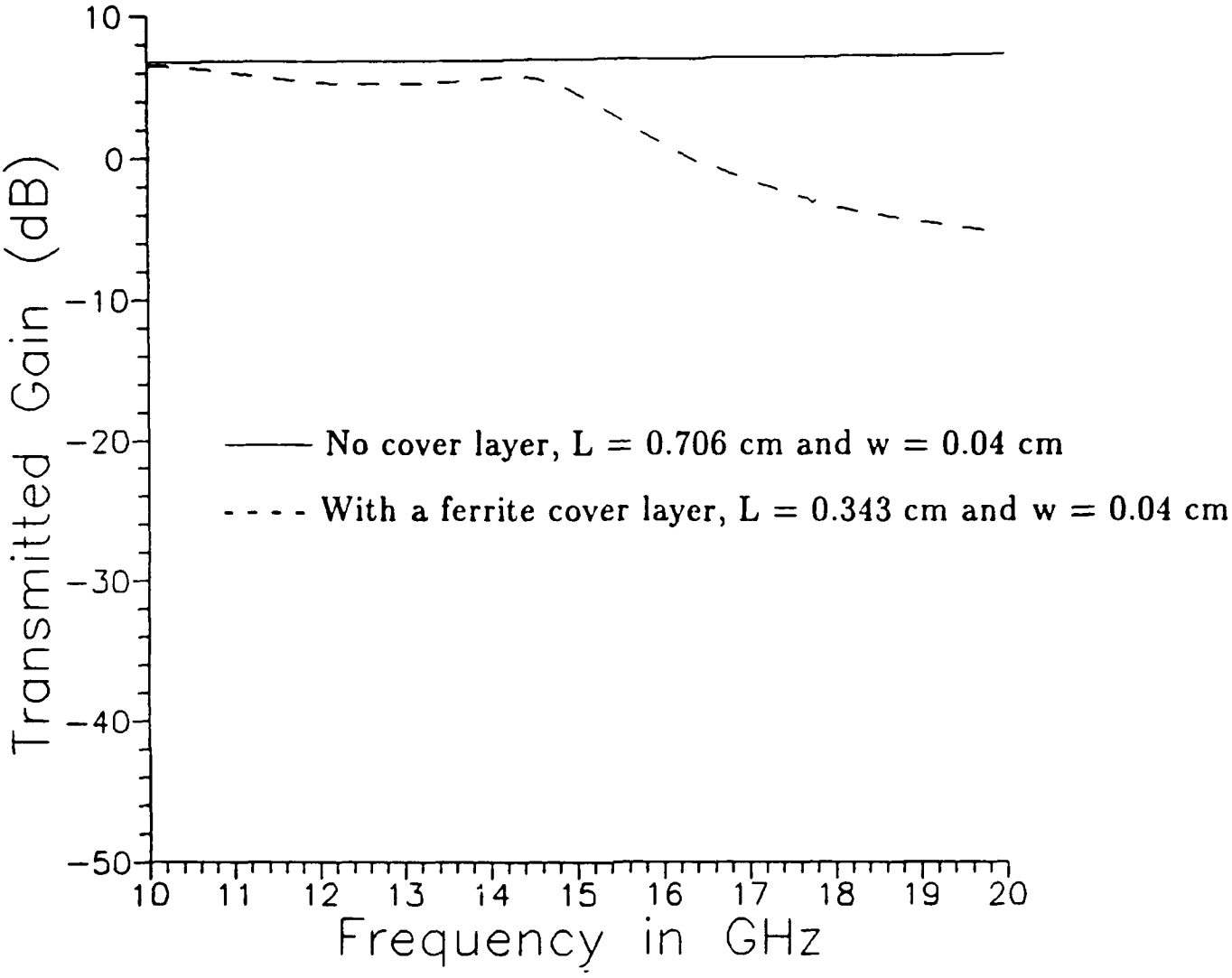

Figure 3.2: Transmit Gain at Broadside as a Function of Frequency for a Microstrip Dipole With and Without a Biased Ferrite Cover Layer.

Substrate: thickness = 0.72 mm, and ϵ_r = 2.2.
Ferrite Cover Layer: thickness= 1.08 mm, ϵ_r = 12.6,
Saturation magnetization (M_s) = 2780 G,
H_{dc} = 2500 Gauss, and the bias field is normal to the layers.

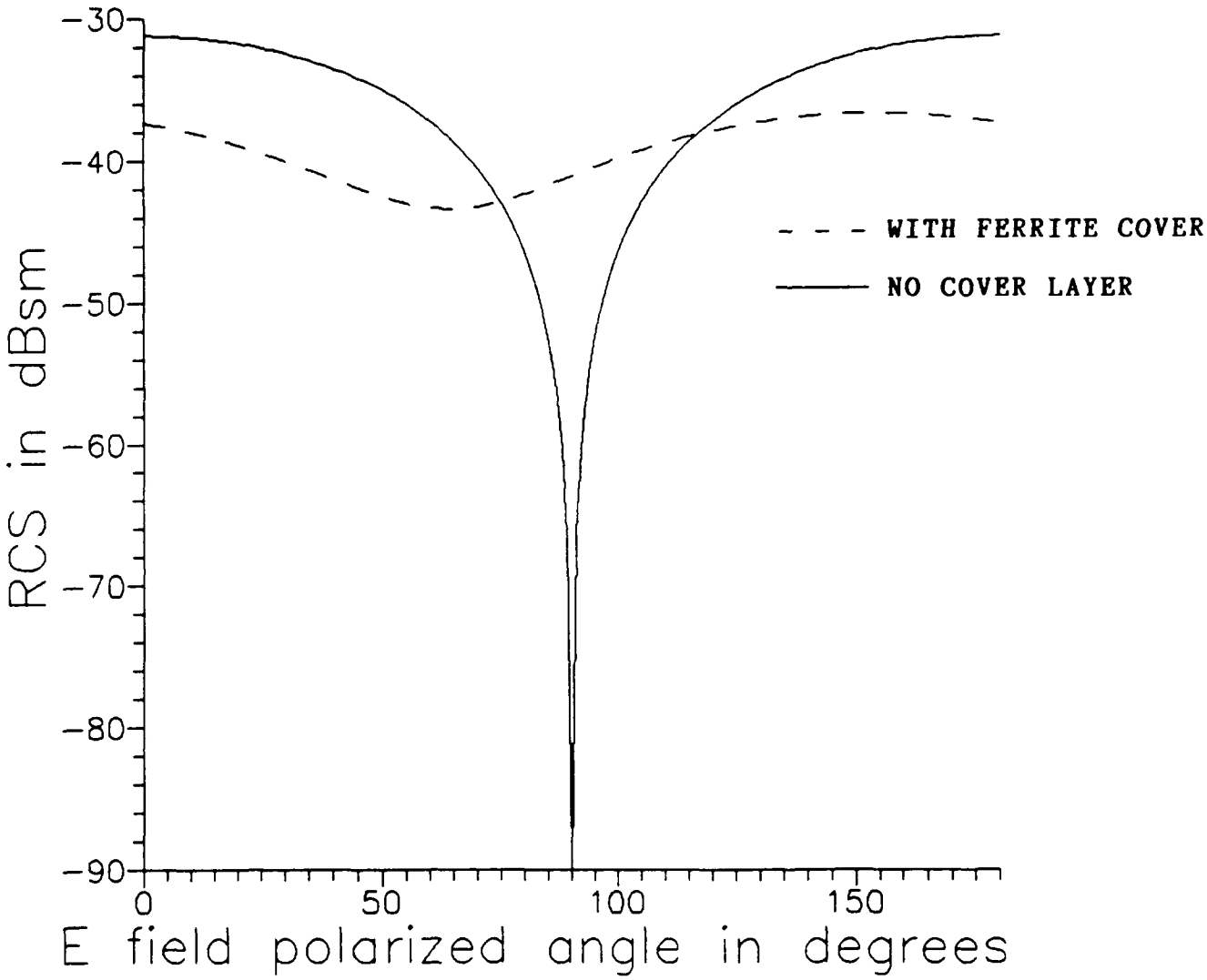

Figure 3.3: RCS at Broadside as a Function of Incident Field Polarization: With and Without a Biased Ferrite Cover Layer.

Frequency= 15 GHz
Substrate: thickness = 0.72 mm, and $\epsilon_r = 2.2$.
Ferrite Cover Layer: thickness= 1.08 mm, $\epsilon_r = 12.6$,
Saturation magnetization (M_s) = 2780 G,
H_{dc} = 2500 Gauss,
The bias field is vertical (normal to substrate),
The dipoles are terminated with matched loads:
$Z_{in}^{fer} = 13.0\Omega$, and $Z_{in}^{iso} = 2.80\Omega$.

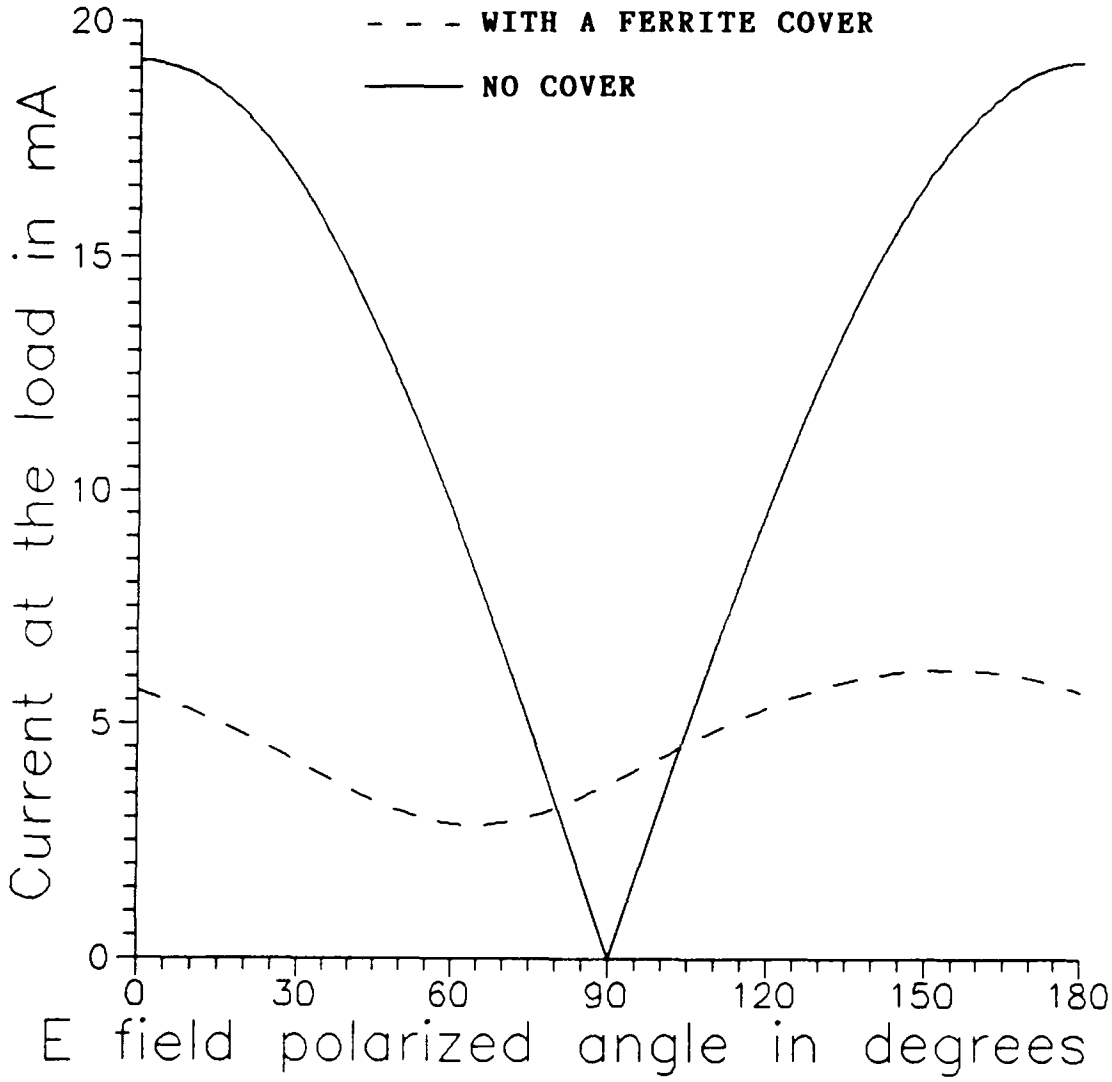

Figure 3.4: Current at the Load as a Function of the Incident Field Polarization, for a Broadside Incident Field: With and Without a Biased Ferrite Cover Layer.

Frequency= 15 GHz
Substrate: thickness = 0.72 mm, and $\epsilon_r = 2.2$.
Ferrite Cover Layer: thickness= 1.08 mm, $\epsilon_r = 12.6$,
Saturation magnetization (M_s) = 2780 G,
H_{dc} = 2500 Gauss,
The bias field is vertical (normal to substrate),
The dipoles are terminated with matched loads:
$Z_{in}^{fer} = 13.0\Omega$, and $Z_{in}^{iso} = 2.80\Omega$.

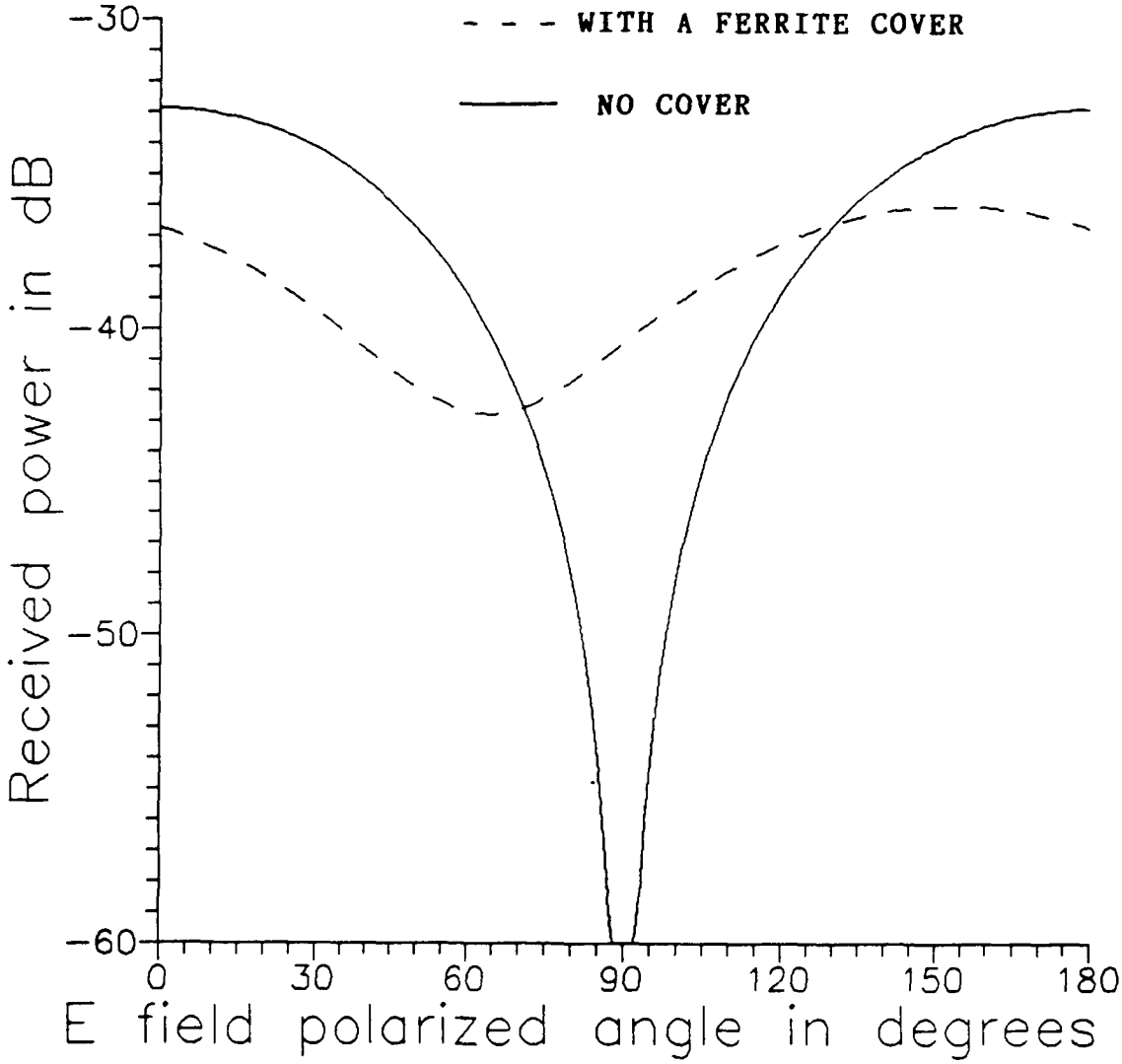

Figure 3.5: Received Power as a Function of the Incident Field Polarization, for a Broadside Incident Field: With and Without a Biased Ferrite Cover Layer.

Frequency= 15 GHz
Substrate: thickness = 0.72 mm, and $\epsilon_r = 2.2$.
Ferrite Cover Layer: thickness= 1.08 mm, $\epsilon_r = 12.6$,
Saturation magnetization (M_s) = 2780 G,
H_{dc} = 2500 Gauss,
The bias field is vertical (normal to substrate),
The dipoles are terminated with matched loads:
$Z_{in}^{fer} = 13.0\Omega$, and $Z_{in}^{iso} = 2.80\Omega$.

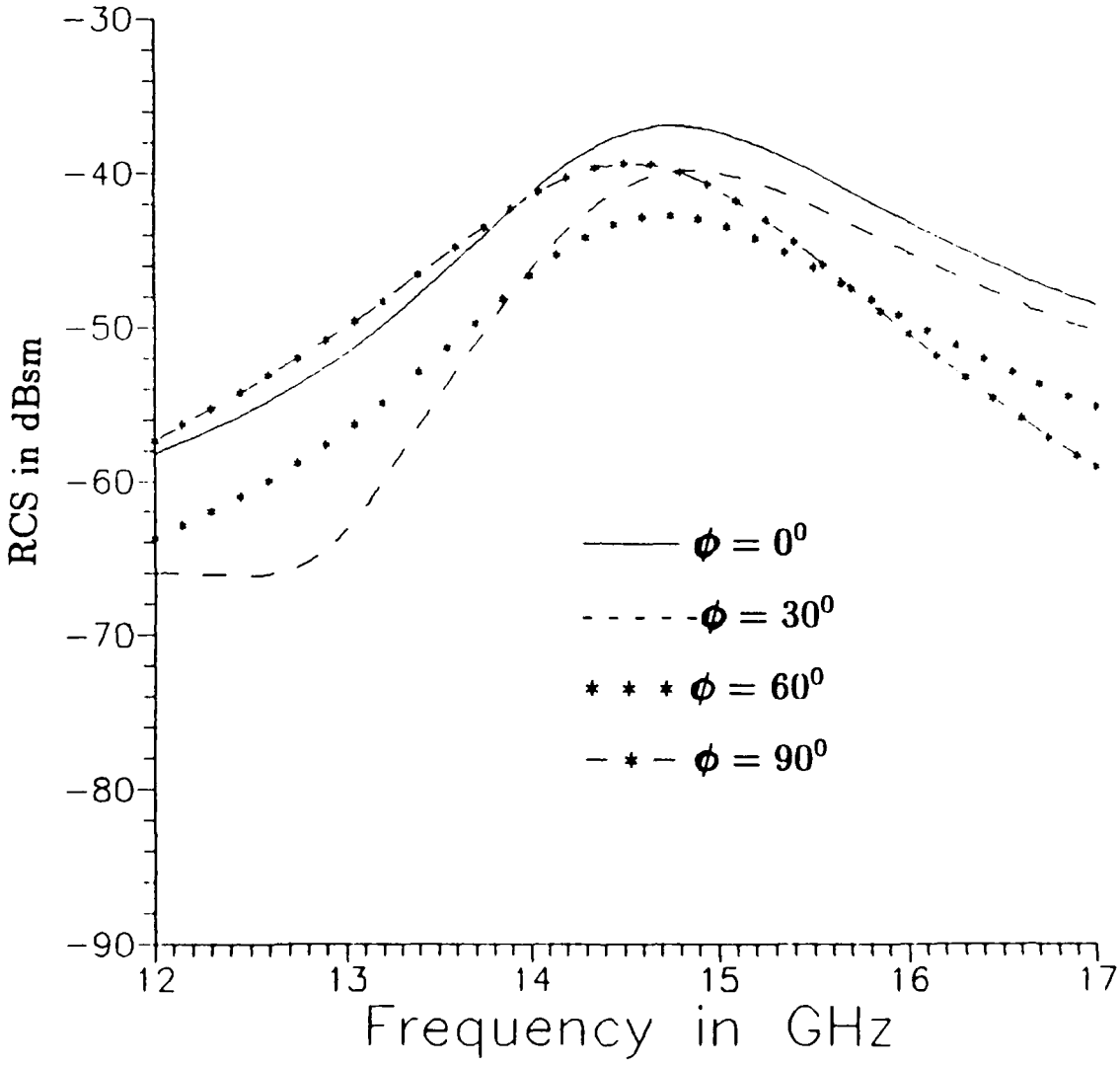

Figure 3.6: Broadside RCS as a Function of Frequency for Different Incident Field Polarizations. The angle ϕ identifies the electric field direction in the x-y plane.

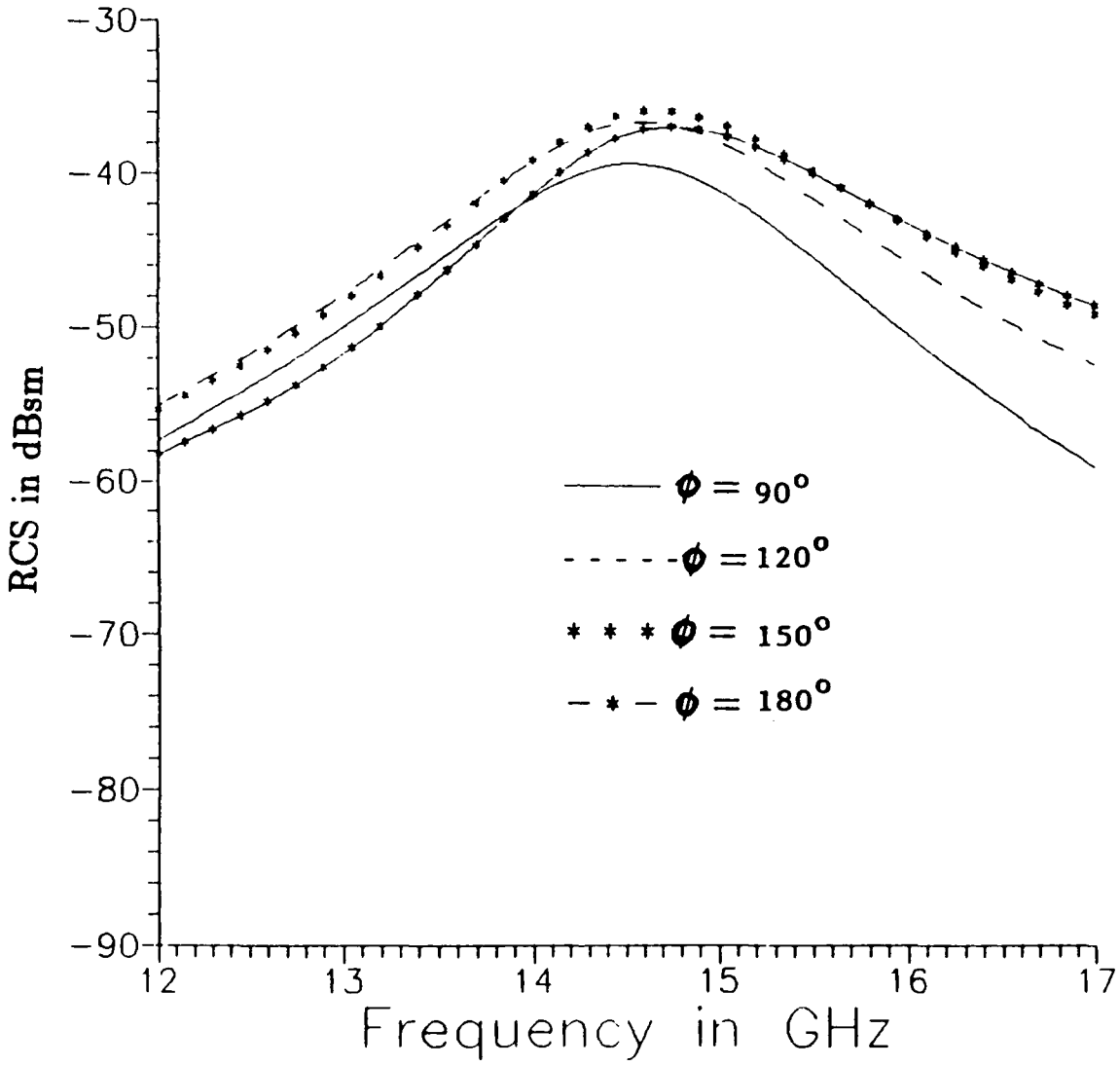

Figure 3.7: Broadside RCS as a Function of Frequency for Different Incident Field Polarizations. The angle ϕ identifies the electric field direction in the x-y plane.

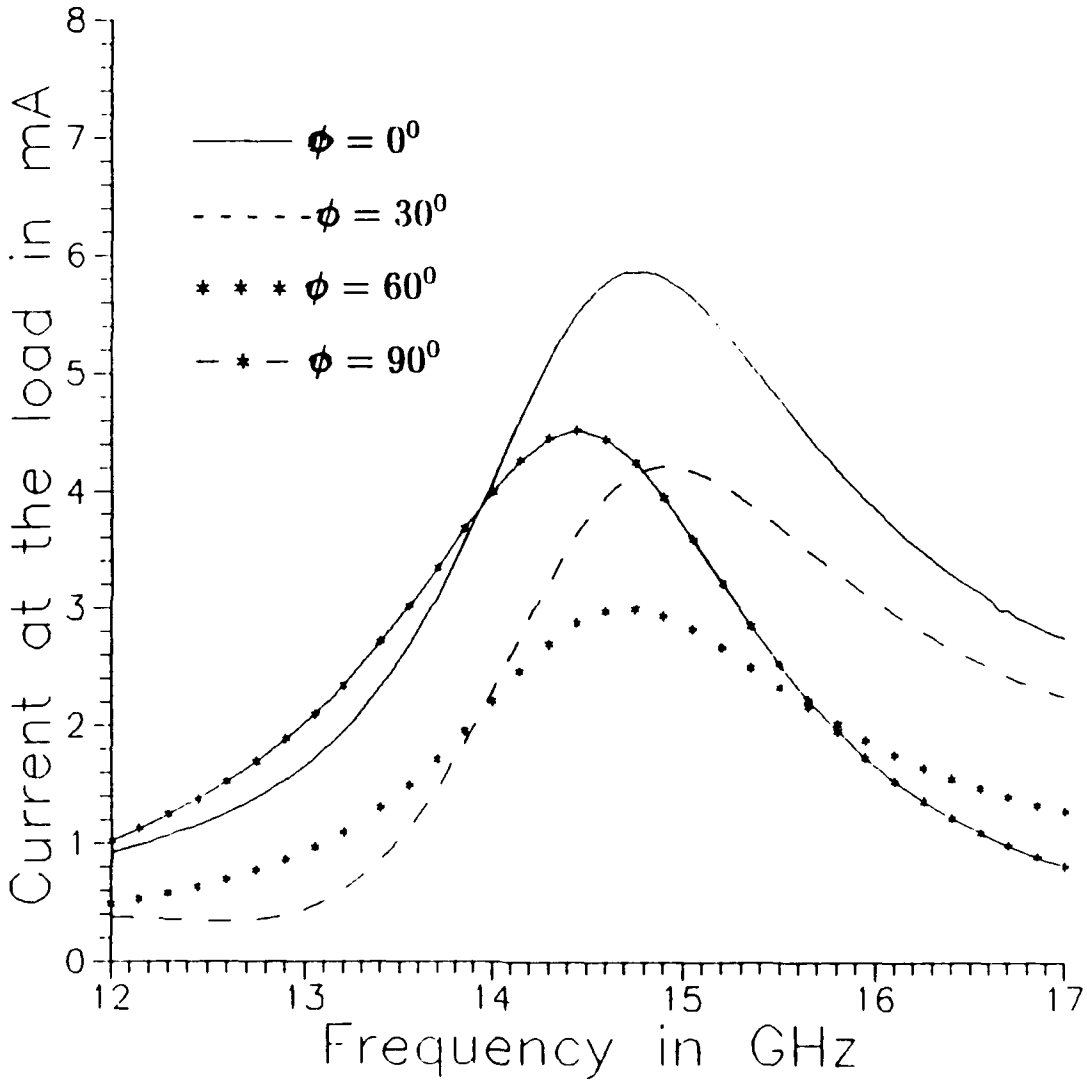

Figure 3.8: Induced Current as a Function of Frequency for Different Incident Field Polarizations. The angle ϕ identifies the electric field direction in the x-y plane.

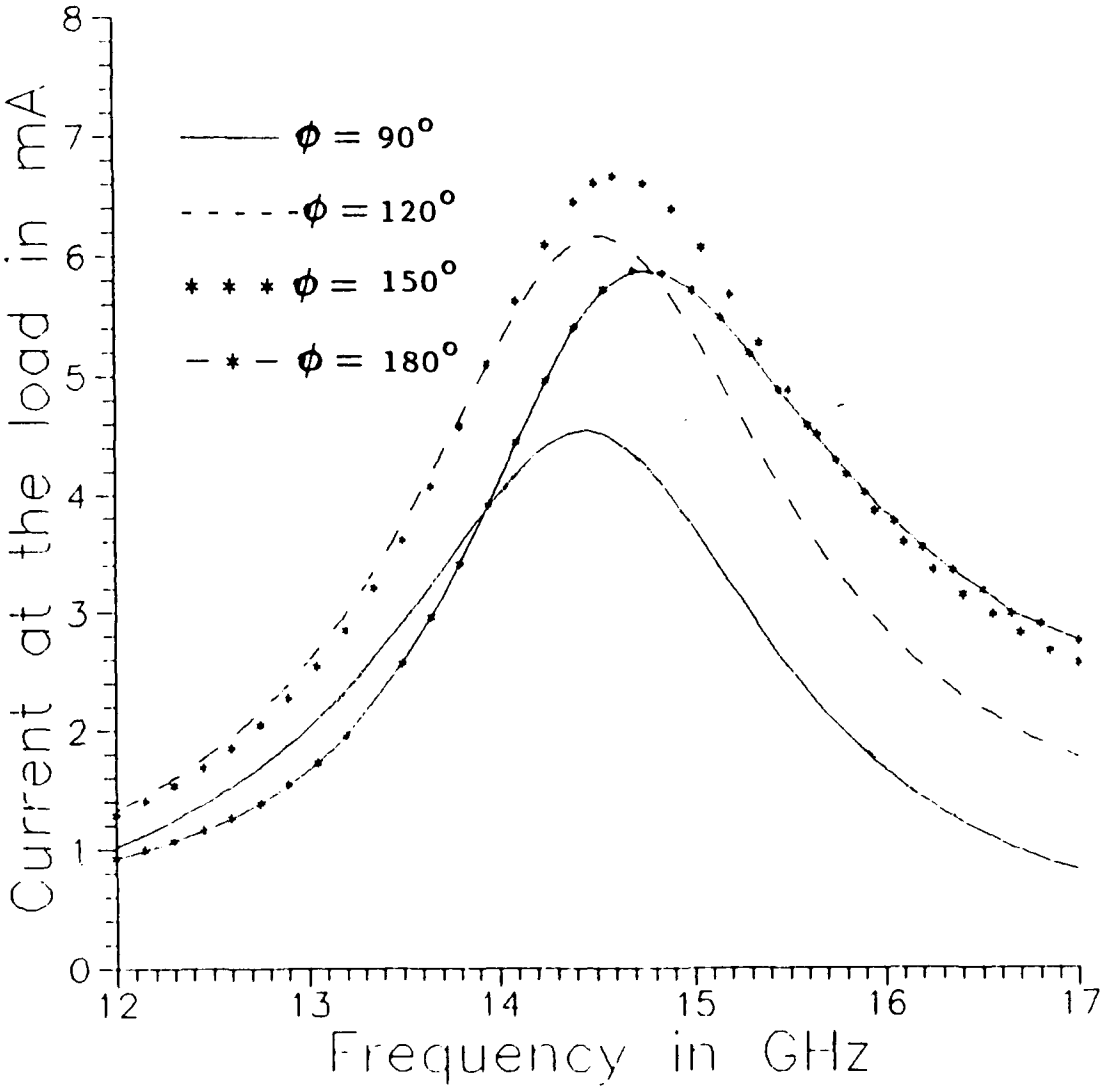

Figure 3.9: Induced Current as a Function of Frequency for Different Incident Field Polarizations. The angle ϕ identifies the electric field direction in the x-y plane.

Incident Angle	Dielectric	Ferrite/Dielectric
$\theta = 30^0$, $\phi = 90^0$	-33.6	-39.3
$\theta = 60^0$, $\phi = 90^0$	-43.1	-44.8
$\theta = 30^0$, $\phi = 0^0$	< -90	-43.8
$\theta = 60^0$, $\phi = 0^0$	< -90	-58.9

TE MODE INCIDENT

Incident Angle	Dielectric	Ferrite/Dielectric
$\theta = 30^0$, $\phi = 90^0$	< -90	-40.4
$\theta = 60^0$, $\phi = 90^0$	< -90	-43.1
$\theta = 30^0$, $\phi = 0^0$	-33.9	-40.1
$\theta = 60^0$, $\phi = 0^0$	-40.6	-54.6

TM MODE INCIDENT

Table 3.1: RCS for Off-broaside Angles of Incidence and TE and TM Incident Field Polarizations.

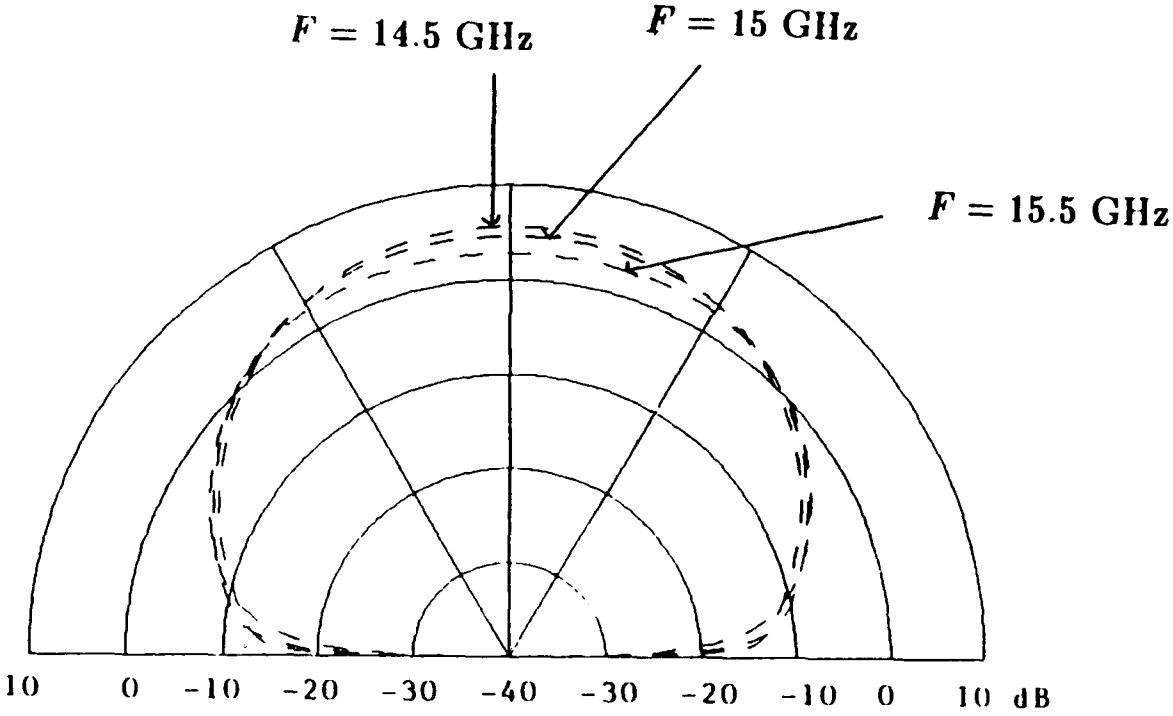

Figure 3.10: Transmit Gain Patterns: $\phi = 0°$ plane.

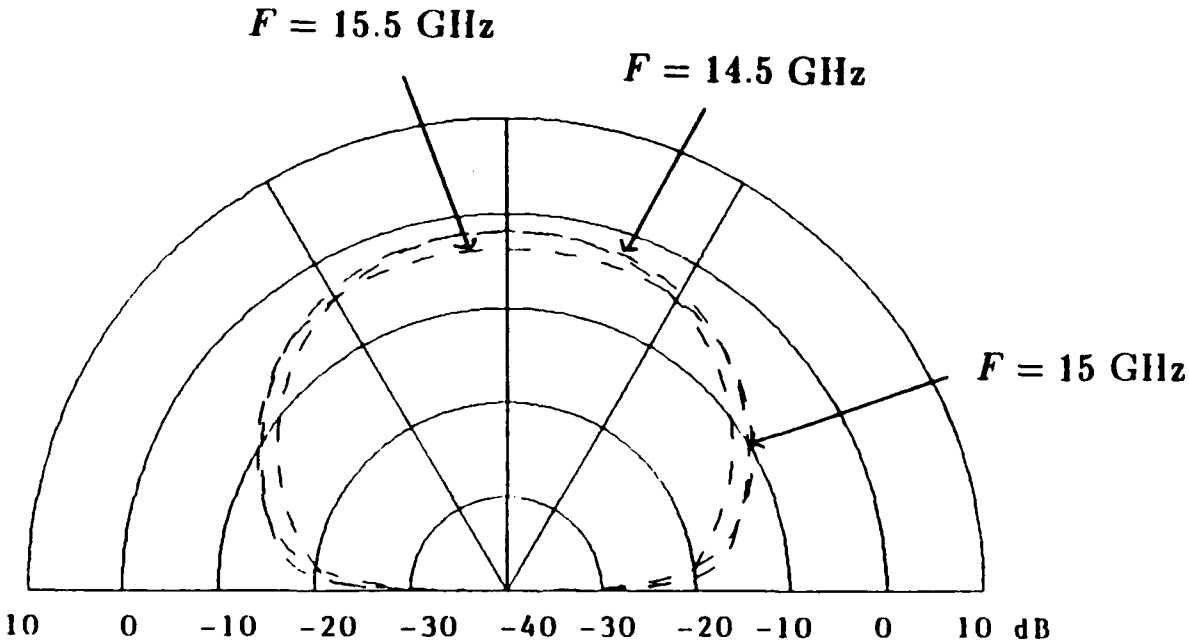

Figure 3.11: $\phi = 0°$ plane Receive Patterns for the case of an Incident TM mode.

Chapter 4

Evaluation of Spectral Integrals in the Moment Method

A numerical algorithm for the moment method solution of printed circuit antenna problems is developed. The formulation employs a spectral domain approach; however, the integration variables are in the cartesian instead of the polar coordinate system. This numerical scheme separates the integration involving the longitudinal and the transverse dependence of the basis functions. This aspect may reduce the computation effort drastically. The new approach is found very efficient and easy to use, and is suitable for a variety of basis functions including mixed type basis function sets.

4.1 Introduction

Method of moments solutions of integral equations have been applied extensively to printed circuit antenna problems in the past. In this approach, an exact Green's function for a grounded dielectric substrate is used. The method of moments transforms the integral equation into linear simultaneous equations where the solution (current on the microstrip) can be found by matrix inversion. The efficiency and accuracy of the solution depends on the computation of each individual matrix element as well as the matrix inversion. Depending on the method of formulation, the computational methods thus lead to two different branches. If the formulation is in a real space, the computation involves the evaluation of a Sommerfeld-type integral [11,1,12,13]. Numerical techniques for efficient computation of this type of integral are developed in [14,15,16]. These numerical methods have a common feature in that, if a true Galerkin procedure is used, then the computations of a

Sommerfeld type integral (Green's function) and four finite integrals (two surface integrals over the planar conductor) are required. An efficient approach as was described in [14] is to tabulate the Green's function as a function of the distance between the source and field point such that the infinite integral needs to be computed only once. The four finite integrals can usually be reduced two integral if the expansion and testing functions are properly chosen. For irregular shaped or entire domain basis functions, more analytic derivation may be required to reduced the computation effort of the four integrals.

If the formulation of the problem is in a plane wave spectral domain, the computation always involves a double infinite integration which is usually transformed into a finite and an infinite one by a transformation from a cartesian to a polar coordinate system as described in [17]-[23]. The problem with this computation is that the finite integration involves an oscillatory function, while the infinite one is slowly convergent and may be highly oscillatory when the basis function spacing is large. These aspects lead to a numerical computation which is very inefficient. An improved technique using an equivalent image extraction method has been proposed [24]. Although it enhances the computational efficiency, it is only developed for piecewise sinusoidal basis functions with no transverse variation and still has difficulties for the thin substrate cases.

In this communication, a new algorithm for the matrix element computation in the method of moments formulation is presented. In the new approach, the integration is carried out directly in a plane wave spectral domain, which involves a double infinite integration. The advantages of computing the double infinite integration directly rather than treating a finite and an infinite one will be discussed. The comparison of the new and the previous methods, in terms of computational efficiency, is also made through the examples of a center-fed dipole and a microstrip open-end discontinuity on an isotropic substrate.

4.2 The New Algorithm

If developed in a spectral domain [17]-[24], the impedance matrix elements, from the method of moments formulation of the printed circuit structure shown in Figure 4.1, are in the form of

$$Z = \int_{-\infty}^{\infty}\int_{-\infty}^{\infty} G(\lambda_x, \lambda_y) J_a(\lambda_x) J_b(\lambda_y) e^{j\lambda_x x_m + j\lambda_y y_n} d\lambda_x d\lambda_y, \tag{4.1}$$

where (x_m, y_n) is the center-to center displacement between the expansion and testing functions. The Green's function $G(\lambda_x, \lambda_y)$ includes the information of the geometry and material constants. If a single layer microstrip structure is used as

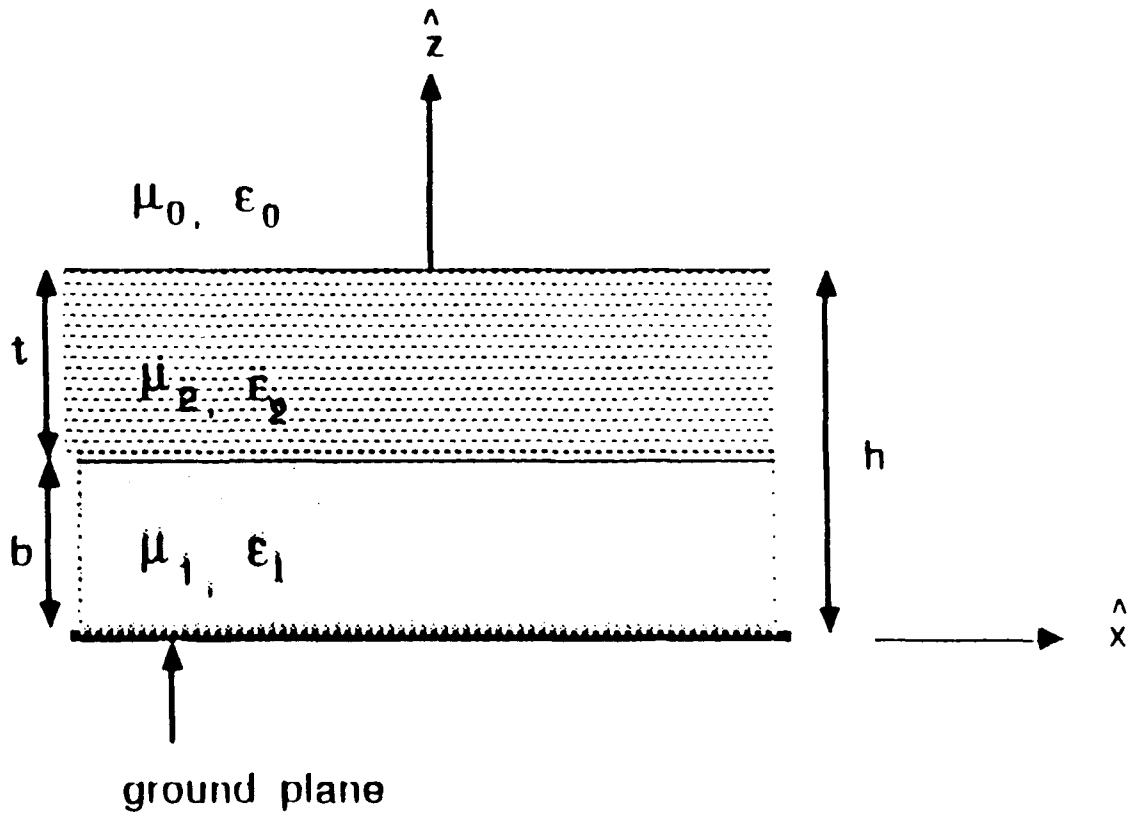

Figure 4.1: A Two-layer Printed Antenna Structure

an example, the Green's function may be any of the following three components, depending on which current and electric field components are considered [25].

$$G_{zz}(\lambda_x, \lambda_y) = [\frac{\epsilon_r - \lambda_x^2}{D_e(\lambda)} + \frac{\lambda_x^2 q_1(1-\epsilon_r)}{D_e(\lambda)D_m(\lambda)}], \tag{4.2}$$

$$G_{xy} = [\frac{-\lambda_x\lambda_y}{D_e(\lambda)} + \frac{\lambda_y\lambda_x q_1(1-\epsilon_r)}{D_e(\lambda)D_m(\lambda)}], \tag{4.3}$$

$$G_{yy} = [\frac{\epsilon_r - \lambda_y^2}{D_e(\lambda)} + \frac{\lambda_y^2 q_1(1-\epsilon_r)}{D_e(\lambda)D_m(\lambda)}], \tag{4.4}$$

where

$$D_e(\lambda) = q + \frac{q_1}{\tanh(2\pi q_1 h)} \tag{4.5}$$

$$D_m(\lambda) = q_1 + \frac{q\epsilon_r}{\tanh(2\pi q_1 h)}, \tag{4.6}$$

$$q = \sqrt{\lambda^2 - 1}, \tag{4.7}$$

$$q_1 = \sqrt{\lambda^2 - \epsilon_r} \tag{4.8}$$

and

$$\lambda = \sqrt{\lambda_x^2 + \lambda_y^2}. \tag{4.9}$$

In this work, we use an approach, in which the integral in Eq. 4.1 is evaluated directly instead of transforming it into a polar coordinate system. With rearrangement, Eq. 4.1 can be written as

$$Z = \int_{-\infty}^{\infty} J_a(\lambda_x) e^{j\lambda_x x_m} S(\lambda_x) d\lambda_x \tag{4.10}$$

where

$$S(\lambda_x) = \int_{-\infty}^{\infty} G(\lambda_x, \lambda_y) J_b(\lambda_y) e^{j\lambda_y y_n} d\lambda_y. \tag{4.11}$$

Both the λ_x and λ_y integration ranges can usually be reduced to the semi-infinite ranges from 0 to ∞ depending on the even or odd symmetry of the integrand. The Green's functions contain singularities in the range $1 < \lambda < \sqrt{\epsilon_r}$ which correspond to either TM surface wave modes ($D_m(\lambda) = 0$) or TE surface wave modes ($D_e(\lambda) = 0$) [11]. A pole extraction method was used [11,1,19,20,21] in the past, which in addition to the numerical integration, requires the calculation of residues and Cauchy principal values at the singularity points. For a multilayer or anisotropic structure, the location of the singularities and the derivative of $D_e(\lambda)$ and $D_m(\lambda)$ usually introduces more complexity if not more difficulty into the problems. A nice way to avoid this singularity problem is to deform the integration in the range from 0 to $\sqrt{\epsilon_r}$ [22]. For the present approach, a careful study shows that both the λ_x and λ_y integration contour needs to be deformed

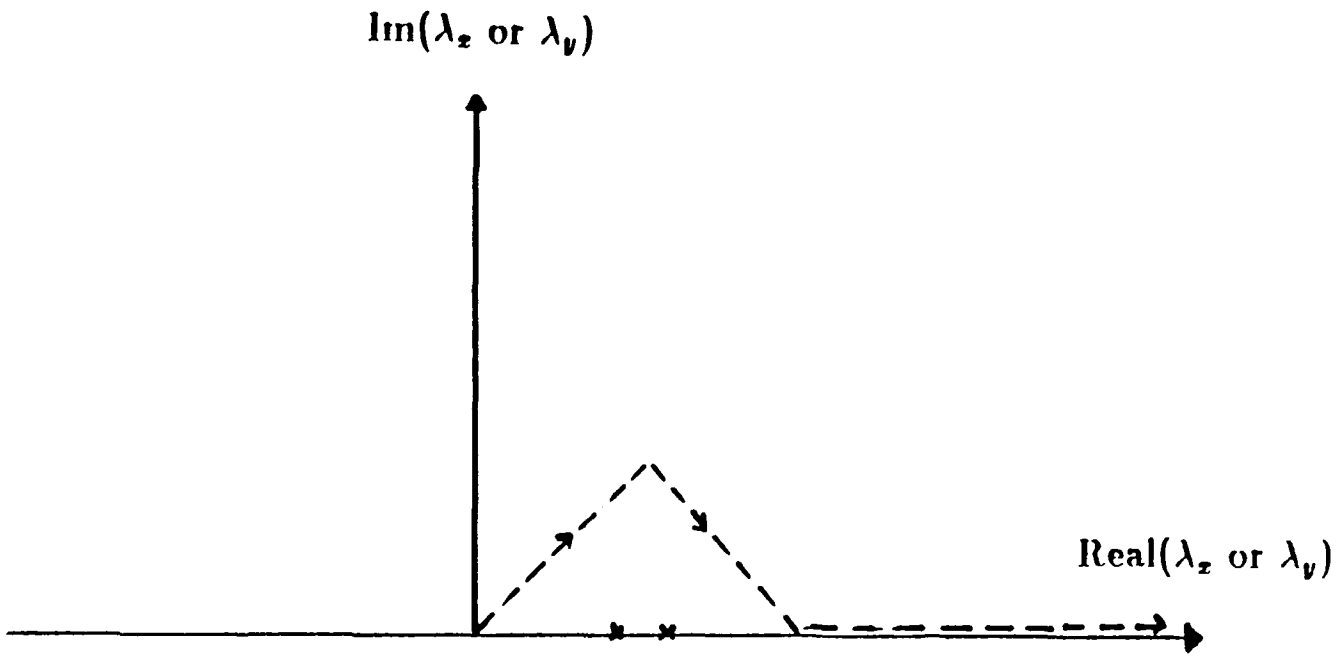

Figure 4.2: Integration Contour in either the λ_x or λ_y complex plane.

to avoid the singularities. The deformed integration path is shown in Figure 4.2. Although the deformed integration path can be arbitrary mathematically, care must be taken in choosing the proper path for numerical integration. When the path is off the real axis, the integrand increases exponentially; therefore if the contour is too far from the real axis, numerical instability occurs. Also if the path is too close to the real axis (the singularities), the integrand is not a smooth function. A numerical study for the integration path in Figure 4.2 shows that choosing the maximum of $\mathrm{Im}(\lambda_x)$ and $\mathrm{Im}(\lambda_y)$ to be about 1/(50h) (h is substrate thickness) is adequate.

For $\lambda_y \geq \sqrt{\epsilon_r}$, the function $S(\lambda_x)$ is an integral where the integrand is a smooth function unless y_n is large. Also, the integral is uniformly convergent. For a single layer microstrip structure with a roof-top basis function, when $\lambda \gg \frac{2}{\pi h}$, the Green's function approaches its asymptotic form which contains only algebraic functions and then integral can be evaluated either in a closed form or can be deformed to an integral with the integrand decaying exponentially. An example of this derivation is given in Appendix 4-A. If the basis functions are not simple trigonometric functions (for example, Maxwellian function, irregular shape basis functions) or the structure is multi-layered or anisotropic, there is no simple asymptotic form for the integrand in $S(\lambda_x)$. In these cases, a Filon's integration scheme [26] may be applied, where the integration path is divided into many interval and the non-sinusoidal term in the integrand is approximated parabolically in each interval. Once the parabolic function approximation is used, the integration in each divided interval can be evaluated in a closed form.

One distinct feature of the new algorithm is that the function $S(\lambda_x)$ is a smooth and monotonic function when $\lambda_x > \sqrt{\epsilon_r}$. From Eqs. 4.2- 4.9, it is seen that the Green's function is asymptotically linear with respect to λ_x. This implies that one can use only a few sampling points to tabulated the function $S(\lambda_x)$ and that interpolation can provide the value with excellent accuracy. A typical example of the functional behavior of $S(\lambda_x)$ is shown in Figure 4.3, where it is seen that, asymptotically, $S(\lambda_x)$ is almost a straight line. Once the function $S(\lambda_x)$ is tabulated, one can proceed to compute the impedance matrix elements shown in Eq. 4.10, which contain a smooth function multiplying either $\cos(\lambda_x x_m)$ or $\sin(\lambda_x x_m)$. This sinusoidal function may oscillate rapidly when x_m is large. To alleviate this difficulty, one can again approximate the smooth function with piecewise parabolic functions.

The approach proposed here has a feature that for fixed y_n the term $S(\lambda_x)$ needs to be computed and tabulated only once and is stored in an array. For example, for a rectangular patch with one dimensional current, which is divided into $M \times N$ subsections, using the new algorithm to generate the impedance matrix elements, it is required to compute a one dimensional infinite integration only M+NP times

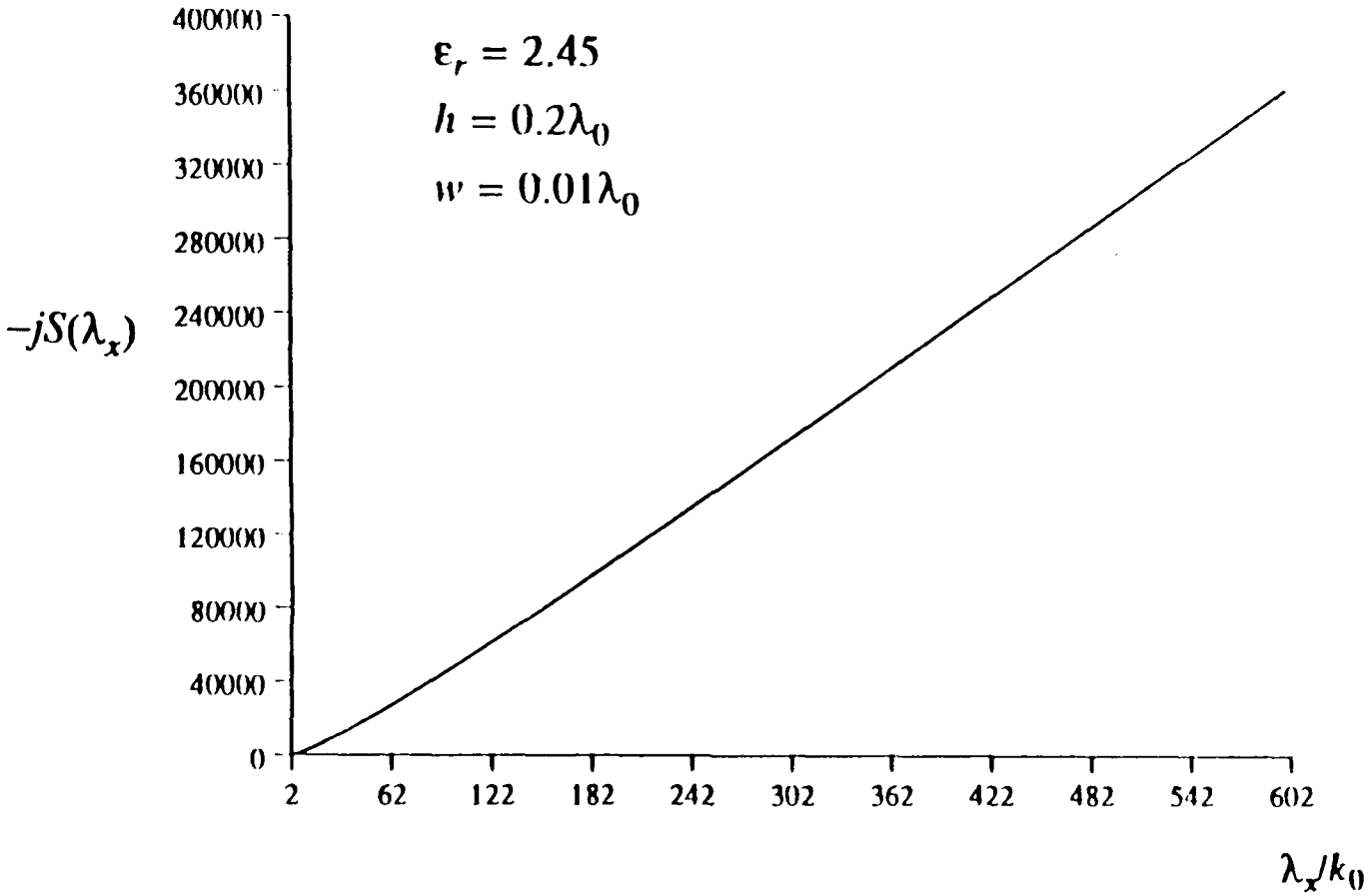

Figure 4.3: $-jS(\lambda_x)$ as a function of λ_x

where P is the number of sampling points for $S(\lambda_z)$. In contrast, if the integration is performed in the polar coordinate, it is required to compute a double integration $M \times N$ times. This feature enhances drastically the computational efficiency. It is also noted that the approach proposed in this communication may not require the use of the asymptotic form of the Green's function unless for some special cases. In other words, the efficiency of the numerical integration does not depend on how far the integration path goes for the integrand to approach its asymptotic form. Therefore, the algorithm is efficient over almost the entire frequency range.

4.3 Numerical Examples

4.3.1 A Center-fed Dipole

For a slender dipole with assumed transverse Maxwellian distribution, if 100 cells are used to represent the current longitudinal dependence and 50 points are used to tabulate the function $S(\lambda_z)$, then in order to fill in the impedance matrix the proposed algorithm (algorithm A) requires the computation of an infinite integral 150 times. In contrast, the algorithm with the integral in polar coordinate (algorithm B), typically requires the computation of the infinite integral more than 3000 times. If a combination of the piecewise sinusoidal and Maxwellian basis functions are used in a Galerkin procedure of the moment method, with algorithm A it takes only about 6 minutes on an IBM AT computer and about 35 seconds on a Compaq-386 computer to generate all the impedance matrix elements. With algorithm B it takes about one hour on an IBM AT and about 6 minutes and 30 seconds on a Compaq-386. The computer codes using algorithm B for testing are based on the one discussed in [23], which is about 2 times more efficient than that discussed in [20].

4.3.2 Microstrip Open-end and Gap Discontinuities

For the microstrip open-end problem, modeling of semi-infinite lines is required. A combination of semi-infinite traveling wave modes and local subdomain modes is fruitful and can be modified easily to apply to different geometries [21,23]. The efficiency of the present algorithm is clearly shown in these open-end and gap computations, where the mixed type of basis functions are used. This is because if only one transverse basis function is used for the longitudinal current, the function $S(\lambda_z)$ is the same for all the impedance matrix elements. Therefore, it needs to be computed only once. The computer time required to compute

the equivalent circuit of this semi-infinite microstrip line is tested for both the algorithm with a polar coordinate integration (algorithm B) and the one with a rectangular coordinate (algorithm A) integration. For a Compaq-386 computer, with 20 subdomain basis functions, algorithm A requires about 30 seconds, while algorithm B requires about 200 seconds, to compute one data point.

4.4 Conclusions

In this work, a new algorithm was developed for the method of moments solution of microstrip antenna and circuit problems. The algorithm is found very efficient and can be applied over almost the entire frequency range. The efficiency and versatility of the new algorithm are illustrated through the examples of a microstrip dipole and a microstrip open-end and gap. The new algorithm can also handle a variety of different types of basis functions, which will find many applications for the analysis of irregular shape microstrip antennas and circuit discontinuities.

Appendix 4-A

An example is presented that illustrates the integration contour deformation that is used to obtain a fast convergent integral. Considering two $\hat{x}$ roof-top current basis functions reaction with the pulse functions of size w_e with separation y_n in a microstrip structure with substrate thickness h and dielectric constant ϵ_r, for $A \geq \frac{2}{\pi h}$ and $A \gg k_1$, $S(\lambda_x)$ defined in Eq. 4.11 is asymptotically in the form of

$$S(\lambda_x) = P(\lambda_x)Q(\lambda_x) \tag{4.12}$$

where

$$Q(\lambda_x) = \int_A^\infty \frac{2\sin^2(\lambda_y w_e)}{\lambda_y^2\sqrt{\lambda_x^2+\lambda_y^2}} \cos(\lambda_y y_n)\, d\lambda_y \tag{4.13}$$

and

$$P(\lambda_x) = \frac{1}{4}(\epsilon_r - \lambda_x^2 \frac{2\epsilon_r}{1+\epsilon_r}). \tag{4.14}$$

$Q(\lambda_x)$ can be written as

$$Q(\lambda_x) = Q_1(\lambda_x, \delta_1) - \frac{1}{2}[Q_1(\lambda_x, \delta_2) + Q_1(\lambda_x, \delta_3) \tag{4.15}$$

where

$$Q_1(\lambda_x, \delta) = \int_A^\infty \frac{\cos(\lambda_y \delta)}{\lambda_y^2\sqrt{\lambda_x^2+\lambda_y^2}}\, d\lambda_y, \tag{4.16}$$

$$\delta_1 = y_n, \tag{4.17}$$

$$\delta_2 = y_n - 2w_e \tag{4.18}$$

and

$$\delta_3 = y_n + 2w_e. \tag{4.19}$$

When $\delta = 0$, $Q_1(\lambda_x, \delta)$ has an exact form. When $\delta \neq 0$, the integration contour can be deformed in the complex domain along the contour of $\mathrm{Re}(\lambda_y = A)$ and $\mathrm{Im}(\lambda_y \geq 0)$. The final form of $Q_1(\lambda_x, \delta)$ to be evaluated numerically is

$$Q_1(\lambda_x, \delta) = \begin{cases} (\frac{\sqrt{A^2+\lambda_x^2}}{A} - 1)\frac{1}{\lambda_x^2}, & \delta = 0 \\ \frac{\delta^2}{2}\int_0^\infty [e^{j\delta A} f(x) - e^{-j\delta A} f(-x)] e^{-x} dx, & \delta \neq 0 \end{cases} \tag{4.20}$$

where

$$f(x) = \frac{1}{(A\delta + jx)^2\sqrt{(\lambda_x\delta)^2 + (A\delta + jx)^2}}. \tag{4.21}$$

Chapter 5

Infinite Arrays of Microstrip Antennas on Generalized Anisotropic Substrates

In this chapter the problem of infinite arrays of printed antennas on generalized anisotropic substrates is addressed. The antenna elements studied include microstrip dipoles and probe-fed patches. In the analysis, the substrate anisotropy is general in form, with nine components in both the permittivity and permeability tensors. This allows for the study of antennas on uniaxial substrates with tilted optical axis or on gyrotropic substrates. A rigorous full-wave moment method solution is adopted. Numerical results indicate that by neglecting substrate anisotropy, the performance of printed antennas may be greatly affected. Results include cases of biased ferrite substrates, in which the antenna characteristics may be changed (or controlled) by varying the bias magnetic fields.

5.1 Introduction

The material properties of the substrate significantly affect printed antenna performance [1,2,27]. Many practical microwave substrates exhibit anisotropy. There are two types of material anisotropy, electric and magnetic anisotropy. For materials with electric anisotropy, the permittivity may be different in different directions. Along each of the three principal axes the permittivity may be characterized by a different constant. Useful microwave substrates with electric anisotropy include single-crystal sapphire ($\epsilon_{xx} = \epsilon_{yy} = 9.4$, $\epsilon_{zz} = 11.6$), boron nitride ($\epsilon_{xx} = \epsilon_{yy} = 5.12$, $\epsilon_{zz} = 3.4$), and Epsilam-10 ($\epsilon_{xx} = \epsilon_{yy} = 13$, $\epsilon_{zz} = 10.2$). Magnetized ferrites

exhibit magnetic anisotropy, where the permeability is in the form of a third-rank tensor. The elements of the permeability tensor are related to the external applied dc magnetic field, the microwave frequency, as well as the inherent physical properties of the ferrite material. These ferrite materials, which are usually gyrotropic, are useful in both active and passive circuits due to the fact that the permeability tensor and thus the electrical properties of the material are changed externally by way of the applied dc magnetic field. This aspect may lead to many applications in printed circuit antennas [28,29].

Infinite array analysis is a useful tool for the design of large antenna arrays. It provides a means of characterizing some of the important features of the large finite array, including the variation of element input impedance as a function of scan angle. The use of dielectric cover layers to improve the input impedance match has been described [32,33,34]. Infinite array analysis has been applied to microstrip phased arrays on isotropic dielectric substrates by several investigators [30]-[34]. Pozar and Schaubert discussed the phenomenon of scan blindness in infinite phased arrays of printed dipoles [30]. They also studied the infinite array of patches [31]. The work reported here represents a significant extension of those analyses to the case of generalized anisotropic substrates.

The cited work employed full-wave method of moments solutions [30]-[34]. That formulation has been shown to be accurate and efficient. A fullwave Green's function and method of moments integral equation solution for the anisotropic is presented here. Unlike in the case of the isotropic substrate, the Green's function for a generalized anisotropic substrate is not a simple closed form. The exponential-matrix method [35] provides a useful technique for the generation of the spectral dyadic Green's function.

The most difficult aspect of the analysis of microstrip antenna problems is the modelling of the feeds. For printed dipoles, a delta-gap generator is usually assumed to simulate the two-wire transmission line feed. For probe-fed patches the probes can be modelled as ideal current generators. This has been found to be a very reasonable model for thin substrate cases [31].

In this chapter the effects of substrate anisotropy on the scan characteristics of infinite phased arrays of printed dipoles and patches are investigated. This first centers on the study of the uniaxial substrate with arbitrarily oriented optical axis, in which case all nine components of the permittivity tensor are nonzero. Then the focus is shifted to the study of the scan characteristics of antennas on a ferrite substrate. The effects of the applied dc magnetic field and its direction on the array performance are illustrated through numerical examples.

In Section 5.2 the infinite array analysis including both permittivity and perme-

ability anisotropy is described. The Green's function for a generalized anisotropic substrate is formulated, where both horizontal and vertical current sources are included.

In Section 5.3 the importance of substrate anisotropy is highlighted through a number of numerical examples. Some features of infinite arrays of printed antennas on a ferrite substrates are also discussed.

5.2 Analysis

The geometries of infinite phased arrays of printed dipoles and patches are shown in Figures 5.1 and 5.2, respectively. The substrate thickness is d. All the dipoles are identical with length l and width w. All the patches are identical with length L_x and width L_y. The structure is periodic and the Floquet cell dimensions are a and b in the x- and y- directions, respectively. The antenna elements lie in the x-y plane. The material constants of the grounded substrate are assumed to have the generalized form:

$$\vec{\bar{\mu}} = \mu_0 \begin{bmatrix} \mu_{xx} & \mu_{xy} & \mu_{xz} \\ \mu_{yx} & \mu_{yy} & \mu_{yz} \\ \mu_{zx} & \mu_{zy} & \mu_{zz} \end{bmatrix} \text{ and } \vec{\bar{\epsilon}} = \epsilon_0 \begin{bmatrix} \epsilon_{xx} & \epsilon_{xy} & \epsilon_{xz} \\ \epsilon_{yx} & \epsilon_{yy} & \epsilon_{yz} \\ \epsilon_{zx} & \epsilon_{zy} & \epsilon_{zz} \end{bmatrix}. \tag{5.1}$$

In progressively phased arrays, the current on each antenna must be phased in accordance with the scan angle $(\theta,\ \phi)$ as

$$e^{jk_0(m\Psi_x a + n\Psi_y b)} \tag{5.2}$$

where

$$\Psi_x = \sin\theta\ \cos\phi,\ \ \Psi_y = \sin\theta\ \sin\phi\,, \tag{5.3}$$

and m and n are the indices for each antenna in the infinite array.

The Green's function for an infinite array of printed antennas [30] has the form:

$$G(x,\ y) = \frac{1}{ab} \sum_{m=-\infty}^{\infty} \sum_{n=-\infty}^{\infty} \tilde{G}(k_x,\ k_y)\ e^{jk_x(x-x')}\ e^{jk_y(y-y')} \tag{5.4}$$

where

$$k_x = \frac{2\pi m}{a} + k_0\Psi_x,\ \ k_y = \frac{2\pi n}{b} + k_0\Psi_y \tag{5.5}$$

and $\tilde{G}(k_x,\ k_y)$ is the spectral Green's function. In the case of the generalized anisotropic substrate, this spectral Green's function may be obtained by using a exponential matrix method.

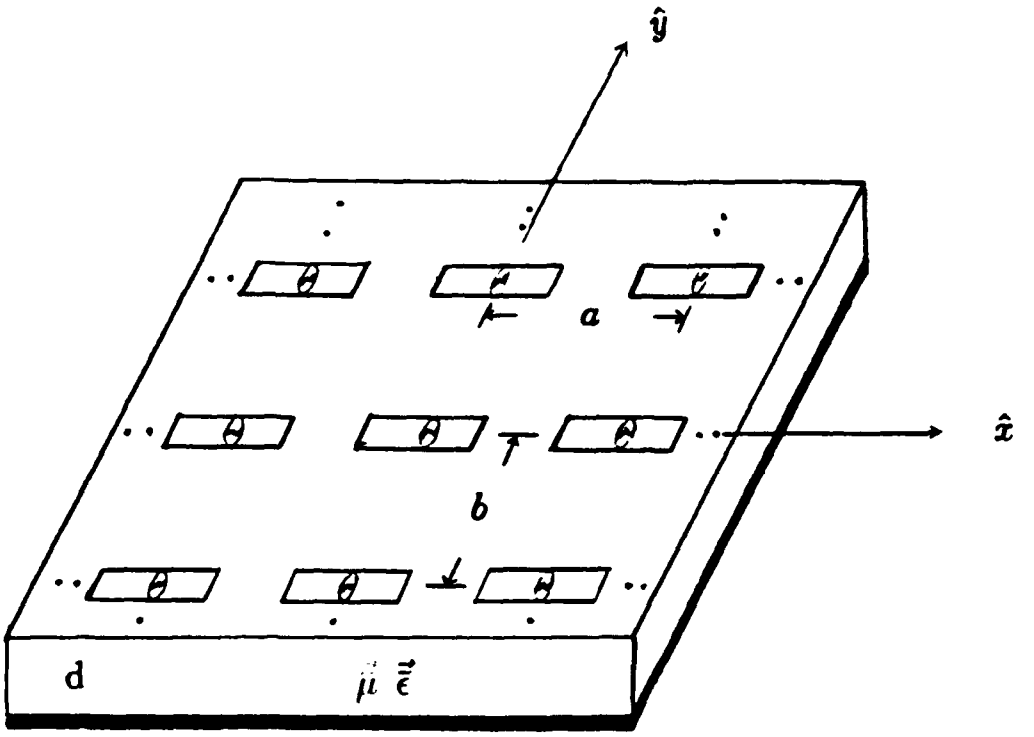

Figure 5.1: Infinite Array of Printed Dipoles on a Generalized Anisotropic Substrate.

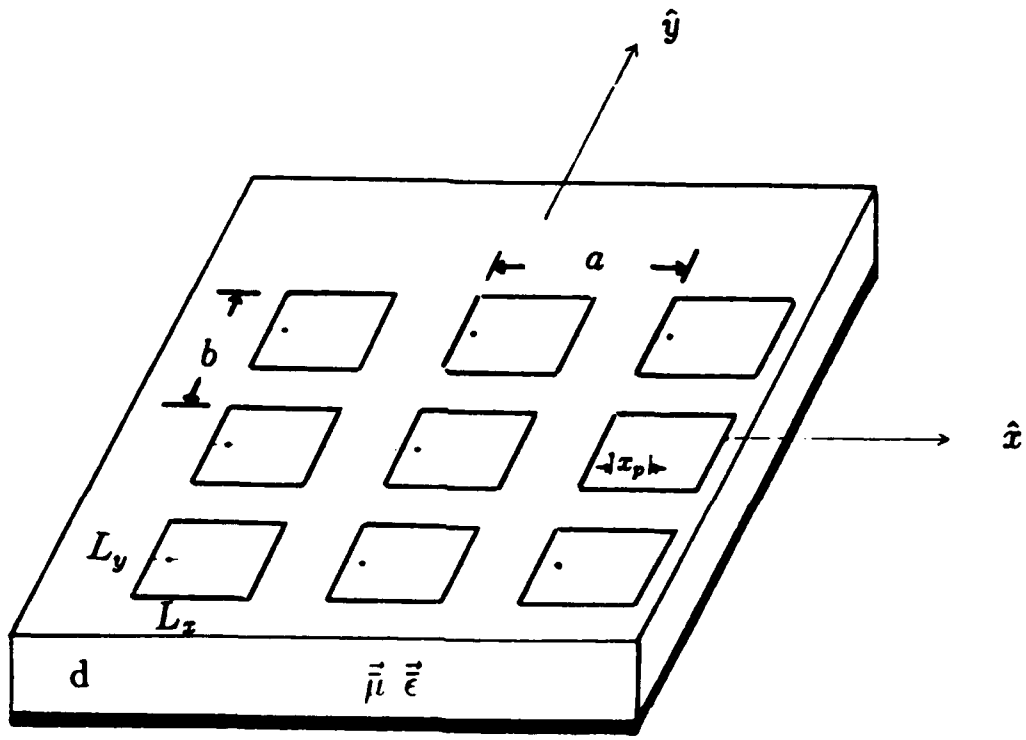

Figure 5.2: Infinite Array of Probe-fed Patches on a Generalized Anisotropic Substrate.

Using the 2-D Fourier transformation

$$\begin{matrix}\vec{E}\\ \vec{H}\end{matrix} = \frac{1}{ab}\sum_{n=-\infty}^{\infty}\sum_{m=-\infty}^{\infty}\begin{matrix}\tilde{E}\\ \tilde{H}\end{matrix}(k_x,\, k_y)\, e^{-jk_x x}\, e^{-jk_y y}\, dk_x\, dk_y, \tag{5.6}$$

in Maxwell's curl equations, one obtains

$$-j\mathbf{k}\times\tilde{H} + \frac{\partial}{\partial z}(\hat{z}\times\tilde{H}) = j\omega\vec{\bar{\epsilon}}\cdot\tilde{E} + \tilde{J}\,\delta(z-z') \tag{5.7}$$

and

$$-j\mathbf{k}\times\tilde{E} + \frac{\partial}{\partial z}(\hat{z}\times\tilde{E}) = -j\omega\vec{\bar{\mu}}\cdot\tilde{H}, \tag{5.8}$$

with $\mathbf{k} = k_x\hat{x}+k_y\hat{y}$. $\tilde{E}$ and $\tilde{H}$ are the spectral electric and magnetic fields; moreover

$$\tilde{E} = \tilde{E}_x\hat{x} + \tilde{E}_y\hat{y} + \tilde{E}_z\hat{z} \tag{5.9}$$

and

$$\tilde{H} = \tilde{H}_x\hat{x} + \tilde{H}_y\hat{y} + \tilde{H}_z\hat{z}. \tag{5.10}$$

After some algebraic manipulations, Eqs. 5.7 - 5.8 can be written in the form of a set of linear differential equations:

$$\frac{\partial}{\partial z}[\tilde{\psi}(z)] = [A]\,[\tilde{\psi}(z)] + [\tilde{f}]\delta(z-z') \tag{5.11}$$

where

$$[\tilde{\psi}(z)] = \begin{bmatrix} k_x\tilde{H}_x(z) + k_y\tilde{H}_y(z)\\ k_y\tilde{H}_x(z) - k_x\tilde{H}_y(z)\\ k_x\tilde{E}_x(z) + k_y\tilde{E}_y(z)\\ k_y\tilde{E}_x(z) - k_x\tilde{E}_y(z)\end{bmatrix} \text{ and } [A] = \begin{bmatrix} a_{11} & a_{12} & a_{13} & a_{14}\\ a_{21} & a_{22} & a_{23} & a_{24}\\ a_{31} & a_{32} & a_{33} & a_{34}\\ a_{21} & a_{42} & a_{43} & a_{44}\end{bmatrix}. \tag{5.12}$$

In Eq. 5.11, $[\tilde{\psi}]$ is a 4×1 vector containing the Fourier transforms of the tangential E and H fields. [A] is a 4×4 complex matrix whose elements are completely described by the material parameters $\bar{\bar{\epsilon}}$ and $\bar{\bar{\mu}}$, and the Fourier transform variables k_x and k_y. $[\tilde{f}]$ is a 4×1 vector containing the Fourier transforms of any sources that might be in the layer. For horizontal current sources one has

$$[\tilde{f}] = [U_x] = \begin{bmatrix} -k_y\\ k_x\\ 0\\ 0\end{bmatrix} \text{ or } [\tilde{f}] = [U_y] = \begin{bmatrix} k_x\\ -k_y\\ 0\\ 0\end{bmatrix}. \tag{5.13}$$

$[U_x]$ is for the current source in the x direction, while $[U_y]$ is for the current source in the y direction. For vertical current sources (probes) one writes

$$[\tilde{f}] = [U_x] = \begin{bmatrix} \frac{k_y\epsilon_{zz}-k_z\epsilon_{yz}}{\epsilon_{zz}}\\ -\frac{k_z\epsilon_{xz}+k_y\epsilon_{yz}}{\epsilon_{zz}}\\ \frac{k^2}{\omega\epsilon_0\epsilon_{zz}}\\ 0\end{bmatrix}. \tag{5.14}$$

The solution of Eq. 5.11 can be found by using the Cayley-Hamilton theorem [35] or using eigenvector analysis. The results from either method are equivalent and yield terms each of which has a z-dependence of the form $e^{\lambda_j z}$, where λ_j are the eigenvalues of the [A] matrix.

5.2.1 Integral Equation and Green's Function for Infinite Probe-fed Patch Arrays

The integral equation for infinite probe-fed patch arrays has the form

$$\int \begin{bmatrix} G_{xx} & G_{xy} \\ G_{yx} & G_{yy} \end{bmatrix} \begin{bmatrix} J_x \\ J_y \end{bmatrix} ds_1 + \int \begin{bmatrix} G_{xz} \\ G_{yz} \end{bmatrix} J_z ds_2 = 0, \tag{5.15}$$

where G_{xx}, G_{xy}..... are in the spectral form of Eq. 5.6.

To find the dyadic Green's function for patch antennas, we describe the fields by a vector $[\psi]$ given by Eq. 5.12. The unknown constants can then be found by applying the appropriate boundary conditions at each layer interface. The solution of Eq. 5.11 is

$$[\tilde{\psi}(z_1)] = [T(z_1 - z_2)]\,[\tilde{\psi}(z_2)], \tag{5.16}$$

where

$$[T(z)] = [\tilde{\phi}] \begin{bmatrix} e^{\lambda_1 z} & 0 & 0 & 0 \\ 0 & e^{\lambda_2 z} & 0 & 0 \\ 0 & 0 & e^{\lambda_3 z} & 0 \\ 0 & 0 & 0 & e^{\lambda_4 z} \end{bmatrix} [\tilde{\phi}]^{-1}, \tag{5.17}$$

in which the $\lambda_i, i = 1,2,3,4$ are the eigenvalues and $[\tilde{\phi}]$ is a 4×4 eigenvector matrix of [A]. (For the isotropic case there would be repeated eigenvalues, and the terms of the exponential matrix could be greatly simplified and would exhibit *sinh* and *cosh* behavior.) According to the Calley-Hamilton theorem, the matrix $[T(z)]$ can also be expressed as

$$[T(z)] = \sum_{n=0}^{3} C_n(z)[A]^n, \tag{5.18}$$

where the coefficients C_n are taken from the solution of the matrix equation

$$e^{\lambda_j(z)} = \sum_{k=0}^{3} \lambda_j^k C_k(z), \quad j = 1,\ 2,\ 3,\ 4. \tag{5.19}$$

It is quite clear that the physical meaning of the matrix [T] is to relate the tangential electromagnetic fields at one surface ($z = z_1$) to another ($z = z_2$). For

the geometry shown in Figure 5.2, the tangential electromagnetic fields at the air-ferrite interface can now be related to those at the ground plane:

$$[\tilde{\psi}(d)] = [T(d)]\,[\tilde{\psi}(0)]\,. \tag{5.20}$$

The electromagnetic fields in the air ($z \geq d$) can be derived in a straightforward manner. With this result together with the boundary conditions that the tangential electric fields are zero at the ground plane, one obtains

$$[\tilde{\psi}(d)] = \begin{bmatrix} j\sqrt{k^2 - k_0^2}\,\tilde{a} \\ \omega\epsilon_0\,\tilde{b} \\ j\sqrt{k^2 - k_0^2}\,\tilde{b} \\ -\omega\mu_0\,\tilde{a} \end{bmatrix} \text{ and } [\tilde{\psi}(0)] = \begin{bmatrix} \tilde{c} \\ \tilde{d} \\ 0 \\ 0 \end{bmatrix}, \tag{5.21}$$

where $\tilde{a}$, $\tilde{b}$, $\tilde{c}$ and $\tilde{d}$ are unknown spectral quantities to be determined.

With the current source at the air-ferrite interface, the electromagnetic fields just above and below z=d are related as

$$[\tilde{\psi}(d)] - [T(d)][\tilde{\psi}(0)] = [U_I], \tag{5.22}$$

where $[U_I]$ is either $[U_x]$ or $[U_y]$. Eq. 5.22 involves a 4 by 4 matrix equation, where the solution determines the quantities $\tilde{a}$, $\tilde{b}$, $\tilde{c}$ and $\tilde{d}$. As a result, the spectral Green's functions for patches are determined from the expressions

$$\tilde{G}_{xx}(k_x,\, k_y) \text{ or } \tilde{G}_{xy}(k_x,\, k_y) = \frac{jk_x\sqrt{k_x^2 + k_y^2 - k_0^2}\tilde{b} - \omega\mu_0 k_y \tilde{a}}{k_x^2 + k_y^2} \tag{5.23}$$

and

$$\tilde{G}_{yx}(k_x,\, k_y) \text{ or } \tilde{G}_{yy}(k_x,\, k_y) = \frac{jk_y\sqrt{k_x^2 + k_y^2 - k_0^2}\tilde{b} + \omega\mu_0 k_x \tilde{a}}{k_x^2 + k_y^2}. \tag{5.24}$$

When $[U_I] = [U_x]$, the above two equations are for $\tilde{G}_{xx}(k_x,\, k_y)$ and $\tilde{G}_{yx}(k_x,\, k_y)$; while when $[U_I] = [U_y]$, the above two equations are for $\tilde{G}_{xy}(k_x, k_y)$ and $\tilde{G}_{yy}(k_x, k_y)$.

The Green's function for the probes can be found by solving the following matrix equation.

$$[T(z' - d)][\tilde{\psi}(d)] - [T(z')][\tilde{\psi}(0)] = [U_z], \tag{5.25}$$

or

$$[\tilde{\psi}(d)] - [T(d)][\tilde{\psi}(0)] = [T(d - z')][U_z], \tag{5.26}$$

where $[U_z]$ is defined in Eq. 5.14. With $[\tilde{\psi}(d)]$ and $[\tilde{\psi}(0)]$ defined in Eq. 5.21, the expression for $\tilde{G}_{zz}$ and $\tilde{G}_{yz}$ can be found from Eqs. 5.23 and 5.24 by replacing $\tilde{G}_{xx}$ by $\tilde{G}_{zz}$ and $\tilde{G}_{xy}$ by $\tilde{G}_{yz}$.

5.2.2 Method of Moments for Infinite Patch Arrays

In the moment method procedure, the unknown current distribution on the patches is expanded in terms of a set of entire domain basis functions:

$$J_x = \sum_i I_i^x \bar{J}_i^x(x, y) \tag{5.27}$$

and

$$J_y = \sum_i I_i^y \bar{J}_i^y(x, y), \tag{5.28}$$

where

$$\bar{J}_i^x = \frac{1}{L_y} \sin\frac{k\pi}{L_x}(x + L_x/2) \cos\frac{l\pi}{L_y}(y + L_y/2) \tag{5.29}$$

and

$$\bar{J}_i^y = \frac{1}{L_x} \cos\frac{k\pi}{L_x}(x + L_x/2) \sin\frac{l\pi}{L_y}(y + L_y/2). \tag{5.30}$$

The current on the probes is assumed to be constant along the vertical direction (z axis), and to have a delta-function form in the x-y plane: $\delta(x - x_p)\delta(y - y_p)$.

With the same expansion and testing functions in the integral equation, one obtains the matrix equation

$$\sum_j Z_{ij} I_j = V_i \text{ for all } i, \tag{5.31}$$

where Z_{ij} is in the form of

$$Z_{ij} = \frac{1}{ab} \sum_m \sum_n \tilde{J}_i \tilde{G} \tilde{J}_j^{\,*}. \tag{5.32}$$

$\tilde{G}$ being any of the four dyadic components $\tilde{G}_{xx}$, $\tilde{G}_{xy}$, $\tilde{G}_{yx}$, $\tilde{G}_{yy}$, and $\tilde{J}_j$, the Fourier transform of the expansion or testing function. The components of the excitation or voltage matrix which is due to the probe current take the form of

$$V_j = \frac{1}{ab} \sum_m \sum_n \tilde{J}_j^{\,x} \tilde{G}_{xz}\, e^{-jk_x x_p}\, e^{-jk_y y_p} \tag{5.33}$$

or

$$V_j = \frac{1}{ab} \sum_m \sum_n \tilde{J}_j^{\,y} \tilde{G}_{yz}\, e^{-jk_x x_p}\, e^{-jk_y y_p}. \tag{5.34}$$

The method of moments provides the currents on the patches. The input impedance from the probe is calculated as

$$Z_{\text{in}} = \frac{-1}{I_p^2} \int_0^d E_z^p dz, \tag{5.35}$$

where I_p is the current on the probe and $E_z^p(z)$ is the electric field due to the currents on the patch. If reciprocity applied, the input impedance could be written as

$$Z_{\text{in}} = -\sum_j I_j V_j, \tag{5.36}$$

where V_j is but the matrix element of the excitation matrix in Eq. 5.33. However, for the generalized anisotropic substrate reciprocity no longer holds. Alternative procedures for the computation of the electric fields due to the patch currents are required. One can, from Eq. 5.22, find $[\tilde{\psi}(0)]$ and obtain the lateral electromagnetic fields at any position z from the expression

$$[\tilde{\psi}(z)] = [T(z)]\,[\tilde{\psi}(0)]. \tag{5.37}$$

Further, the spectral electric field $\tilde{E}_z$ can be related to the lateral electromagnetic fields through

$$\epsilon_0\epsilon_{zz}\tilde{E}_z = k_y\tilde{H}_x - k_x\tilde{H}_y - \epsilon_0\epsilon_{zx}\tilde{E}_x - \epsilon_0\epsilon_{zy}\tilde{E}_y. \tag{5.38}$$

Replacing $\tilde{G}_{zx}$ and $\tilde{G}_{zy}$ in Eq. 5.33 by this spectral field $\tilde{E}_z$, one obtains a voltage matrix V_j^p. As a result, the input impedance of the probe is calculated as

$$Z_{\text{in}} = -\sum_j I_j V_j^p. \tag{5.39}$$

5.2.3 Integral Equation and Green's Function for Infinite dipole Arrays

For narrow microstrip dipoles, the transverse current is usually negligible. Therefore, the corresponding integral equation is simplified to the form

$$\int G_{zz}\, J_z\, ds = -\delta(x - x_a), \tag{5.40}$$

where x_a is the location of the delta gap source. The spectral form of G_{zz} is the same as the one discussed previously for patches. If roof-top basis functions are used in the method of moments, the impedance matrix elements can be expressed as

$$Z_{ik} = \frac{1}{ab}\sum_{m=-\infty}^{\infty}\sum_{n=-\infty}^{\infty} \tilde{G}(k_x, k_y)\,\tilde{j}^2(k_x, k_y)\,e^{-jk_x(i-k)\Delta}, \tag{5.41}$$

where

$$\tilde{j}(k_x, k_y) = 4\frac{\sin(k_y w/2)}{k_y w}\,\frac{1-\cos(k_x\Delta)}{k_x^2\Delta}, \tag{5.42}$$

and Δ is half the length of the basis function. For a center-fed dipole, it is convenient to use an odd number of basis functions such that all the elements in the voltage vector are zero except the center term which is unity. The input impedance, which is the reciprocal of the current at the center of the dipole, can be obtained from the matrix equation $[Z][I] = [V]$.

5.3 Results

The results shown first illustrate the effects of substrate anisotropy on the scan characteristics of infinite phased arrays of printed dipoles. For a uniaxial substrate with an optical axis tilted in the x-z plane, where the optical axis angle measured from the z axis is θ_0, the permittivity tensor is

$$\vec{\vec{\epsilon}} = \epsilon_0 \begin{bmatrix} \epsilon_x \cos^2\theta_0 + \epsilon_z \sin^2\theta_0 & 0 & (\epsilon_x - \epsilon_z)\sin\theta_0\cos\theta_0 \\ 0 & \epsilon_x & 0 \\ (\epsilon_x - \epsilon_z)\sin\theta_0\cos\theta_0 & 0 & \epsilon_x \sin^2\theta_0 + \epsilon_z \cos^2\theta_0 \end{bmatrix} . \tag{5.43}$$

Figures 5.3 and 5.4 show, respectively, E-plane and H-plane scan characteristics, comparing cases with and without material anisotropy. The substrate is PTFE cloth, which exhibits uniaxial anisotropy [36]. It is seen that the effects of substrate anisotropy are quite noticeable for the E-plane but not for the H-plane. Also, the anisotropy in the planar direction (x-y plane) is more important than that in the vertical direction. Figures 5.5 and 5.6 show the scan characteristics for the E and H-planes, respectively, for a sapphire substrate. The characteristic impedance of the feed is assumed matched with the input impedance of the dipole at a broadside scan, and when the substrate is isotropic with $\epsilon_r = 9.4$. In addition to the results for the isotropic case, the results for four different directions of the optical axis are also shown in Figures 5.5 and 5.6 ($\theta_0 = 0^o$, 30°, 60°, 90°). It is seen that the substrate anisotropy introduces a severe input mismatch, although the angle of scan blindness does not change much. The results also show that when $\theta_0 = 0^o$ the mismatch is most severe. In other words, the anisotropy in the z direction is more important than that in the x direction.

Examples of scan characteristics for an infinite array of probe-fed patches on Epsilam-10 substrate are shown in Figures 5.7 and 5.8 for the E and H-planes, respectively. The results for the optical axis in $\theta_0 = 0^o$, 30°, 60°, 90° are shown. It is seen again that the material anisotropy introduces large changes in the patch array element input impedance. Ignoring the material anisotropy in such a case would result in a severely mismatched design.

The permeability tensor of a ferrite substrate is

$$\vec{\vec{\mu}} = \mu_0 \begin{bmatrix} \mu + (1-\mu)\cos^2\phi_0 & (1-\mu)\sin\phi_0\cos\phi_0 & j\kappa\sin\phi_0 \\ (1-\mu)\sin\phi_0\cos\phi_0 & \mu + (1-\mu)\sin^2\phi_0 & -j\kappa\cos\phi_0 \\ -j\kappa\sin\phi_0 & j\kappa\cos\phi_0 & \mu \end{bmatrix} , \tag{5.44}$$

where ϕ_0 is the angle of the direction of the dc bias H field measured from the x axis in the x-y plane. The parameters μ and κ are characterized by the dc magnetic field, the saturation magnetization, and the frequency of operation [9]. The effect of the applied magnetic field on infinite printed dipole arrays is shown in Figure

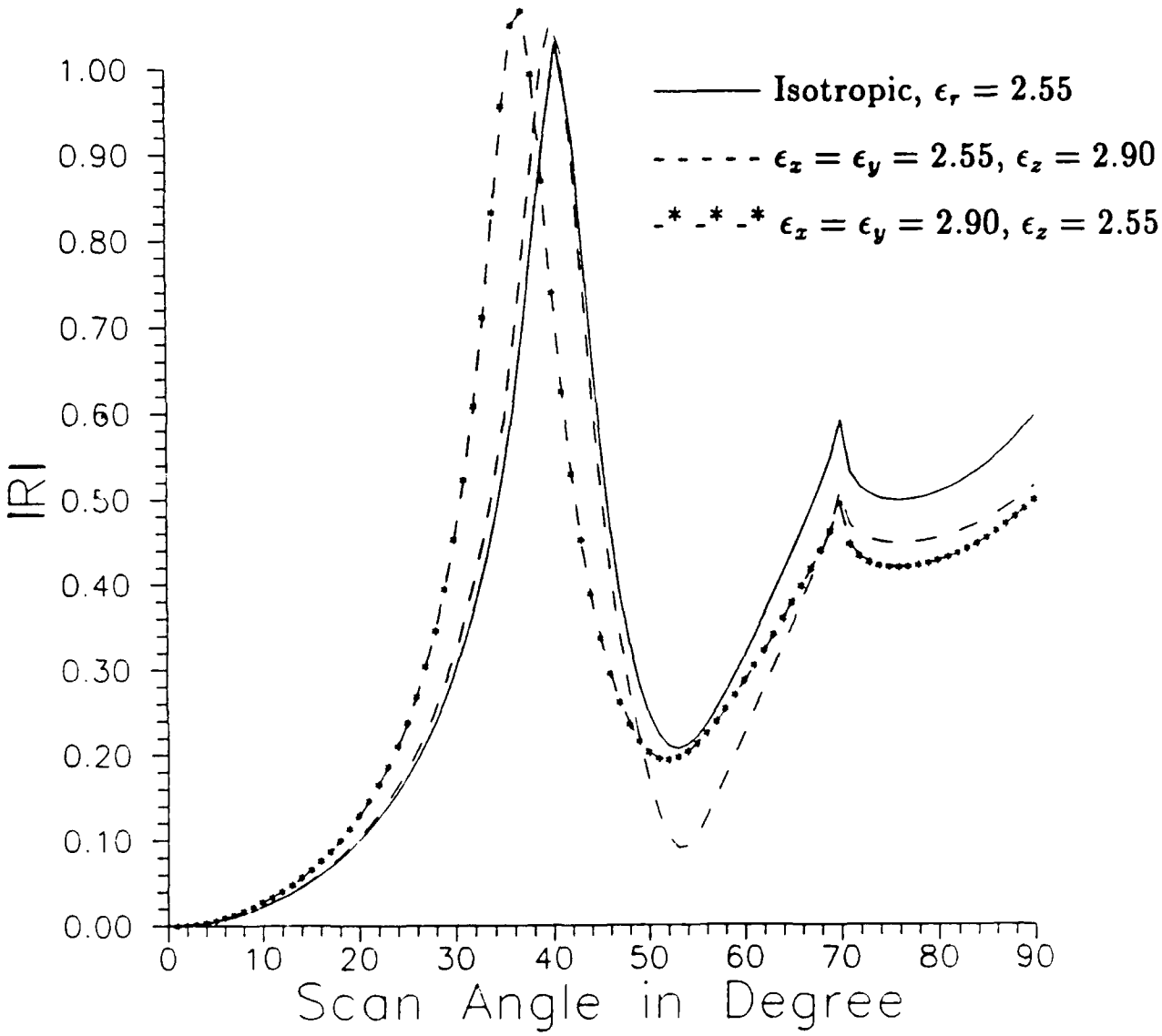

Figure 5.3: Comparison of E-plane Scan Characteristics of Infinite Printed Dipole Array on Uniaxial and Isotropic Dielectric Substrates.

Reflection coefficient magnitude for the E-plane

$d = 0.19\lambda_o$, $a = 0.5155\lambda_o$, $b = 0.5\lambda_o$, $L = 0.39\lambda_o$, $w = 0.002\lambda_o$.

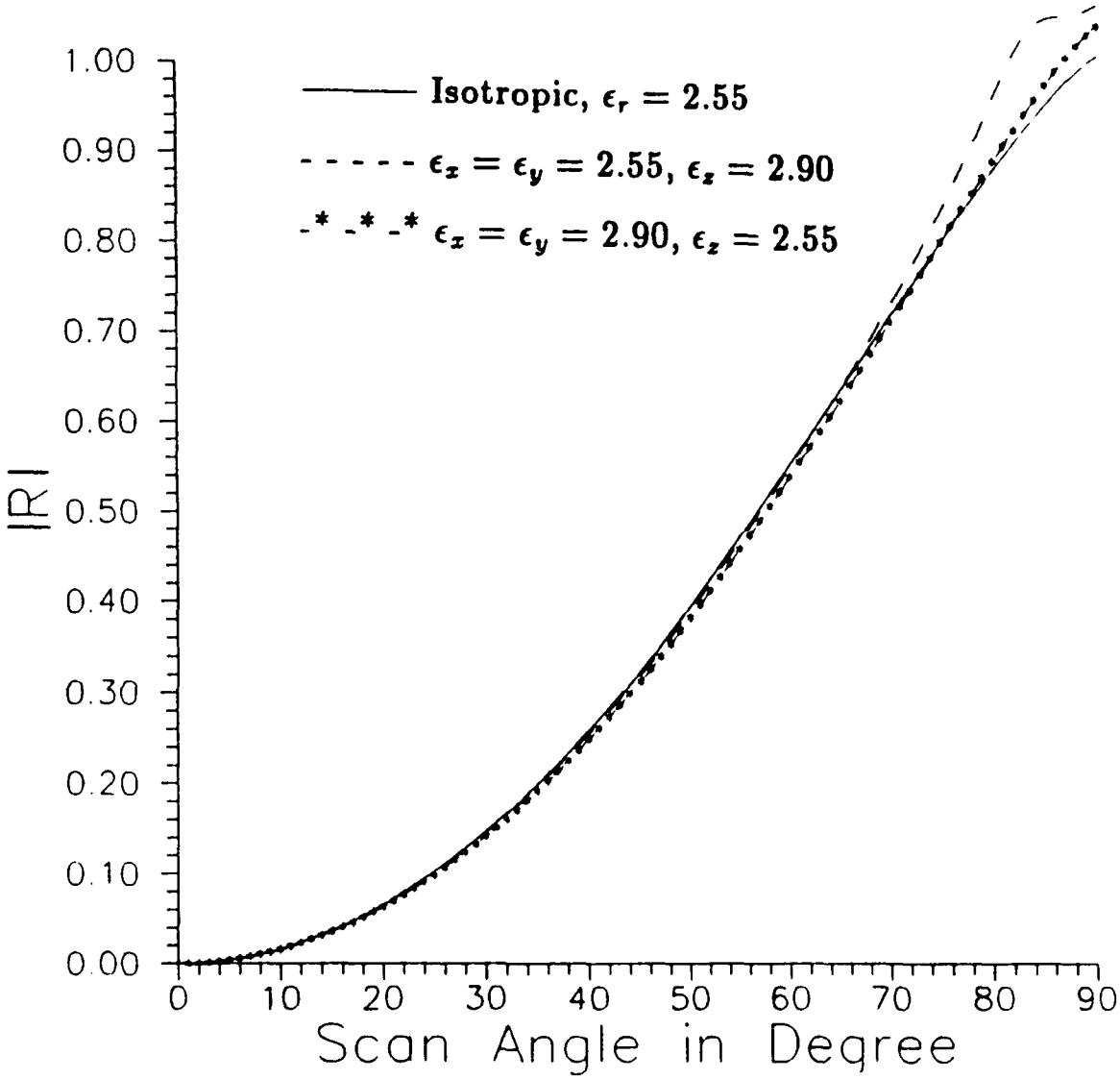

Figure 5.4: Comparison of H-plane Scan Characteristics of Infinite Printed Dipole Array on Uniaxial and Isotropic Dielectric Substrates.

Reflection coefficient magnitude for the H-plane scan.

$d = 0.19\lambda_o$, $a = 0.5155\lambda_o$, $b = 0.5\lambda_o$, $L = 0.39\lambda_o$, $w = 0.002\lambda_o$.

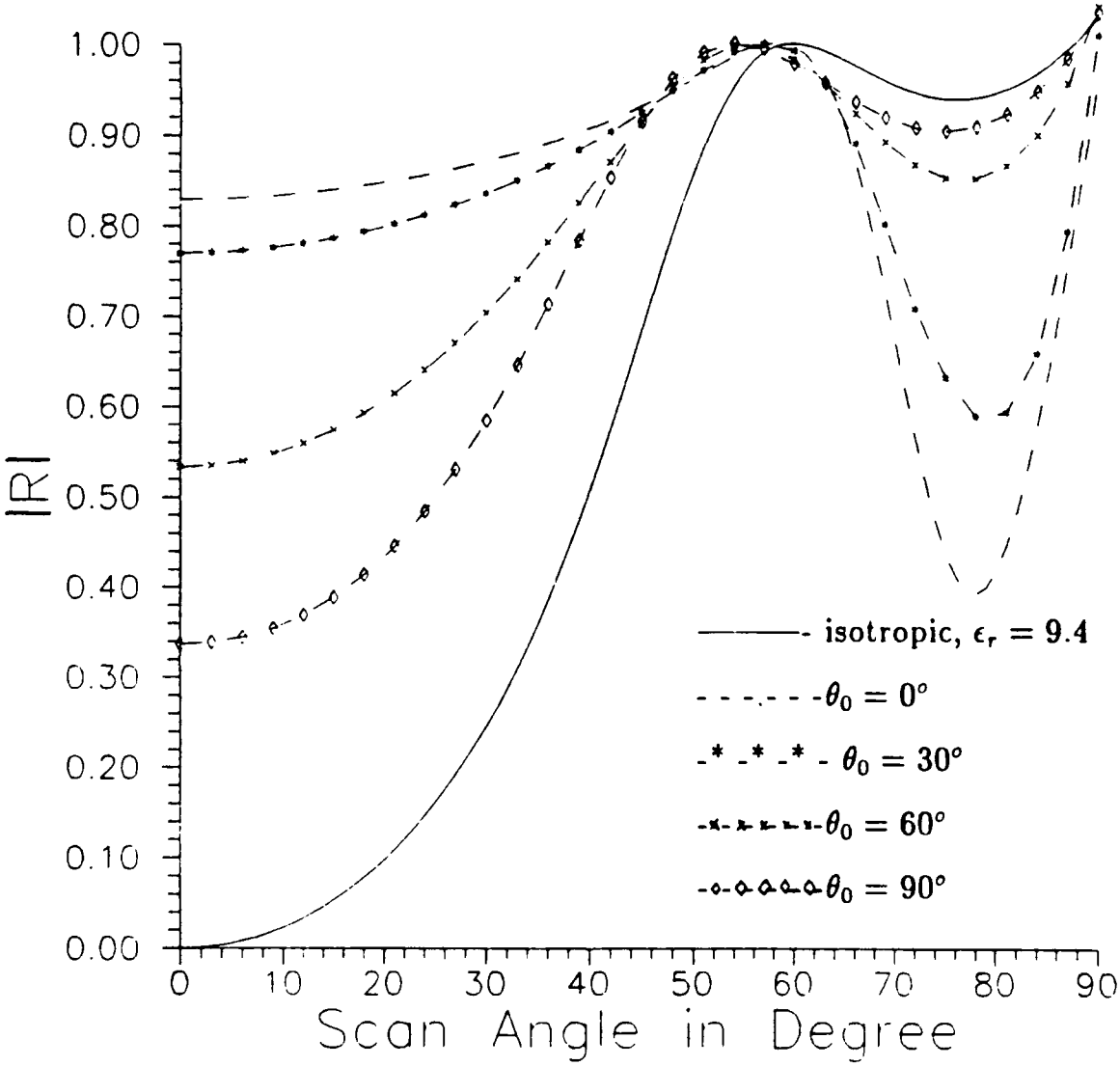

Figure 5.5: E-plane Scan of a Dipole Array on a Uniaxial Substrate with Tilted Optical Axis

Reflection coefficient magnitude for the E-plane scan.
The optical axis tilt angle is θ_o.
$Z_{in} = 8.06 + j0.36$.
$\epsilon_x = \epsilon_y = 9.4$, $\epsilon_z = 11.6$.
$d = 0.06\lambda_o$, $a = 0.5\lambda_o$, $b = 0.5\lambda_o$, $L = 0.186\lambda_o$, $w = 0.002\lambda_o$.

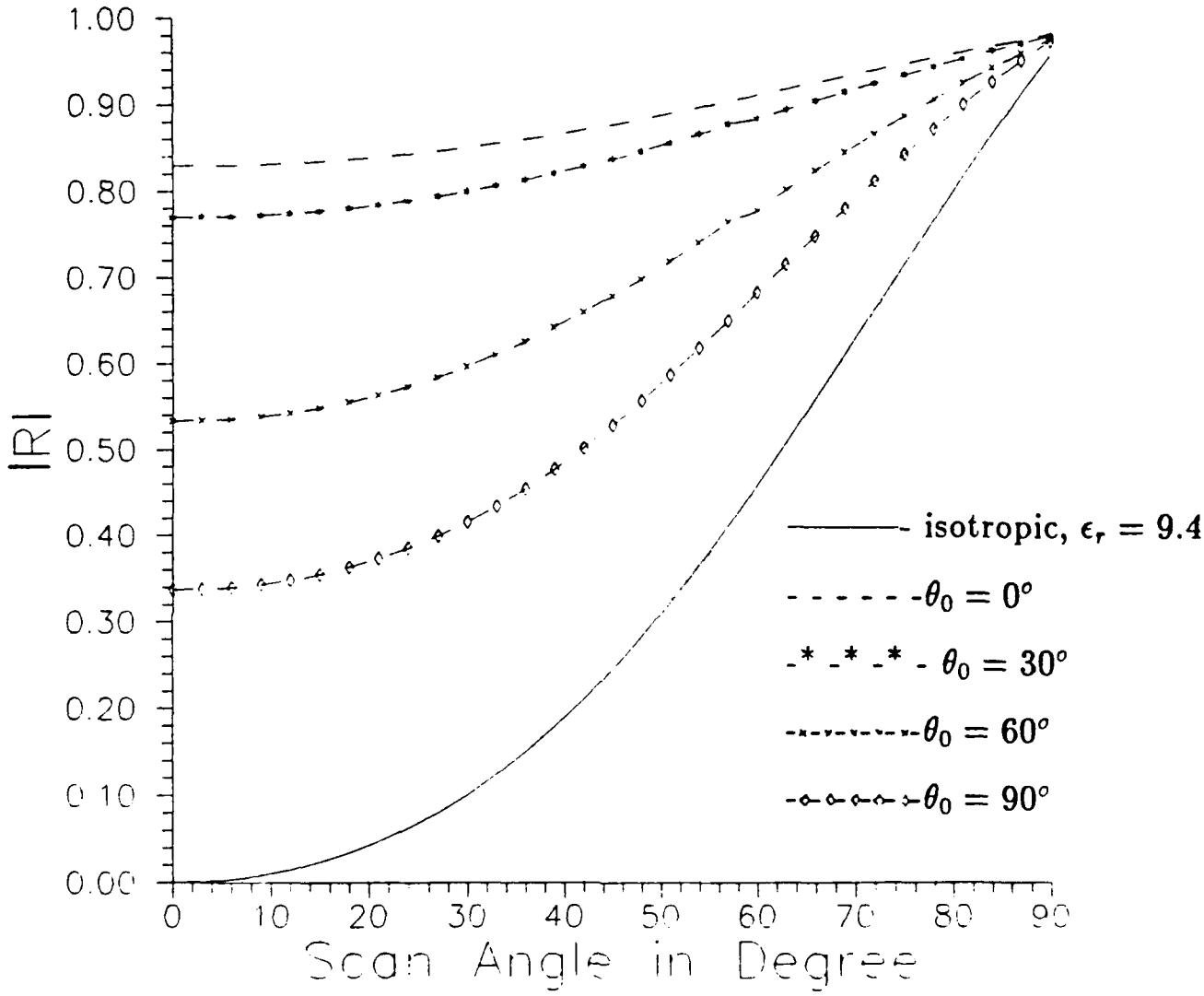

Figure 5.6: H-plane Scan of a Dipole Array on a Uniaxial Substrate with Tilted Optical Axis

Reflection coefficient magnitude for the H-plane scan.
The optical axis tilt angle is θ_o.
$Z_{in} = 8.06 + j0.36$.
$\epsilon_x = \epsilon_y = 9.4$, $\epsilon_z = 11.6$.
$d = 0.06\lambda_o$, $a = 0.5\lambda_o$, $b = 0.5\lambda_o$, $L = 0.186\lambda_o$, $w = 0.002\lambda_o$.

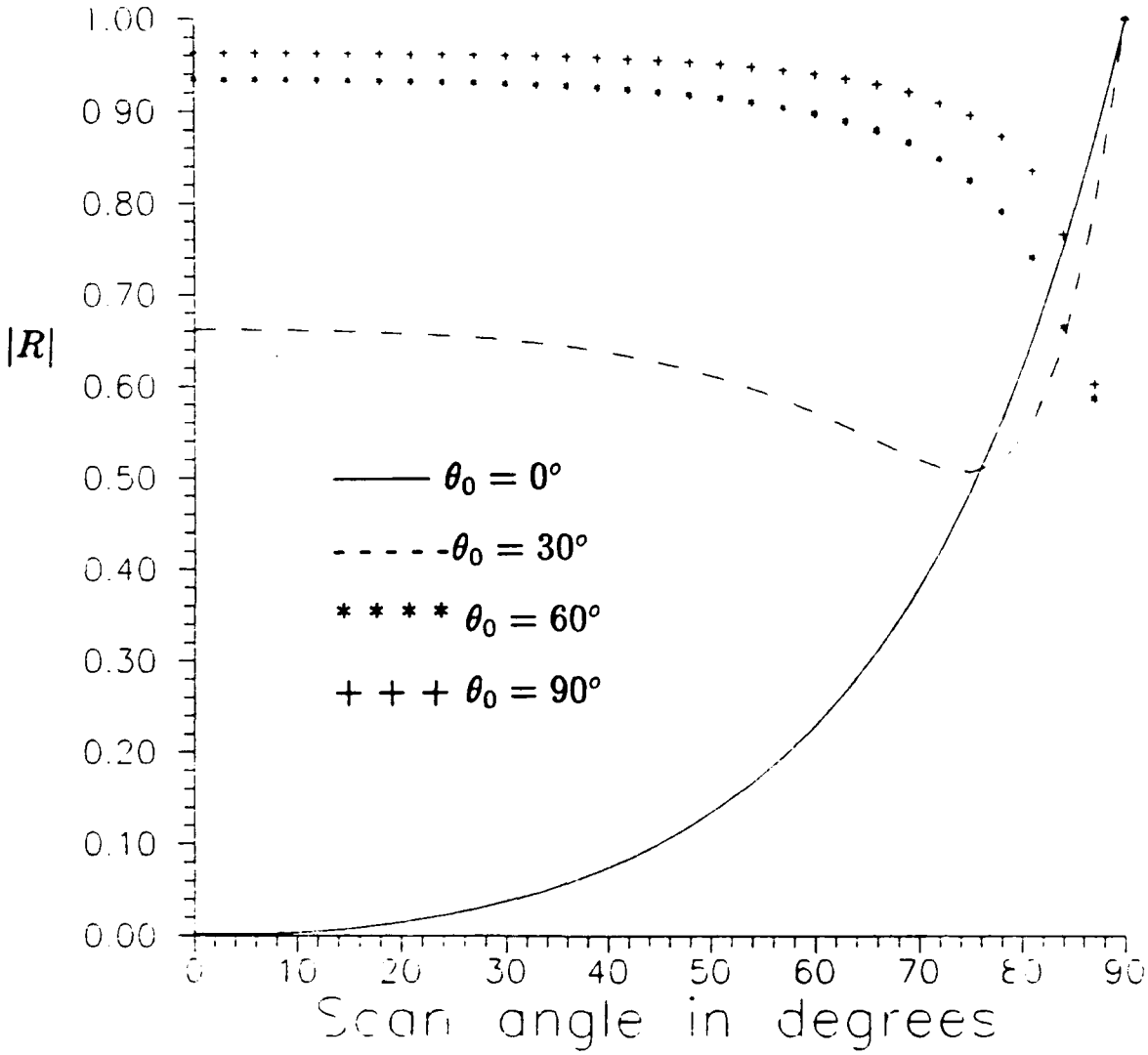

Figure 5.7: E-plane Scan Characteristics of an Infinite Probe-fed Patch Array on a Uniaxial Substrate with Tilted Optical Axis.

Reflection coefficient magnitude for the E-plane scan.
The optical axis tilt angle is θ_o. f = 4.085GHz.
L_x = 1.1cm, L_y = 1.1cm, x_p = 0.165cm, y_p = 0.0cm,
$\epsilon_x = \epsilon_y$ = 13.0, ϵ_z = 10.2.
d = 0.127cm, a = 2.125cm, b = 2.378cm, Z_c = 47 Ω.

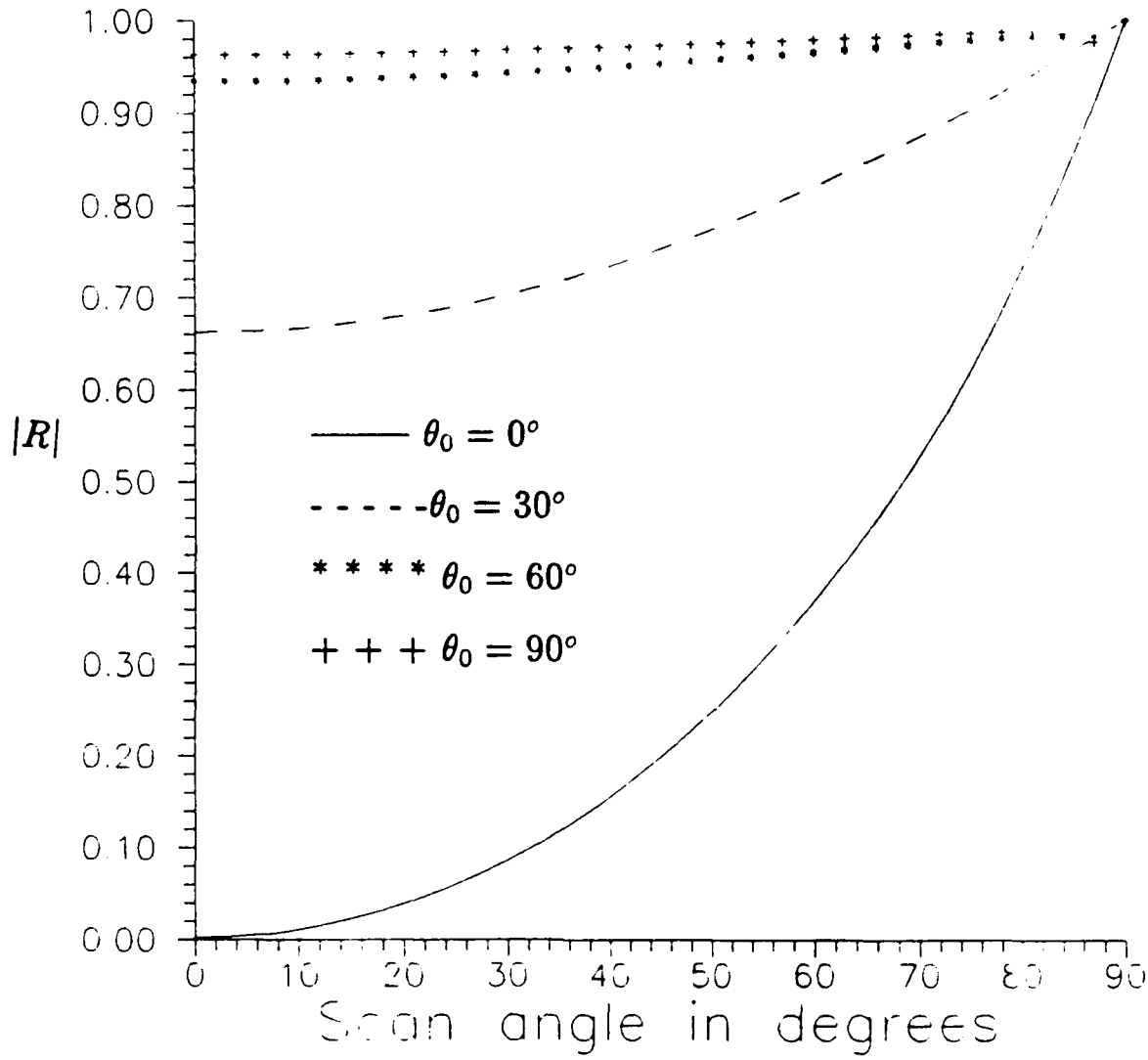

Figure 5.8: H-plane Scan Characteristics of an Infinite Probe-fed Patch Array on a Uniaxial Substrate with Tilted Optical Axis.

Reflection coefficient magnitude for the H-plane scan.
The optical axis tilt angle is θ_o. f = 4.085GHz.
L_x = 1.1cm, L_y = 1.1cm, x_p = 0.165cm, y_p = 0.0cm,
$\epsilon_x = \epsilon_y$ = 13.0, ϵ_z = 10.2.
d = 0.127cm, a = 2.125cm, b = 2.378cm, Z_c = 47 Ω.

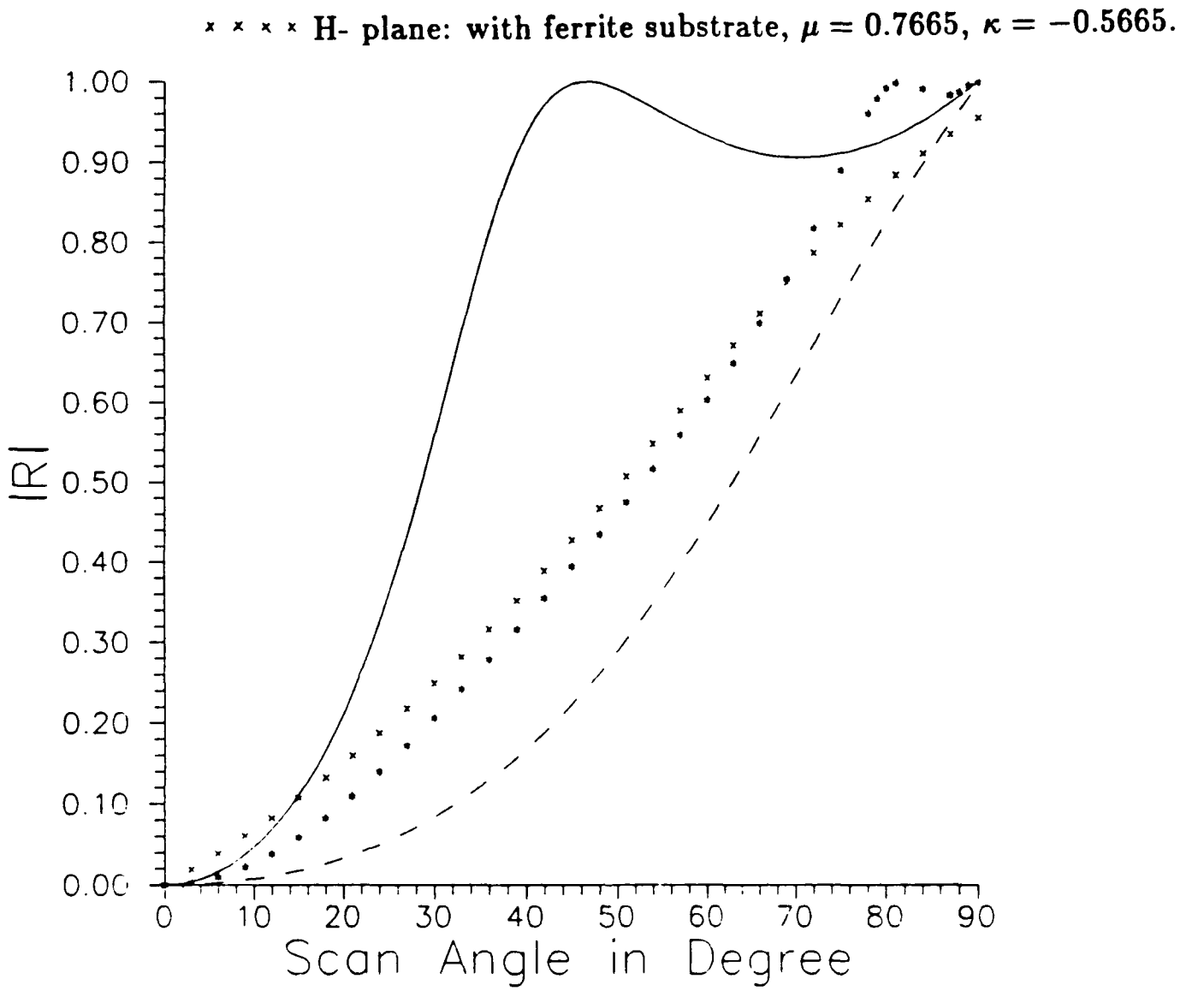

Figure 5.9: Comparison of the Scan Characteristics of Dipole Arrays on Isotropic and Biased Ferrite (gyrotropic) Substrates.

$d = 0.06\lambda_o$, $a = 0.5\lambda_o$, $b = 0.5\lambda_o$, $\epsilon_r = 12.6$, $w = 0.002\lambda_o$.
For the isotropic substrate $L = 0.156\lambda_o$ and $Z_c = 9.3 + j0.30$.
For the ferrite substrate $L = 0.205\lambda_o$ and $Z_c = 0.7 + j0.03$.

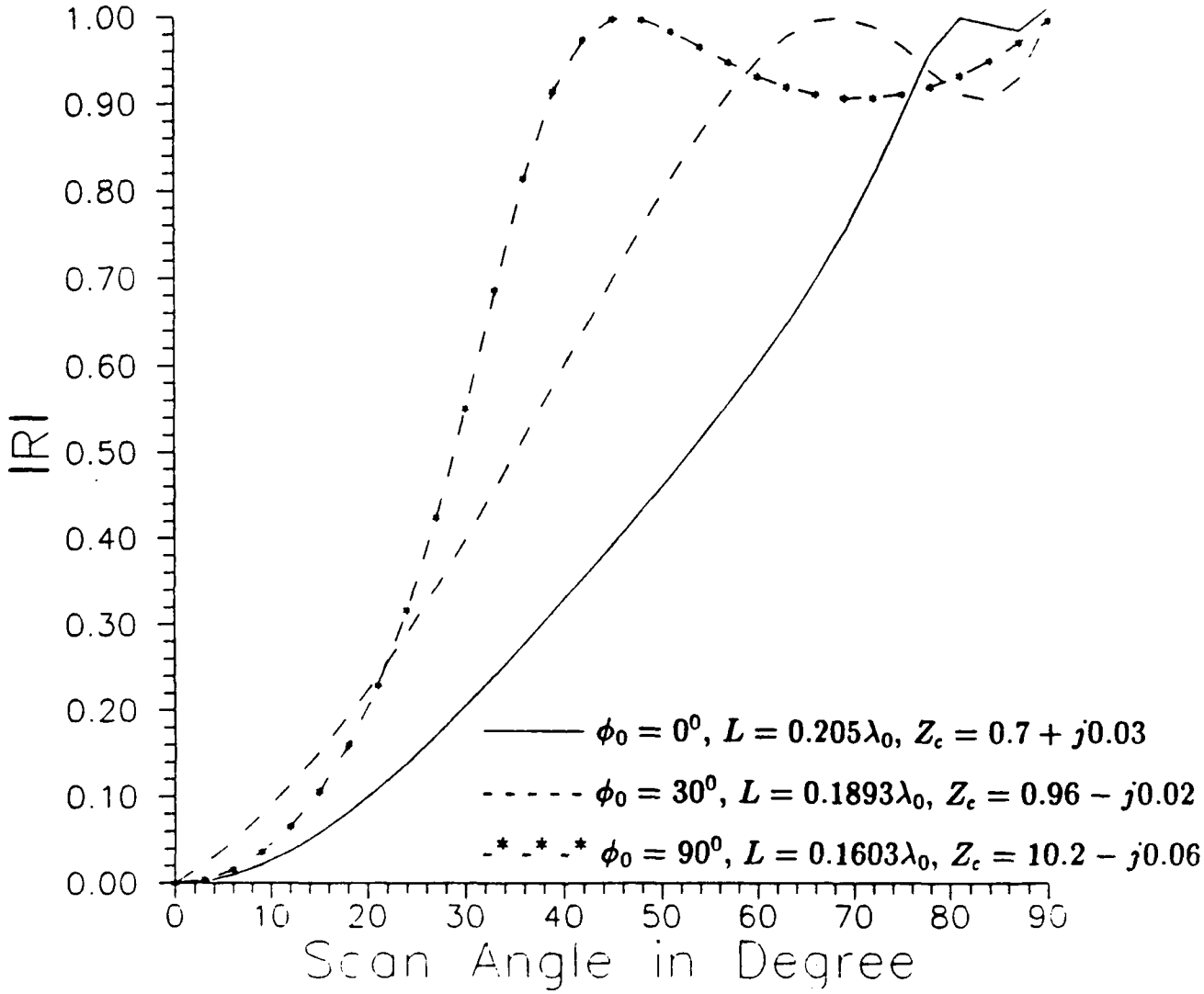

Figure 5.10: E-plane Scan Characteristics of an Infinite Array of Printed Dipoles on a Ferrite Substrate.

$d = 0.06\lambda_o$, $a = 0.5\lambda_o$, $b = 0.5\lambda_o$, $\epsilon_r = 12.6$, $w = 0.002\lambda_o$.
The dc magnetic field direction is (θ_o, ϕ_o), $\mu = 0.7665$, $\kappa = -0.5665$.

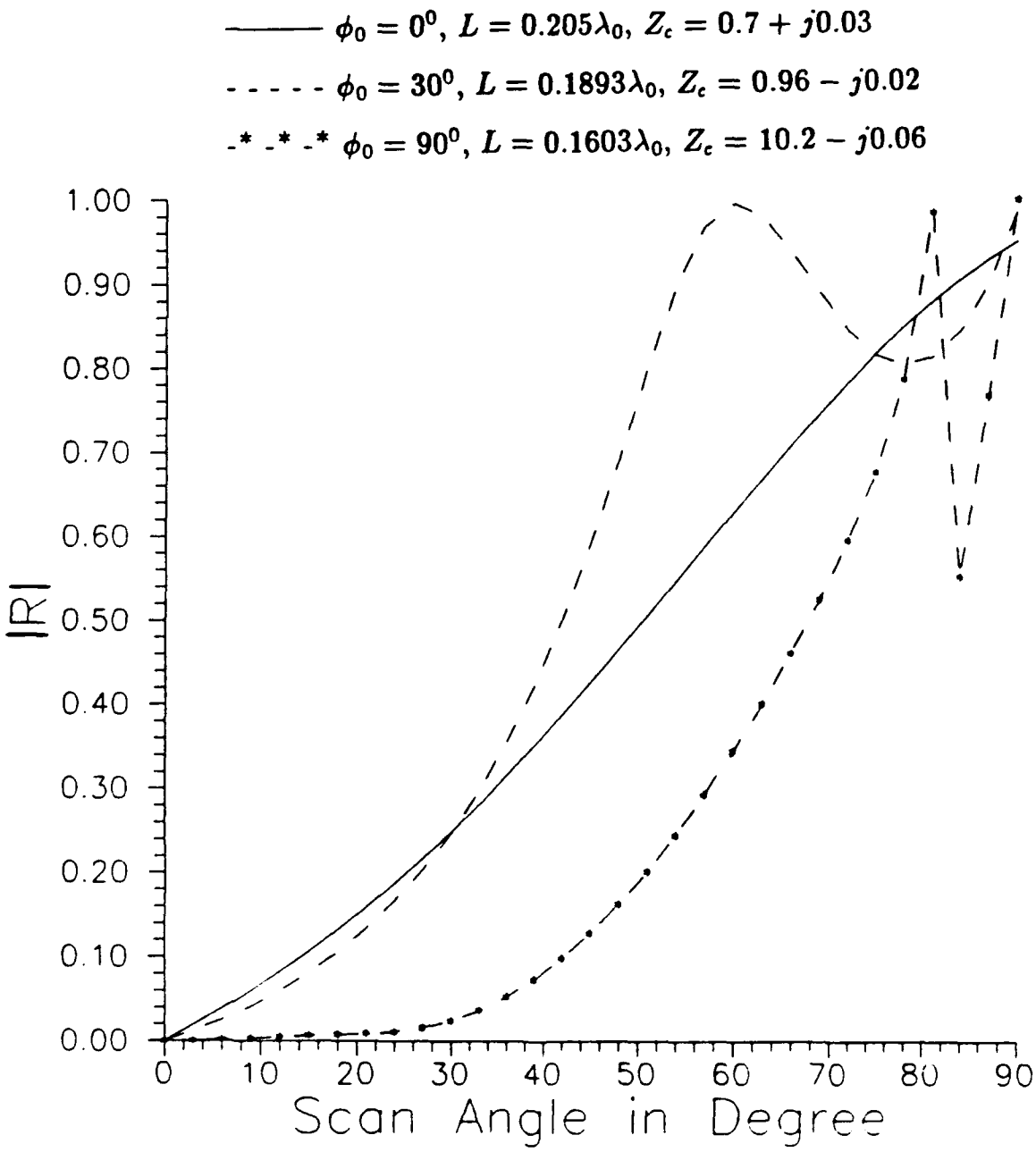

Figure 5.11: H-plane Scan Characteristics of an Infinite Array of Printed Dipoles on a Ferrite Substrate.

$d = 0.06\lambda_o$, $a = 0.5\lambda_o$, $b = 0.5\lambda_o$, $\epsilon_r = 12.6$, $w = 0.002\lambda_o$.
The dc magnetic field direction is (θ_o, ϕ_o), $\mu = 0.7665$, $\kappa = -0.5665$.

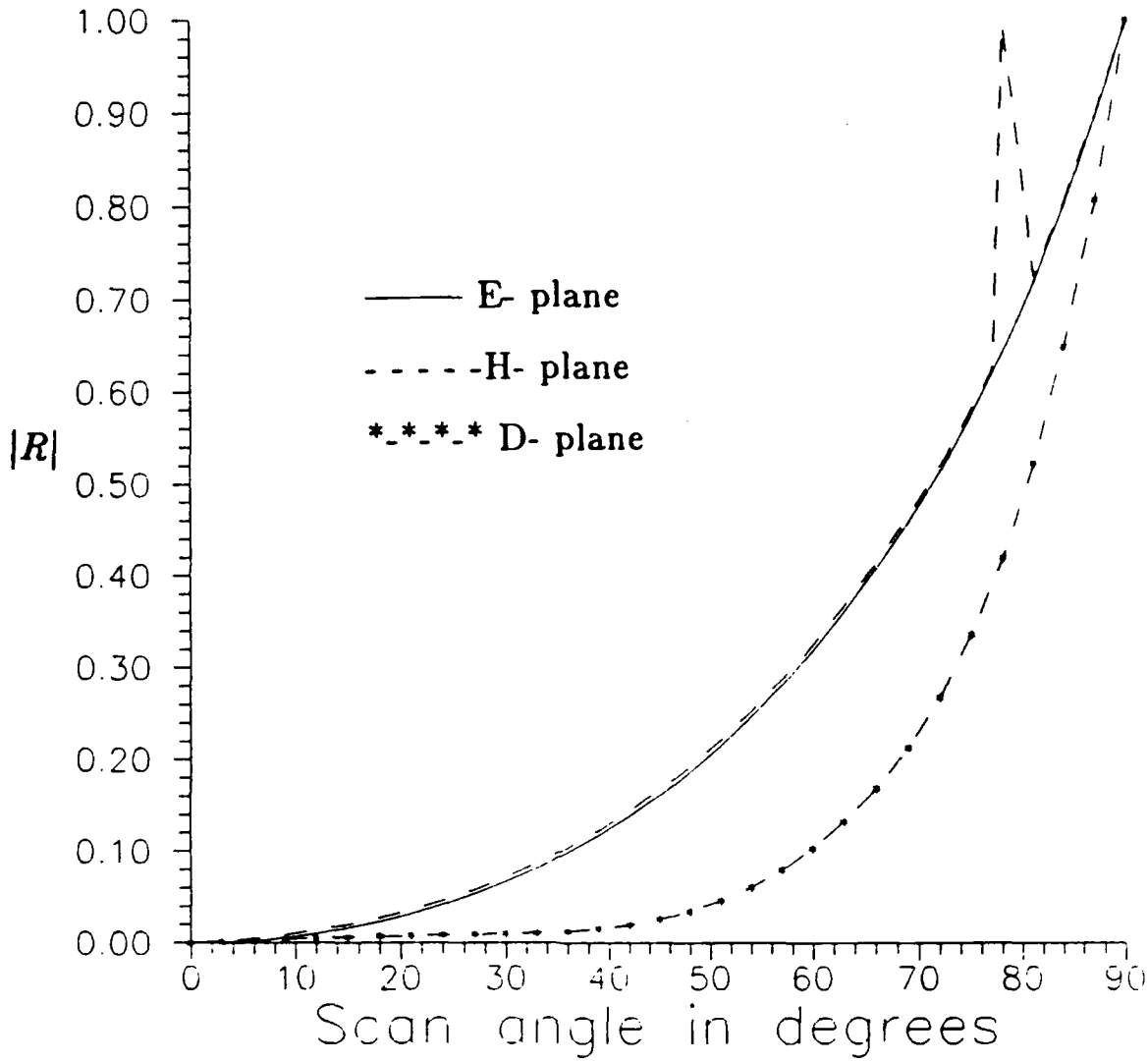

Figure 5.12: Scan Characteristics of an Infinite Probe-fed Patch Array on a Ferrite Substrate.

$f = 0.66$GHz, $d = 0.3175$cm,
$L_x = 2.98$cm, $L_y = 2$cm, $x_p = 0.88$cm, $y_p = 0.0$cm,
$\epsilon_r = 12.6$, $\mu_o H_o = 0.05$T, $\mu_o M_s = 0.275$T, $\theta_o = 90°$, $\phi_o = 0°$,
a = 5 cm, b = 4 cm, and $Z_c = 50\Omega$.

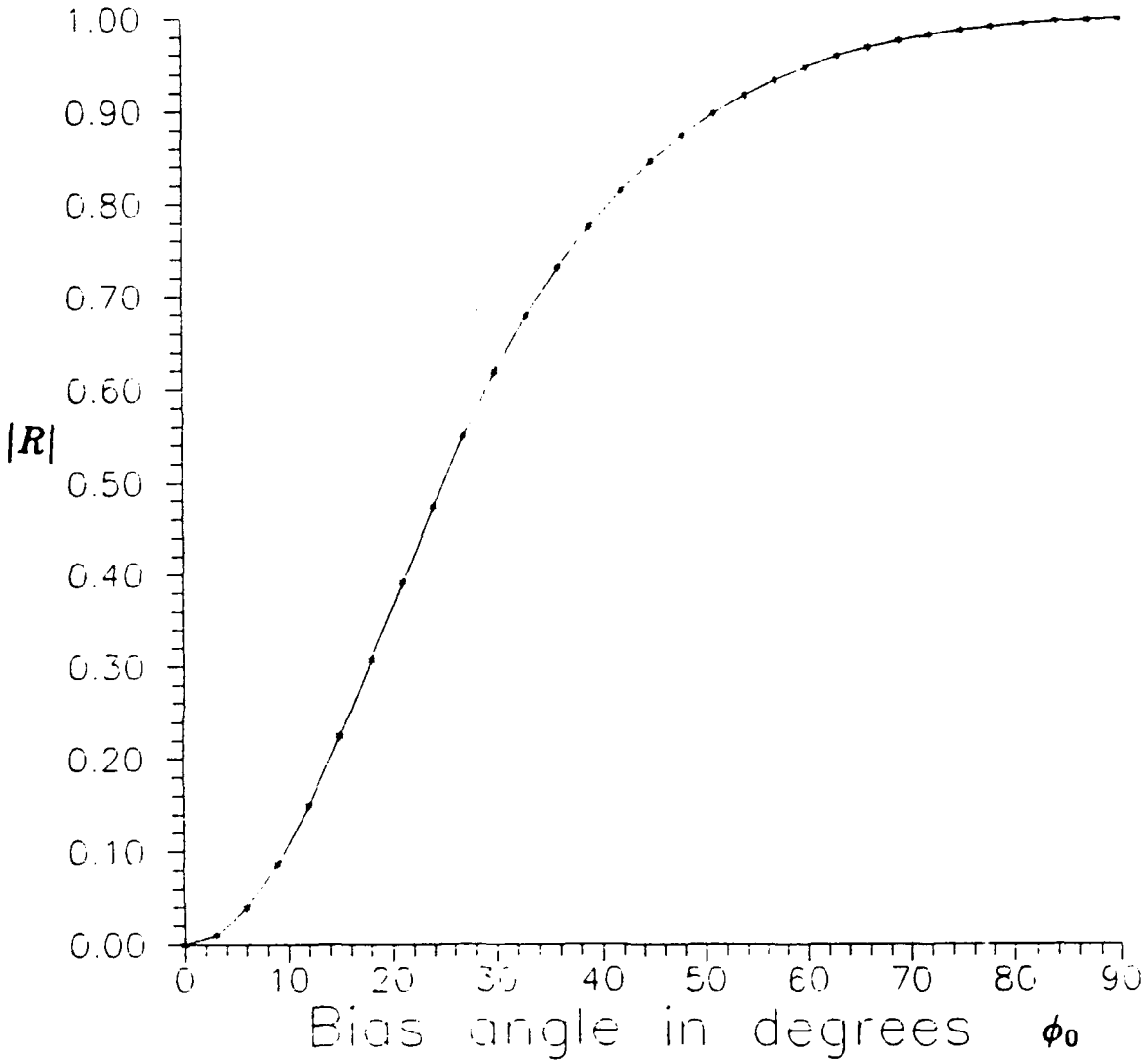

Figure 5.13: Input Reflection Coefficient for the Patch Array on a Biased Ferrite Substrate as a Function of the Bias Field Angle.

$f = 0.66$GHz, $d = 0.3175$cm,
$L_x = 2.98$cm, $L_y = 2$cm, $x_p = 0.88$cm, $y_p = 0.0$cm,
$\epsilon_r = 12.6$, $\mu_o H_o = 0.05$T, $\mu_o M_s = 0.275$T, $\theta_o = 90°$,
a = 5 cm, b = 4 cm, and $Z_c = 50\Omega$.

5.9. The results for an isotropic substrate with no bias are also shown. The results for a ferrite substrate are for the case in which the applied magnetic field is in the x direction (same as the current). It is seen that the input impedance level reduces drastically with a ferrite substrate. The results also show that the scan angle where the scan blindness occurs can be much larger ($> 80^o$) with a biased ferrite substrate (achieved without a reduction of the Floquet cell size). The effects of the direction of the bias magnetic field on the scan characteristics are shown in Figures 5.10 and 5.11 for the E and H-planes, respectively. It is seen that when the dc magnetic field direction is transverse to the direction of the current in the dipole, the scan characteristics are closer to the isotropic case (no applied dc magnetic field). When the direction of the dc magnetic field decreases from $\phi_0 = 90^o$, the E-plane performance improves, while the H-plane scan characteristics are degraded.

The scan characteristics for an infinite probe-fed patch array on a biased ferrite substrate are shown in Figure 5.12. It is seen, as for the dipole case, that the E-plane and H-plane scan characteristics are very much the same. However, it is found, for the patch array, that a scan blindness condition arises in the H-plane but not in E-plane. Also it is seen that the scan performance is much better in the diagonal plane ($\phi = 45^o$), where even at the extreme scan angle of 80 degrees the mismatch not too large ($|R| < 0.40$).

It is known that the bias magnetic field changes the permeability and thus the electrical properties of ferrites. It is therefore possible to adjust the bias H field level and thereby effect changes in the scan performance of an array. It is also seen from Eq. 5.44 that the permeability tensor of ferrites is a strong function of the angle of the bias H field. An example of the effect of the bias angle on the broadside scan input impedance is shown in Figure 5.13. As ϕ_0 varies from 0 to 90 degrees, the input impedance changes from that of a perfect match to one of almost total reflection.

5.3.1 Conclusion

An analysis of infinite phased arrays of printed antennas on generalized anisotropic substrates was developed. It has been applied to uniaxial dielectric substrates, and to gyrotropic (biased ferrite) substrates. From the computed results, it was found that the substrate dielectric anisotropy in commonly used substrates can introduce significant changes in active impedance of the array element. If those anisotropic effects are neglected in the design process the performance of the array can be severely degraded. In the case of a ferrite substrate it was also found that the strength and the direction of the applied magnetic field may affect significantly the scan characteristics of the infinite array. It was observed, in the principal planes, that the angle at which scan blindness occurs may be very large when a

biased ferrite substrate is used, and that this condition can be achieved without reducing the size of the periodic cell.

Bibliography

[1] P.B. Katehi and N.G. Alexopoulos, "On the effect of substrate thickness and permittivity on printed circuit antennas," IEEE Trans. on Antennas Propagat., Vol. AP-31, pp. 34-39, Jan. 1983.

[2] D.R. Jackson and N.G. Alexopoulos, "Fundamental superstrate (cover) effects on printed circuit antennas," IEEE Trans. on Antennas Propagat., Vol. AP-32, pp. 807-815, Aug. 1984.

[3] N.G. Alexopoulos, "Integrated-circuit structures on anisotropic substrate," IEEE Trans. on Microwave Theory and Techniques, Vol. MTT-33, pp. 847-888 Oct. 1985.

[4] D.M. Pozar, "Radiation and scattering from a microstrip patch on a uniaxial substrate," IEEE Trans. on Antennas Propagat., Vol. AP-35, pp. 613-621, June 1987.

[5] R. E. Collin and F. J. Zucker, *Antenna Theory* , McGraw-Hill Book Company, 1969.

[6] H.Y. Yang, A. Nakatani, and J.A. Castaneda,"Efficient Evaluation of Spectral Integrals in the Moment Method Solution of Microstrip Antennas and Circuits," IEEE Trans. on Antennas Propagat., accepted for publication.

[7] I.J. Bahl and P. Bhartia, Microstrip Antennas. Artech. House, Dedham, MA, 1980.

[8] K.R. Carver and J.R. Mink, "Microstrip Antenna Technology," IEEE Trans. Antennas and Propagations, Vol. AP-29, pp. 2-24, 1981.

[9] R.E. Collin, Foudations for Microwave Engineering, McGraw-Hill Book Company, New York, 1966, pp. 286-294.

[10] V. Aulock, Handbook of Microwave Ferrite Materials, Academic Press, New York, 1965.

[11] I.E. Rana and N.G. Alexopoulos, "Current distribution and input impedance of printed dipole," IEEE Trans. on Antennas Propagat., Vol. AP-29, pp. 99-105, Jan. 1981.

[12] C.L. Chi and N.G. Alexopoulos, "Radiation by a probe in a substrate," IEEE Trans. on Antennas Propagat., Vol. AP-34, pp. 1080-1091, Sep. 1986.

[13] H. Nakano, S.R. Kerner and N.G. Alexopoulos, " The moment method solution of printed wire antennas of arbitary configuration," IEEE Trans. on Antennas Propagat., Vol. AP-36, pp. 1667-1674, Dec. 1988.

[14] J.R. Mosig and F.E. Gardiol, "Analytic and numerical techniques in the Green's function treatment of microstrip antennas and scatters," IEE Proc., Vol. 130, pt. H, No. 2, pp. 175-182, March 1983.

[15] P.B. Katehi and N.G. Alexopoulos, "Real axis integration of Sommerfeld integrals with application to printed circuit antennas," Journal of Math. Phys., 24, March 1983.

[16] C.L. Chi and N.G. Alexopoulos, "An image extraction approach to modeling printed circuit antennas, Electromagnetics 6, pp. 161-170, 1986.

[17] N.K. Uzunoglu, N.G. Alexopoulos, and J.G. Fikioris, "Radiation properties of microstrip dipoles," IEEE Trans. on Antennas Propagat., Vol. AP-27, pp. 853-858, Nov. 1979.

[18] M.C. Bailey and M.D. Deshpande, "Integral equation formulation of microstrip antennas," IEEE Trans. on Antennas Propagat., Vol. AP-30, pp. 651-656, July. 1982.

[19] D.M. Pozar, "Input impedance and mutual coupling of rectangular microstrip antennas," IEEE Trans. on Antennas Propagat., Vol. AP-30, pp. 1191-1196, Nov. 1982.

[20] D.R. Jackson and N.G. Alexopoulos, "Analysis of planar strip geometries in a substrate-superstrate configuration," IEEE Trans. on Antennas Propagat., Vol. AP-34, pp. 1430-1438, Dec. 1986.

[21] R.W. Jackson and D. M. Pozar, "Full wave analysis of microstrip open-end and gap discontinuities," IEEE Trans. on Microwave Theory and Technique, Vol. MTT-33, pp.1036-1042, Oct. 1985.

[22] E.H. Newman and D. Forral, "Scattering from a microstrip patch," IEEE Trans. on Antennas Propagat., Vol. AP-35, pp. 245-251, March 1987.

[23] H.Y. Yang and N.G. Alexopoulos, "A dynamic model for microstrip-slotline transition and related structures," IEEE Trans. on Microwave Theory and Technique, Vol. MTT-36, pp.286-293, Feb. 1988.

[24] D.M. Pozar, "Improved computational efficiency for the method of moments solution of printed dipoles and patches," Electromagnetics 3, pp. 299-309, July-Dec 1983.

[25] H.Y. Yang and N.G. Alexopoulos, "Basic building block for high frequency interconnects: theory and experiment,: IEEE Trans. on Microwave Theory and Technique, Vol. MTT-36, pp.1258-1264, Aug. 1988.

[26] L.N.G. Filon, "On a quadrature fomula for trigonometric integrals," Proc. R. Soc. Edinburgh, 1982, 49, pp. 38-47.

[27] H.Y. Yang and J.A. Castaneda, "Printed dipole characteristics in a two-layer geometry with uniaxial anisotropy," Electromagnetics, no. 4, pp.439-450, 1989.

[28] I. Hsia, H.Y. Yang and N.G. Alexopoulos, "Microstrip antennas on ferrite substrate," To be presented in IEEE Antenna Propagat. Soc. Int. Symp., Dallas, May 1990.

[29] I. Hsia, H.Y. Yang and N.G. Alexopoulos, "Basic properties of microstrip circuit elements on nonreciprocal substrate-superstrate structures," To be presented in IEEE MTT-S 1990 Int. Microwave Symp., Dallas, May 1990.

[30] D.M. Pozar and D.H. Schaubert, "Scan blindness in infinite phased arrays of printed dipoles," IEEE Trans. on Antennas Propagat., Vol. AP-32, pp. 602-610, June 1984.

[31] D.M. Pozar and D.H. Schaubert, "Analysis of in infinite array of rectangular patches with idealized probe feeds," IEEE Trans. on Antennas Propagat., Vol. AP-32, pp. 1101-1107, Oct. 1984.

[32] J.A. Castaneda and N.G. Alexopoulos, "Infinite arrays of microstrip dipoles with a superstrate(cover) layer," in IEEE Antenna Propagat. Soc. Int. Symp. Dig., Vamcouver, Canada, June 17-21, 1985, pp. 713-717.

[33] M.D. Deshpande and P.D.R. Prabhakar, "Analysis of dielectric covered infinite array of rectangular microstrip antennas," IEEE Trans. on Antennas Propagat., Vol. AP-35, pp. 732-736, June 1987.

[34] J. A. Castaneda, *Infinite Phased Array of Microstrip Dipoles in Two layers,* Ph.D. Dissertation UCLA, Dec. 1988.

[35] J.L. Tsalamengas and N.K. Uzunoglu, "Radiation from a dipole in the proximity of a general anisotropic grounded layer," IEEE Trans. on Antennas Propagat., Vol. AP-33, pp. 165-172, Feb. 1985.

[36] M. Olyphant, jr., "Measuring anisotropy in microwave substrate," in IEEE MTT-S 1979 Int. Microwave Symp. Dig., Apr. 30-May 2, 1979, pp.91-94.

☆U.S. GOVERNMENT PRINTING OFFICE

MISSION

OF

ROME LABORATORY

Rome Laboratory plans and executes an interdisciplinary program in research, development, test, and technology transition in support of Air Force Command, Control, Communications and Intelligence (C^3I) activities for all Air Force platforms. It also executes selected acquisition programs in several areas of expertise. Technical and engineering support within areas of competence is provided to ESD Program Offices (POs) and other ESD elements to perform effective acquisition of C^3I systems. In addition, Rome Laboratory's technology supports other AFSC Product Divisions, the Air Force user community, and other DOD and non-DOD agencies. Rome Laboratory maintains technical competence and research programs in areas including, but not limited to, communications, command and control, battle management, intelligence information processing, computational sciences and software producibility, wide area surveillance/sensors, signal processing, solid state sciences, photonics, electromagnetic technology, superconductivity, and electronic reliability/maintainability and testability.